

Bose-Einstein Condensate Based Atom-Optics δ -Kicked Rotor For Precision Measurements

A thesis

Submitted in partial fulfillment of the requirements of the degree of

Doctor of Philosophy

by:

Jay Mangaonkar

Registration ID 20132019



Department of Physics


INDIAN INSTITUTE OF SCIENCE EDUCATION AND RESEARCH

PUNE - 411008, India

Certificate

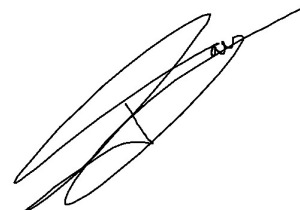
Certified that the work incorporated in the thesis entitled “**Bose-Einstein Condensate Based Atom-Optics δ -Kicked Rotor For Precision Measurements**” submitted by **Jay Mangaonkar** was carried out by the candidate, under my supervision. The work presented here or any part of it has not been included in any other thesis submitted previously for the award of any degree or diploma from any other university or institution.

Date: June 11, 2021


(Supervisor)

Declaration

I hereby certify that the work which is being presented in the thesis entitled “**Bose-Einstein Condensate Based Atom-Optics δ -kicked Rotor For Precision Measurements**” in partial fulfillment of the requirements for the award of the Degree of **Doctor of Philosophy** and submitted in the Department of Physics of the Indian Institute of Science Education and Research, Pune is an authentic record of my own work carried out during a period from August, 2013 to June, 2020 under the supervision of Dr. Umakant D. Rapol, Associate Professor, Department of Physics, Indian Institute of Science Education and Research, Pune. The matter presented in the thesis has not been submitted by me for the award of any other degree of this or any other institute.



Date: June 11, 2021

(Jay Mangaonkar)

Abstract

This thesis presents the realization of a Bose-Einstein Condensate (BEC) based Atom-Optics δ -Kicked Rotor experiment (AOKR) using ^{87}Rb atoms and its utility in atom interferometry and precision measurements. The AOKR involves subjecting the BEC to a series of optical lattice pulses. The phase modulation of the BEC wavefunction due to the optical lattice potential splits it into discrete momentum states. When the pulse period is equal to an integer or half integer multiple of the ‘Talbot time’, the total energy imparted to the system per pulse either quadratically increases (resonance) or is completely suppressed (anti-resonance). Monitoring these resonances allows measurement of Talbot time which is connected to the atomic recoil frequency. The recoil-frequency along with other physical quantities constitutes the fine structure constant α . Since the value of α governs the strength of interactions between elementary particles, its precision measurement via different techniques is important. In the AOKR pulse scheme that we follow, the optical lattice pulse phase modulation is negated by inverting its sign for the rest of the pulses. The measurement of the revival of the initial state or the fidelity then constitutes as the Talbot time measurement. The sign inversion of the phase modulation is brought about by shifting the phase of the optical lattice by π -radians. The pulse scheme can also be thought of as a multi-path atom interferometer. The BEC which is used as an input for this interferometer is obtained after laser cooling in a Magneto-Optical Trap (MOT) and subsequent evaporative cooling in an hybrid optical crossed dipole trap. Since the quasi-momentum dynamics are theoretically predicted to play an important role in the dynamics of the AOKR pulse scheme, the characterization of the BEC initial state and its evolution is done. The finite momentum spread of the BEC is theoretically proposed to affect the sensitivity of the AOKR pulse sequence. We measure this predicted deviation from ideal dispersion-less AOKR behavior and it agrees with the simulations. Ultimately, we measure the Talbot time with a relative uncertainty of 1.2×10^{-3} . While execution of the phase-inversion pulse sequences, it is observed that the momentum distribution within a diffracted order and the population of the orders about zero momentum state shows an asymmetry when the phase differed from π radians. This intra-order and inter-order asymmetry is characterized for the case of two pulses. The intra-order asymmetry has been previously unreported and is unique

as it possess a net asymmetry without a net momentum current. The enhancement in sensitivity of inter-order asymmetry to resonance suggests that it can be used as a probe in future AOKR experiments.

Dedicated to
Life, the Universe and Everything

Publications from the thesis work

- Effects of finite momentum width on the reversal dynamics in a BEC based atom optics δ -kicked rotor; **Jay Mangaonkar**, Chetan Vishwakarma, S Sagar Maurya, Sumit Sarkar, Jamie L. MacLennan, Pranab Dutta and Umakant D. Rapol, *Journal of Physics B: Atomic, Molecular and Optical Physics*, **53**, 235502 (2020)

Publications from contribution to other work

- Nonmonotonic diffusion rates in atom-optics Lèvy kicked rotor; Sanku Paul, Sumit Sarkar, Chetan Vishwakarma, **Jay Mangaonkar**, M. S. Santhanam and Umakant D. Rapol, *Physical Review E*, **100**, 060201(R) (2019)
- Diffraction of a CW atom laser in Raman-Nath Regime; Sumit Sarkar, **Jay Mangaonkar**, Chetan Vishwakarma and Umakant D. Rapol, *Physical Review A*, **98**, 043625 (2018)
- A simple atomic beam oven with a metal thermal break; Chetan Vishwakarma, **Jay Mangaonkar**, Kushal Patel, Gunjan Verma, Sumit Sarkar and Umakant D. Rapol, *Review of Scientific Instruments*, **90**, 053106 (2019)

Acknowledgments

I open at the close. Just like these words on Harry's golden snitch, opening the acknowledgment section in some sense feels like steps being taken to close my Ph.D. journey at IISER-Pune and what a journey it has been! The timing of 'the close' feels right. Though we are still far from done with the pandemic, efforts to fight it are beginning to bear fruit. Monsoon (arguably the best season that Pune has) is around the corner and the campus is starting to take a shade of green. In the lab too, vacuum pumps are whirring round the clock to bring the strontium and rubidium setups back online for new and exciting set of experiments. This lab, helmed by Prof. Umakant Rapol, has been at the core of my Ph.D. journey. I will be forever in his debt for letting me join his lab and providing valuable guidance for navigating the field of experimental atomic physics. Perseverance, tenacity, no-nonsense approach to experiments and a keen eye for detail are a few of the many qualities in him that I admire. In my view, it's somewhat of an impossible task to build complex experiments in India like the one in lab-213 from scratch without having someone like him around.

I have had the chance to witness multiple generations of students who worked in this lab. When I joined as a clueless undergrad back in 2013, the rubidium experiment was just being re-built after being shifted out from the satellite campus. I saw my seniors work tirelessly almost round the clock, to get the elusive Bose-Einstein condensate. What impressed me (and still does) was the diverse range of problems being tackled from plumbing and electronics to atom trapping and laser cooling. The people I worked with early on were Sunil, Sumit, Chetan, Gunjan, Sainath and Jithin. I tried to assimilate some qualities I admired about each of them. Sunil 'bro' is one of the coolest guys I've ever met. His attitude of remaining calm and laughing it off even in critical situations became something of a 'core tenet' for me. Sumit Sarkar taught me the ropes of the rubidium experiment. His disciplined approach to doing experiments was vital in getting the crossed-dipole trap working. Discussions with him had a major part in getting my article published. Following the example set by Gunjan, I decided to do the simulations for the experiments I was doing by myself and it was a very rewarding experience. Working with Chetan was a very enjoyable experience. The strontium Magneto-Optical Trap (MOT) was achieved despite of severe budgetary constraints due

to his skill, resourcefulness and consistent efforts. His cheerful and helpful nature set up a good mood in the workspace. Personally, his friendship played a great part in keeping a sane head throughout. Sainath was someone who had almost the same weird taste in humor as mine. I've seldom seen anyone pursue perfection as much as him. He took on several projects in the lab which benefited both the setups and was the go-to person for any matter involving programming. Jithin brought unbounded energy with him which pushed up everyone's efforts. I also had the opportunity to work with the lab's younger generation i.e. Shivsagar, Kushal, Korak and Pranab. All of them are brilliant individuals who luckily share the same rapport that I got to experience with my seniors. I can safely say that the lab has been passed on to very skilled hands. A special shout-out goes to the lab visitors in 2019, Jamie and Harinee. Jamie brought a fresh perspective to the lab and I got to learn a lot from her. She inspired me to go for runs, which has become a habit now. I will always cherish our evening runs and long dinner discussions over a plethora of topics. I always wondered how Harinee was able to function with a constant smile on her face and a spring in her step. There was never a dull moment with her enthusiasm around. I would also like to thank h-cross support staff: Nilesh Dumbre, Prashant Kale, Sudhir Lone and people from the administrative department: Prabhakar, Dhanashree, Tushar and Sayalee. For almost a year, I had the opportunity to work at Prof. Vasant Natarajan's lab at the Indian Institute of Science-Bangalore, for which I am very grateful. I thank all the lab members there: Raghuv eer, Nikhil, Mangesh, Sumanta, Santosh, Pushpendar, Abhilash, Subbu, Vineet, Harish and Nadeem for hosting me and for all the fun.

Outside of the lab, the I-Ph.D. 2013 batch functioned like a family for me. Tackling the early undergrad days was much easier almost entirely due to the love and support from these awesome set of individuals. I would especially like to acknowledge a few of them: Neel was the person responsible for almost all of the trips and dinner outings we had and was a source of much needed drama. Sandip and I shared a lot of common tastes and it was fun to discuss the 'deeper mysteries' of life with him. Anish was one of the few who used to laugh at my lame jokes. The debates and discussions randomly held in his room was a good way to unwind. Bharat provided the complimentary crazy vibe to Neel and was the life of any party or trip that we did. Ron (whenever he was

present on the campus) was that reliable friend required for successful execution of plans. Deepak shared my love of fantasy novels and introduced South Park to me. Most of the weekend movies I caught were with him as company. Adarsh, as his name goes, was an academic ideal to strive for. He was also the first ever roommate I had. Kashyap was the most athletic one among us and the late night tea sessions with him were always refreshing. Shivani was always very enthusiastic and cheery about plans to hang out. One could always rely on Dhriti for locating and cooking delicious food and teaching us cool dance moves. Mehak always looked out for everyone and was there anytime I needed help. Amar and Akhila were the power couple and also were generous hosts for partying. I fondly remember the trips to central Pune in the early days with Charu. The rest: Anshul, Harpreet, Aditi, Swati, Divya also made the experience all the more fun and unforgettable. I thank all of them for constituting the best cohort that one could ever ask for. I would also like to thank one of my oldest friends, Vinay, for all the strange things that we share and for being a good friend.

I thank my cousins and their families for their love. They were always curious about what I was doing and encouraged me to see it through to the end. I would also like to thank my family to support my decision to do a Ph.D. They went to great lengths to ensure that I don't get distracted from my studies and provided whatever I needed. All of this would have been impossible without their love and support.

Date: June 10, 2021

(Jay Mangaonkar)

Contents

Declaration	v
Abstract	vii
Publications from the thesis work	xi
Acknowledgments	xiii
List of figures	xxi
1 Introduction	1
1.1 The wave-particle duality	1
1.2 Matter-wave Interferometry	2
1.3 Atom Interferometry (AI)	3
1.4 Multi-path atom interferometers	7
1.4.1 The Talbot effect	8
1.4.2 The Talbot-Lau effect	10
1.5 Objective of the thesis	11
1.6 Organization of the thesis	12
2 Introduction to laser cooling and Bose-Einstein Condensate	15
2.1 Phase space density (PSD)	15
2.2 The two-level system	16

2.2.1	The scattering force	17
2.3	The magneto-optical trap (MOT)	19
2.4	The optical dipole trap	22
2.5	Evaporative cooling	24
2.6	Condensation of a non-interacting Bose gas	26
2.6.1	Effect of interactions on the ground state of a trapped BEC . . .	31
2.6.2	Calculation of BEC momentum width	35
3	Matter-wave diffraction	37
3.1	Coherent transfer of momentum from an optical potential	37
3.2	Two photon transitions	39
3.3	The Raman-Nath regime	40
3.4	The Bragg regime	44
3.5	Preparation and control of diffraction beams	45
4	The δ-kicked rotor	49
4.1	Classical δ -kicked rotor and chaos	49
4.2	Atom-optics quantum δ -kicked rotor (AOKR)	51
4.3	Dynamical localization	52
4.4	Quantum resonances	53
5	Measurement of Talbot time using AOKR	57
5.1	Measurement scheme	57
5.1.1	Pulse scheme-1	58
5.1.2	Pulse scheme-2	61
5.2	Experimental results	64
5.3	AOKR as a velocity filter	67
5.4	Conclusion	68
6	Asymmetry in AOKR	71
6.1	Intra-order asymmetry	71
6.2	Inter-order asymmetry	75

7	Quantum ratchet	77
8	Numerical methods	81
9	Conclusion and future experiments	87
9.1	Summary	87
9.1.1	Realization and characterization of BEC	87
9.1.2	Preliminary experiments with diffraction using an optical lattice	87
9.1.3	AOKR pulse scheme for measurement of Talbot time	88
9.1.4	Asymmetry in momentum distribution	89
9.2	Future experiments	90
9.2.1	Continuous-time quantum walk (CTQW) with AOKR	90
9.2.2	Effect of interactions on the Talbot effect	90
9.2.3	Realization of asymmetric beam splitter and combiner with AOKR	91
A	Appendix	93
A.1	Characterization of lattice phase noise induced due to vibrations	93
A.2	BEC momentum width measurement using Bragg spectroscopy	95
A.3	Absorption imaging	96

List of Figures

- 1.1 **Atom interferometer in a Mach-Zehnder (MZI) configuration:** The atomic cloud (blue sphere) is split and recombined by three pulses of a running wave optical lattice formed from the laser beams with wave-vectors k_1 , k_2 and frequencies ω_1 , ω_2 , thus forming an atom interferometer. The states $|0\rangle$ and $|1\rangle$ are the momentum states coupled by the Bragg interaction with the lattice. The interferometer sensitivity is directly proportional to the blue shaded area, which is the total area enclosed by the interferometer. 3
- 1.2 **Multi-path interferometer schematic:** The blue spheres represent cold atom cloud as the initial state with zero momentum in the frame of the optical lattice. The optical lattice pulses couple multiple momentum states (denoted by black arrows), in contrast with a standard two-path interferometer. Here $|n \hbar K\rangle$ denote the momentum state populated by the atomic ensemble on interaction with the lattice ($K = k_1 + k_2$). . . . 5
- 1.3 **Measurement of the fine structure constant (α):** The uncertainty in the Rydberg constant and rubidium mass is taken from Ref. [1]. The uncertainty in the electron mass value is taken from Ref. [2]. ω denotes the angular frequency corresponding to the optical lattice wave-vector. 8

1.4	<p>The optical Talbot effect: Simulated intensity profile $E ^2$ of a plane wave with wavelength λ incident from the left on a grating with period a. The color bar on the right is an indicator of the same (intensity = $E ^2$, E being the electric field amplitude). The intensity pattern is repeated with a shift of $a/2$ in the y-direction after integer multiples of L_T. The fractional Talbot effect at $x = L_T/2$ is also visible.</p>	9
2.1	<p>MOT schematic for $J = 0 \rightarrow J = 1$ transition. The Zeeman splitting (exaggerated in the figure) caused by the magnetic field gradient causes preferential absorption of light from either the σ^+ or the σ^- beams depending on the atoms position along the z-axis. This position dependent imbalance between the imparted force from the two beams drives the atoms towards $z = 0$ resulting in a net confinement.</p>	19
2.2	<p>^{87}Rb D2 line: (Left) The energy level diagram of the D2 transition with hyper-fine splitting. The cooling laser is red detuned by about 2Γ from $F = 2\rangle \rightarrow F' = 3\rangle$, where $\Gamma = 2\pi \times 6$ MHz while the repumper is almost resonant to the $F = 1\rangle \rightarrow F' = 2\rangle$ transition. (Right) the saturation absorption spectroscopy signal which is used to lock the lasers on the relevant transitions. The numerals on top of the spectra denote the F' state. The lines which possess two numbers represent the cross-over resonances.</p>	20
2.3	<p>The AC Stark effect. (Left) The spatially varying energy splitting between the ground and the excited state of the ‘atom+light field’ system for a negative detuning δ. The blue sphere represents the atoms which are attracted towards the point where the down shift in energy is the highest i.e the point of highest intensity of the beam. (Right) Schematic of the far-detuned crossed dipole trap configuration used in our setup. A pair of 1064 nm laser beams are focused at the position of the atoms with a beam waist ($2w_0$) of about $70 \mu\text{m}$. The initial power in the beams is about 6 W, providing confinement potential in the range of $\sim 100\text{s} \mu\text{K}$.</p>	22

2.4	Trapping frequency measurement: Atoms were given an impulse of magnetic field force and allowed to oscillate for a variable time t in the optical dipole trap before being released. The y-axes of the plots denote the displacement after a period of time-of-flight which captures the velocity of the atoms when the trap is turned off. Vertical ($2\pi \times 122 \pm 5$ Hz) and horizontal ($2\pi \times 134 \pm 7$ Hz) denote orientation w.r.t gravity.	23
2.5	Evaporative cooling: The trapping potential is slowly lowered from left to right resulting in the ejection of atoms having energy higher than the confinement threshold. The rest of the atoms re-thermalize at a lower temperature via elastic collisions.	25
2.6	Bose-Einstein condensation of ^{87}Rb in an optical dipole trap: The figure shows time-of-flight images during the final evaporation steps in the ODT. The momentum distribution starts developing a deviation from the thermal distribution as the transition is approached. The center image clearly shows this bimodal (Gaussian+Thomas-Fermi) distribution, where the central component represents from the atoms in the condensed state. The final image shows an almost pure BEC state. The mentioned temperature is of the thermal component.	29
2.7	Temporal evolution of the expansion scale factor b_i: The plot shows the analytical solutions for $b(\tau)$ in different regimes along with the solution obtained from solving the second order differential equation directly in MATLAB ($\tau = \omega_0 t$). The solution is linear in the long term showing that the expansion velocity attains a saturation after sometime.	32
2.8	Expansion of BEC after release from the trap: (Top) Absorption images of the BEC for different time-of-flights. The BEC under goes expansion as the interaction energy of the BEC is released as kinetic energy. (Bottom) The calculated expansion coefficient along with the experimentally observed one assuming a spherical trap with a trapping frequency of $\omega_0 = 2\pi \times 129$ Hz. τ is expressed in dimensionless units as $\tau = \omega_0 t$	34

3.1	<p>Momentum transfer using optical fields: (Left) No net momentum is imparted to the atom (blue sphere) via a coherent process in the case of a running wave. (Right) In this case a net momentum is imparted to the atom as it can absorb a photon from one field and emit it into the other through a stimulated emission process.</p>	38
3.2	<p>Raman-Nath regime of diffraction: (Left) (a) The BEC, prepared and confined in a crossed optical dipole trap is released after a certain wait time. (b) A standing wave is pulsed on for a variable time. This standing wave periodically modulates the condensate wavefunction, thus causing the BEC to diffract into different momentum states. (c) The BEC is then allowed to undergo free fall till the diffracted wavepackets can be resolved via absorption imaging. (Right) Experimentally observed absorption image of the diffraction process. The pulse period was kept as $t = 0.225 \omega_r^{-1} (9.5 \mu s)$. The population in the diffracted orders agree with the Bessel distribution formula (Eq. 3.10) applicable in the Raman-Nath regime for a Bessel function argument of 1.7 as explained in the text below.</p>	41
3.3	<p>Beyond the Raman-Nath regime: (a) Simulated momentum distribution of momentum states for variable evolution time under optical lattice potential with $V_0 = 80 \hbar \omega_r$. The time axis is scaled w.r.t to the total pulse duration of $6 \mu s$. It can be seen that after $\sim 3 \mu s$, the population in diffracted orders beyond $m \sim \pm 10$ does not increase because of the breakdown of the Raman-Nath regime. (b) Experimentally observed momentum distribution of BEC subjected to a lattice potential for variable time. It can be seen that after sometime the initial zero momentum state is again populated. This ‘rephasing’ time roughly corresponds to a quarter of the oscillation period of the lattice harmonic potential. . . .</p>	42

3.4	<p>Bragg diffraction: (Left) Energy conservation condition for a two-photon transition connecting $0\rangle \rightarrow 1\hbar K\rangle$ momentum states. The difference in frequencies of the two beams that make the running lattice should be $\omega_1 - \omega_2 = 4E_r/\hbar \approx 2\pi \times 15.2$ kHz for ^{87}Rb with 780 nm light. (Right) experimentally observed first order Bragg diffraction of the BEC.</p>	43
3.5	<p>Lattice preparation: (Top) The optical lattice is formed from two counter propagating beams, each derived from a diffracted AOM order and delivered to the atoms via optical fibers. The AOMs are driven by two phase locked RF sources AFG-1 and AFG-2 (Tektronix, AFG 3101). Their relative phase can be set to any value. (Bottom) The signal from these AFGs is fed to the AOMs via RF amplifiers (Mini-Circuits, ZHL-1-2W). AOM-1 can be driven by either of the two function generators depending on the state of the source toggle TTL (Mini-Circuits, ZYSWA-2-50DR). Thus the phase of the optical lattice beam can be toggled between any two fixed values within ~ 10s of ns. The amplitude of the optical lattice is pulsed via switches 2 and 3. The pulse train for these is passed through a delay generator (SRS, DG-535) to adjust for a time lag between the pulses caused due to different electronic paths.</p>	47
4.1	<p>Classical chaos in δ-kicked rotor: (Left) Representative model of the δ-kicked rotor. A particle (blue sphere) which is free to rotate on a ring of radius R, is periodically ‘kicked’ with a force F. (Right) Poincaré sections of the δ-kicked rotor, governed by the standard map (Eq. 4.3). As the stochasticity parameter κ is increased beyond ~ 1 the system dynamics become chaotic.</p>	50
4.2	<p>Localization in quantum δ-kicked rotor: (Left) The average energy of the system as a function of the number of kicks. The energy growth is arrested beyond a certain ‘quantum break time’. The simulation parameters are $\kappa = 11.6$ and $\hbar_{eff} = 1$. (Right) The momentum distribution in this ‘localized’ regime assumes a double-exponential profile.</p>	52

- 4.3 **Quantum resonance: (Left)** Time-of-flight images after subjecting the BEC to δ -pulses of standing wave at resonant period ($T = 66.34 \mu\text{s}$ for ^{87}Rb) with kick strength $\phi_d = 0.8$. The momentum orders get progressively populated as number of kicks increase. **(Right)** Energy growth corresponding to the images shown on the left along with a power law fit ($E = AN^B$). The fit parameters are $A = 0.59 \pm 0.11$, $B = 1.81 \pm 0.15$, implying that the energy grows quadratically with each kick. The red circles correspond to the experimental data. The black squares correspond to the numerical simulations. 54
- 4.4 **Quantum anti-resonance: (Left)** Time-of-flight images after subjecting the BEC to δ -pulses of standing wave ($\phi_d = 0.8$) at anti-resonant period ($T = 33.15 \mu\text{s}$ for ^{87}Rb). Each kick cancels out the phase modulation produced by the previous one. **(Right)** Energy evolution corresponding to the images shown on the left. The contrast in anti-resonant behavior is not perfect due to a finite momentum width of the BEC. . . . 55
- 5.1 **Pulse scheme-1: (Left)** Schematic of the pulse scheme. After the first N pulses, the phase of the optical lattice is shifted by π radians and the lattice power is ramped up such that the phase modulation depth is $N\phi_d$. At resonance this last pulse cancels out the phase modulation of the previous pulses and revives the initial state. **(Right)** Experimental implementation of the pulse sequence for $N = 4$, $\phi_d = 0.8$. As it can be seen the fidelity at resonance is less than unity due to the momentum width of the BEC. Simulated values accommodate this momentum spread in initial ensemble ($\Delta p = 0.035$). 58
- 5.2 **Pulse scheme-2:** The evolution of the BEC wavefunction is shown in momentum space at the resonance condition ($T = T_T$). The spheres represent of the relative population present in different momentum states after each pulse in the sequence shown at the bottom. The number in n^{th} order is $\propto |\langle 2n\hbar k | \psi(p) \rangle|^2$. \vec{k}_1 and \vec{k}_2 denote the wave vectors of the two laser beams forming the standing wave that is pulsed for a duration of τ_p , according to the shown sequence. 59

5.3 **Variation of fidelity $I(l)$:** Fidelity (I) as a function of scaled pulse period (l) for different number of kicks N at a constant kick strength $\phi_d = 0.8$. The red dots are the experimental data and the blue solid lines are the numerical simulations. The error bars represent \pm one standard deviation over 5 data points. $\Delta\beta$ is the only free parameter used to match the experimental values at different number of kicks. The values for $\Delta\beta$ used are 0.023 for $N=2$ and 0.017 for $N = 3, 4, 5$ respectively. Data for $N = 1$ is not shown here as fidelity doesn't undergo significant change at this scale. 61

5.4 **Scaling of sensitivity ($S = \Delta l/2$) with number of pulses ($N = 1 - 5$):** using fidelities obtained from the experimental measurements (red circles), from the analytical equations with $\Delta\beta = 0$ (Eq. 5.6, black squares) and with $\Delta\beta = 0.0229$ (Eq. 5.11, blue triangles), each with linear fits for $\phi_d = 0.8$. The slopes of the linear fits are -1.85 ± 0.12 (red solid line), -2.23 (black dashed line) and -1.95 (blue dash-dot line). Eq. 5.6 and 5.11 were truncated to $n = \pm 20$ (convergence observed for $|n| \geq 7$). 65

5.5 **Suppression of resonant fidelity with number of pulses: (Left)** The evolution of population in different momentum states as a function of kick number at resonant pulse period $l = 2$, where the phase of the lattice is inverted from kick 5 onward. The simulation data depicts the amount of population in each momentum state for parameters $\phi_d = 0.8$, $N = 4$ and $\Delta\beta = 0.023$. The experiment data contains the absorption images taken for $\phi_d \sim 0.8$ after 7 ms time of flight. **(Right)** Peak fidelity at resonance $I(l = 2)$ as a function of number of kicks N . The red dots are experimental data of fidelity at resonance and the blue squares are theoretical values obtained from Eq. for parameters $\phi_d = 0.8$ and $\Delta\beta = 0.023$. Error bars on experimental values indicate \pm one standard deviation over 5 data points. 66

5.6 **AOKR as a velocity filter:** (Left) absorption images of the BEC subjected to two kicks ($\phi_d \sim 2.1$) with a relative lattice phase of π -radians between them. The pulse period was equal to the Talbot time. The kicks were delivered 5 ms after the trap release and images were captured after an additional 15 ms time-of-flight. In comparison to the un-kicked BEC (a), the narrowing of the zeroth momentum order profile in the direction of the lattice is clearly visible in (c). (Right) the absorption image data in (c) is integrated to give a line plot. The simulation data is also displayed for the parameters $\phi_d = 2.1, \Delta\beta = 0.031$. The dashed circle highlights the gap left in the second diffracted order due to momentum selectivity of the AOKR resonance. 67

6.1 **Intra-order and inter-order asymmetry:** Simulated momentum distribution after an initial Gaussian wave-packet centered at $j = 0$ with momentum spread $\Delta\beta = 0.05$ is subjected to two pulses of kick strength $\phi_d = 0.8$. The red dashed line indicates $k, \beta = 0$. (a) Here, the pulse period is $l = 2$ and the relative lattice phase between the two pulses is $\Phi = \pi$. The distribution is symmetric about $\beta = 0$ for each j and no net momentum current is present. (b) At $l = 2$ and $\Phi = \pi + 2$, the asymmetry in the β distribution of $j = 0$ is clearly visible. As explained in the text, no net current is induced despite of the asymmetry. (c) For $\Phi = \pi + 0.5$ and $l = 1.5$, a net momentum current is induced, as seen in the population difference between the 1 and -1 orders. The y-axis scale is not the same for the three cases. 72

6.2 **Top left:** Intra-order asymmetry for $N = 1$ as a function of the lattice phase. The asymmetry (A_{00} in Eq. 6.2) is calculated as $(n_+ - n_-)/(n_+ + n_-)$, where n_+ and n_- denote the integrated probability density in the positive and the negative sections of the 0^{th} order momentum bin ($-0.5 \leq \beta < 0.5$). Red dots denote the average experimental asymmetry value over 3 data points. Blue solid line denotes the theoretically calculated value for $\phi_d = 1.15$ and $\Delta\beta = 0.023$ using Eq. 6.2. **Top right:** experimental absorption images taken after 20 ms time-of-flight for the following lattice phase settings $\Phi =$ (a) $\pi/3$, (b) π and (c) $5\pi/3$ radians. White dashed lines indicate the $\beta = 0$ position at each discrete momentum bin. **Bottom left:** Inter-order population asymmetry for $N = 1$ as a function of pulse period, at a fixed lattice phase. The asymmetry here is calculated in the same manner as above, where n_+ and n_- denote the integrated probability density in first order diffracted populations ($\pm 1 \hbar K$). Red dots denote the average experimental asymmetry value over 5 data points. Blue solid line denotes the simulated curve for $\phi_d = 0.8$, $\Delta\beta = 0.023$ and $\Phi = \pi + 0.35$. **Bottom right:** experimental absorption images taken after 7 ms time-of-flight for the following pulse periods $l =$ (d) 1.4, (e) 2 and (f) 2.5. Error bars in both the figures denote \pm one standard deviation. 74

6.3 **Comparison of asymmetry and fidelity for the measurement of Talbot time:** The blue dash-dot line denotes the simulated fidelity for a two kick sequence based on the phase reversal scheme explained in section 5. The red solid curve denotes the simulated absolute value of the asymmetry for a two kick sequence as defined in Fig. 6.2. It can be clearly seen that the asymmetry signature is much narrower than the fidelity near resonance, for the same kick strength ($\phi_d = 0.8$) and initial state momentum width ($\Delta\beta = 0.023$). The phase offset between the two kicks for the asymmetry plot is 0.35 rad. 75

7.1	Gradient force on atoms: The distribution of the wavefunction $\psi(x) = 0 \hbar K\rangle + e^{i\pi/2} 1 \hbar K\rangle = 1 + ie^{iKx}$ is shown in position space alongside the optical lattice potential $V(x) = \cos(Kx)$. The maximum gradient of the potential coincides with the peak of the distribution. The force due to this gradient drives the ratchet.	78
7.2	Realization of a quantum ratchet: Top: Pulse schematic for creation of the quantum ratchet. The Bragg pulse prepares the initial state which is then subjected to the δ -kicked rotor pulses. The phase offset of the optical lattice between the Bragg and the kicked rotor pulses was γ . The kicked rotor pulses were applied with a resonant period of $T = 33.17 \mu\text{s}$ and a frequency detuning of $\sim 15 \text{ kHz}$ between the kicking beams. The kick strength was kept as $\phi_d \sim 1$. Bottom: Time-of-flight images of the BEC after application the Bragg and δ -kicked rotor pulses. The color-bar indicates optical density.	79
8.1	Simulated momentum distribution in the Raman-Nath regime. The simulation parameters are: potential depth $V_0 = 160 \hbar\omega_r$ and interaction time $t = 0.01 \omega_r^{-1}$. Since the parameters satisfy the Raman-Nath regime, the population distribution follows a Bessel distribution $J_n^2(V_0 t/\hbar)$, where n is the diffraction order.	83
9.1	Diffraction profile for different pulse application times: In the first row the optical lattice pulse was applied immediately after releasing the BEC from the trap ($t = 0 \text{ ms}$). It can be seen that the diffraction orders are significantly narrower in comparison to the case where the pulse is applied much later ($t = 6 \text{ ms}$). No pulse is applied in the last row. All images are taken after 20 ms from the trap release.	91

9.2	AOKR based interferometer: The blue spheres denote the atomic ensemble. The first pulse pair splits this ensemble into a equal superposition of $ 0\rangle$ and $ 1\rangle$ states, where $ n\rangle$ denotes the n^{th} diffraction order. l and Φ denote the pulse pair separation and the relative lattice phase between the pair respectively. The Bragg π -pulse transfers atoms into the $ -1\rangle$ state. The interferometer is then closed by the final pulse pair.	92
A.1	Interferometric diagnosis of vibration noise: Schematic of the test setup used to characterize the vibration noise introduced in the optical lattice. Light from the laser was split into two paths using a non-polarizing beam splitter. The longer path traversed the optical fiber length and a distance $2L = 18$ cm, which is the separation between the two steel posts. This path was then interfered with the shorter one on the photo-diode. Any vibrations in the steel posts Δx (highly exaggerated in the figure) produced a intensity variation in the interferometer signal. The photo-diode signal was fed to a spectrum analyzer (SRS's SR785).	93
A.2	FFT of photo-diode data: The marked peaks in frequency are as follows: $f_1 = 64.5$ Hz, $f_2 = 72$ Hz and $f_3 = 89.5$ Hz. Thus, the timescale for the vibrations is at the level of ~ 10 ms for this configuration of optics. Inset shows the time series data captured on an oscilloscope over a time scale of 80 ms.	94
A.3	Bragg spectroscopy of BEC: The BEC was subjected to a Bragg pulse of $200 \mu s$ duration, $100 \mu s$ after release from the trap. The frequency difference between the Bragg beams was scanned from 0-30 kHz. The standard deviation of the Gaussian fit to diffraction efficiency peak is 2.26 kHz.	95

Chapter 1

Introduction

1.1 The wave-particle duality

The birth of quantum mechanics can be dated to the formulation of the quantum theory of radiation by Max Planck in 1900 [3]. He postulated that energy can be absorbed and emitted only in quantized units i.e $E = h\nu$ (E =energy, ν = frequency and h = Planck's constant). This equivalence of an object's energy to frequency, was generalized by L. de Broglie by ascribing a 'phase wave' to all particles in his short article in 1923 [4]. In his view, the equations of motion for particles had to evolve beyond the geometric approach towards an 'undulation' or wave theory, similar to the case of 'electromagnetism'. The wavelength λ_{dB} of this 'phase wave' or the 'deBroglie wavelength' for a particle is related to its momentum p and Planck's constant h in the following way:

$$\lambda_{dB} = \frac{p}{h}$$

This implies that particles should be able to show interference effects like diffraction and two slit interference on encountering a structure that is of the order of their deBroglie wavelength. This hypothesis was soon confirmed by the famous Davisson-Germer experiment in 1923-27. They observed that electrons, when scattered off a nickel crystal, show a diffraction pattern which obeyed the Bragg condition [5]. This diffraction pattern was later observed by G. P. Thompson for the case of electrons bombarded on a thin celluloid in 1927 [6]. Davisson and Thompson were jointly awarded the 1937 physics

Nobel prize for these groundbreaking experiments. This ‘wave-particle duality’ was later found in other particles such as neutrons [7], neutral atoms [8] and molecules [9]. Matter-wave studies have led to a wide variety of real world applications. Electron microscopes are used to probe biological and mechanical structures at length scales 10^5 times smaller than the optical diffraction limit [10]. Neutron/helium diffraction has become an indispensable tool for solid state physics to probe material surface/structure properties [11, 12]. Diffraction and interference in large molecules is being used to test the spatial limit and other degrees of complexity to which quantum effects still remain observable [13]. Apart from these, matter-wave interference is also a prospective tool for precision measurement. This will be discussed in the next section.

1.2 Matter-wave Interferometry

The interference of light plays a key role in both cutting-edge science and real world applications. It has been instrumental in the development of astronomy, metrology, spectroscopy, etc to name a few. It was in the limelight for being at the core of the recent gravitational wave detection at the Laser-Interferometer Gravitational-Wave Observatory (LIGO) [14]. LIGO is the biggest interferometer ever constructed with its two arms measuring ~ 4 km each in a Michelson configuration. In the same spirit, matter-waves can also be manipulated and made to interfere forming an atom interferometer. Similar to the optical interferometer, the initial wavefunction is separated into two paths in momentum/position space and then recombined to observe interference. A major advantage such interferometers have over the optical ones is that matter interacts strongly with physical fields like gravity and electromagnetic. This makes precision measurement of these fields possible with matter-wave interferometers. Despite of these advantages, carrying out interferometry with matter-waves is more challenging because of two major reasons: 1. the smaller deBroglie wavelength resulting from the higher temperature of these particles makes it difficult to observe interference, 2. lack of straightforward optics to manipulate such particles while preserving coherence. The smaller deBroglie wavelength meant that the early matter-wave interferometry was carried out using lighter particles like electrons and neutrons. The first neutron interferometer made use of single crystal silicon for neutron beam manipulation [15]. It was

the first kind of matter-wave interferometer to measure gravitationally induced quantum interference [16]. The technique of neutron interferometry is used to study gravity [17], precision measurement of scattering lengths [18] and search for dark energy [19]. A downside of neutron interferometer's simplicity is that it requires state-of-the-art vibration isolation and precisely aligned crystal facets.

1.3 Atom Interferometry (AI)

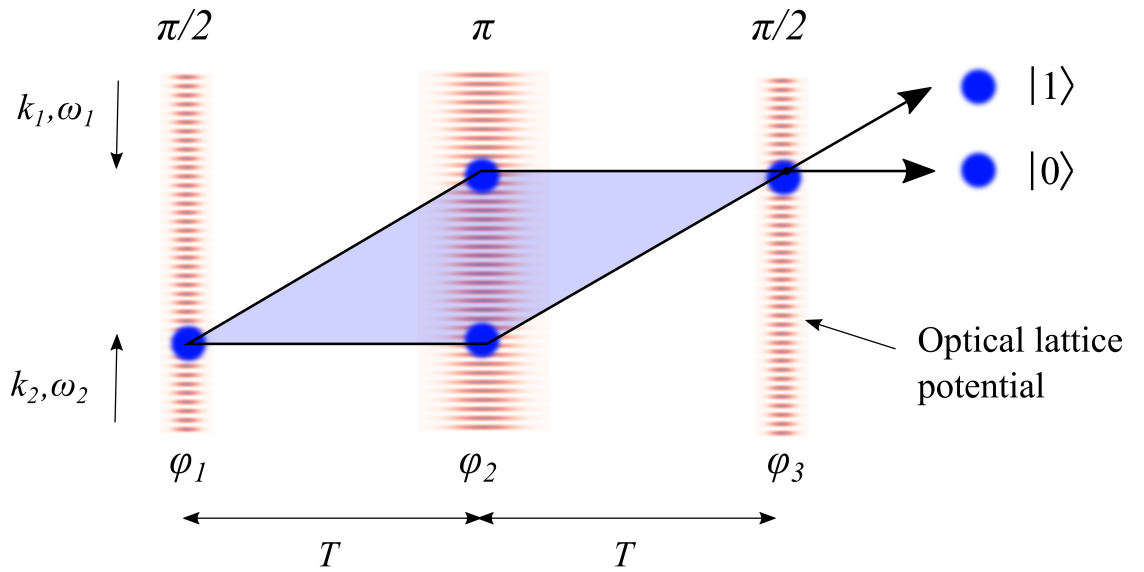


Figure 1.1: Atom interferometer in a Mach-Zehnder (MZI) configuration: The atomic cloud (blue sphere) is split and recombined by three pulses of a running wave optical lattice formed from the laser beams with wave-vectors k_1 , k_2 and frequencies ω_1 , ω_2 , thus forming an atom interferometer. The states $|0\rangle$ and $|1\rangle$ are the momentum states coupled by the Bragg interaction with the lattice. The interferometer sensitivity is directly proportional to the blue shaded area, which is the total area enclosed by the interferometer.

With the advancement in laser and cold atom technology, realization of matter-wave interferometer based on atoms became possible. The rapid improvements in techniques to generate ultra-cold atoms increased the attainable deBroglie wavelength of atom samples to $\sim 1 - 10 \mu\text{m}$ [20–22]. As mentioned before, the interferometric paths consist of differing momentum states and require diffracting elements for momentum state manipulation. Initially there were several demonstrations of AI with the diffraction optics consisting of micro-fabricated solid structures with silicon as the base material [23–25]. These were of transmission gratings with periodicity $\sim 0.1-1 \mu\text{m}$. For the case of atoms

these were later replaced with a more reliable stationary or running optical lattice red-detuned to the atoms resonant transition. The coupling between the optical field and the atoms is due to the induced electric dipole moment. By 1980s, the lasers had achieved sufficient spectral-densities to achieve coherent splitting in momentum via dipolar coupling as demonstrated by Pritchard et. al. for the case of sodium atomic beam [26]. Thus the tool-kit to create atom interferometers was ready.

We will now describe briefly a typical configuration used by AIs today. Figure 1.1 shows an AI schematic in a Mach-Zehnder configuration. The first such interferometer was demonstrated by M. Kasevich and S. Chu in 1991 [27]. The blue spheres represent a cold atomic ensemble undergoing momentum state manipulation via Bragg diffraction from pulses of an optical lattice potential. The first $\pi/2$ -pulse transfers puts the ensemble in a superposition of two momentum states $|0\rangle$ and $|1\rangle$ and can be considered as the beam splitter pulse. The π -pulse acts as a mirror pulse and inverts the momentum states of the two arms, thus refocusing them to interfere. The two momentum states finally interfere at the location of the final $\pi/2$ - pulse or the readout pulse. The readout state of the interferometer is dependent on the total phase $\Delta\phi$ gathered during the pulse sequence. In an optical interferometer there is a sinusoidal variation of intensity of the fringes when the path length is scanned. In an AI the fringe pattern is observed by monitoring the population in one of the states that varies with the total phase as $(1 + C \sin(\Delta\phi))/2$. Here, C is called the contrast of the interferometer. The interferometer signal can be scanned by varying the phase of the last $\pi/2$ -pulse. The phase uncertainty $\delta\phi$ in the fit to $(1 + C \sin(\Delta\phi))/2$, determines the sensitivity of the interferometer. Apart from the phase gathered from the lattice beams, any physical field present which interacts with the atoms also introduces a phase called the propagation phase in the interferometer [28]. As an example, the phase acquired due to gravitational acceleration g is given by $\Delta\phi_g = 2kgT^2$. These interferometers have typical integration times of ~ 10 ms which makes the total phase acquired due to gravity $\sim 10^5$ rad. Thus, an uncertainty in phase measurement of $\delta\phi \sim$ mrad which is typical, allows these interferometers to reach single shot sensitivities of $\Delta g/g \sim 10^{-9}$ level [29, 30].

The acceleration and rotation measurement performance of the standard AI configuration as described in Figure 1.1 can be compared to that of an optical interferometer.

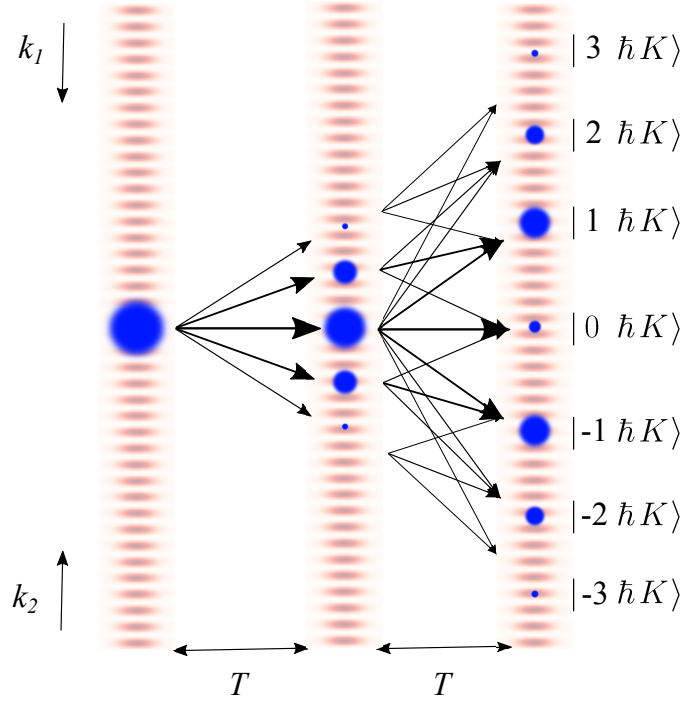


Figure 1.2: Multi-path interferometer schematic: The blue spheres represent cold atom cloud as the initial state with zero momentum in the frame of the optical lattice. The optical lattice pulses couple multiple momentum states (denoted by black arrows), in contrast with a standard two-path interferometer. Here $|n \hbar K\rangle$ denote the momentum state populated by the atomic ensemble on interaction with the lattice ($K = k_1 + k_2$).

In this configuration, an AI can measure rotation which occur perpendicular to the plane of its enclosed area (A). As derived in Ref. [31], the phase shift in an AI induced due to a rotation rate Ω is given by:

$$\delta_{atoms} = \frac{4\pi m A \Omega}{h}$$

Where, m is the mass of the atoms used in the AI. This phase shift occurs due to the Sagnac effect. For the case of an optical interferometer the corresponding phase shift is given by:

$$\delta_{light} = \frac{4\pi A \Omega}{\lambda c}$$

Where, λ is the wavelength of the light used in the interferometer and c is the speed of light. Thus the ratio of phase shifts can be used as a criteria for comparing the relative sensitivity of the interferometers. This ratio $R_{rotation} = \delta_{atoms}/\delta_{light} = m\lambda c h^{-1}$ can be as high as $\sim 10^{10}$ for a typical set of parameters. It is reduced to about $\sim 10^4$

due to two factors: 1. the fact that light makes multiple round-trips in an optical ring gyroscope in the time that the AI takes to close once and 2. the flux of cold atoms is much less in comparison to photon flux of a laser source. Among the state-of-the-art AIs, a rotation sensitivity of 3×10^{-10} rad/s (Earth's rotation rate = 7.29×10^{-5} rad/s) has been demonstrated which is in favorable comparison to the state-of-the-art fiber optic gyroscopes [32].

AI has undergone rapid developments over decades and the current generation interferometers rival the optical interferometers in absolute gravity [30, 33–36], gravity-gradient [37–39] and magnetic field gradient [34, 40] measurement sensitivities. Unlike other gravimeters like the falling corner-cube interferometer, AI has no moving parts and is thus ideal for on field applications like air/ship borne gravity surveys [41, 42], aid marine navigation in GPS denied environments [43], monitoring seasonal aquifer changes [44], gravity reference for a Kibble balance [45], etc. AI also has been an ideal test-bed for exploring fundamental physics experiments such as testing the equivalence principle [46], detecting dark energy [47], precision measurements of the fine structure constant [48] and the gravitational constant [49], tests of quantum superposition at large length scales [50] etc. AI also lies at the core of the MIGA (Matter Wave laser Interferometric Gravitation Antenna) experiment which aims to detect gravitational waves in a frequency band (100 mHz-1 Hz) not accessible to current generation light based gravitational wave detectors [51]. When MIGA reaches design sensitivity, it will allow observation of the low-frequency gravitational waves which begin years before the final in-spiral phase of the black-hole mergers.

The interferometers explored above only utilize two momentum states in their working. This simplifies the readout and the associated uncertainties in it. Although a better AI architecture is unlikely to emerge, a new interferometric scheme can be advantageous for specific applications such as the measurement of atomic recoil frequency and gravitational acceleration. One such non-standard configuration of AI are called multi-path interferometers, which utilize more than two momentum states. The next section describes a few leading realizations of multi-path interferometers.

1.4 Multi-path atom interferometers

As shown in Figure 1.2, the primary difference between the traditional two-port and the multi-path interferometers is that there are multiple interferometer loops present. For the two path interferometers this type of coupling is undesired and such loops are known as parasitic interferences [52]. However, certain multi-path schemes have been shown to perform competently with the standard AI configuration for the measurement of atomic recoil frequency and the acceleration due to gravity. The recoil frequency ω_r is defined as the $E_r = \hbar\omega_r$, where E_r is the energy imparted to the atoms after exchange of a photon pair from the diffracting optical lattice. The measurement of recoil frequency is one of the sought after pursuits of atom interferometry as it is directly related to the precision measurement of the fine structure constant (α). α characterizes the strength of interaction between elementary charged particles and thus holds an important place in the Standard model. Currently, Holger Müller's group at the University of Berkeley holds the record of measuring α with an uncertainty of 0.2 parts per billion (ppb) with a Ramsey-Bordé interferometer and it reveals a 2.5σ tension between the value measured by alternative means [53]. Alternative measurement of α is important as such discrepancies between measurement techniques may point towards new physics.

One of the first demonstrations among the multi-path interferometers used a superposition of atomic ground states with different momenta, where a pair of counter-propagating beams put the atoms in a non-absorbing dark state [54]. Due to multi-beam interference, the phase-readout is like an Airy pattern rather than a sine wave analogous to a Fabry-Pérot interferometer output. Though the transfer efficiency to higher momentum states was high in this type of interferometer, eventually it was succeeded by optical lattice based techniques. A leading contender capable of reaching ppb level of accuracy is the contrast interferometer (CI). This interferometer uses a Bose-Einstein Condensate (BEC) as the source and is arranged in a symmetric three path configuration [55]. An important advantage that CI has over traditional interferometry is that the recoil phase is recorded in the contrast of the output signal and not its phase. This makes the readout inherently immune to lattice vibration noise which is an important systematic effect that has to be considered in two-path interferometers. The next list of multi-path interferom-

$$\alpha = \left[2 \frac{R_\infty}{c} \frac{M}{m_e} \frac{h}{M} \right]^{1/2}$$

Rydberg constant
0.007 ppb

Rb⁸⁷ mass
0.075 ppb

Electron mass
0.03 ppb

Determined by
atomic recoil frequency
 $\frac{h}{M} = \frac{4\pi c^2 \omega_r}{\omega^2}$

Figure 1.3: Measurement of the fine structure constant (α): The uncertainty in the Rydberg constant and rubidium mass is taken from Ref. [1]. The uncertainty in the electron mass value is taken from Ref. [2]. ω denotes the angular frequency corresponding to the optical lattice wave-vector.

eters we introduce are based on a phenomenon known as the matter-wave ‘Talbot-Lau’ effect. We will briefly introduce this effect in the next section.

1.4.1 The Talbot effect

The Talbot effect in light was first reported by H.F. Talbot in 1836 [56]. On illuminating a grating with a sunbeam and imaging the transmitted light via a lens, he observed sharp lines or bands of colors, the direction of which was parallel to the lines of the grating. In his report he described the patterns as being sharp enough to be compared to a “tissue woven with colorful thread”. On traversing the distance between the lens and the grating, these bands repeated distinctly and indefinitely even when the grating was greatly out of focus of the lens. The occurrence of this repetition of band patterns was later explained to be a natural consequence of near field diffraction by Lord Rayleigh in 1881 using the Fresnel diffraction theory [57]. He derived the distance interval between two such revivals of the grating intensity pattern to be a^2/λ . Figure 1.3 shows this reappearance of the intensity pattern repetition having a spatial periodicity of the grating period. calculated near field pattern for a grating. This “lens-less” focusing and

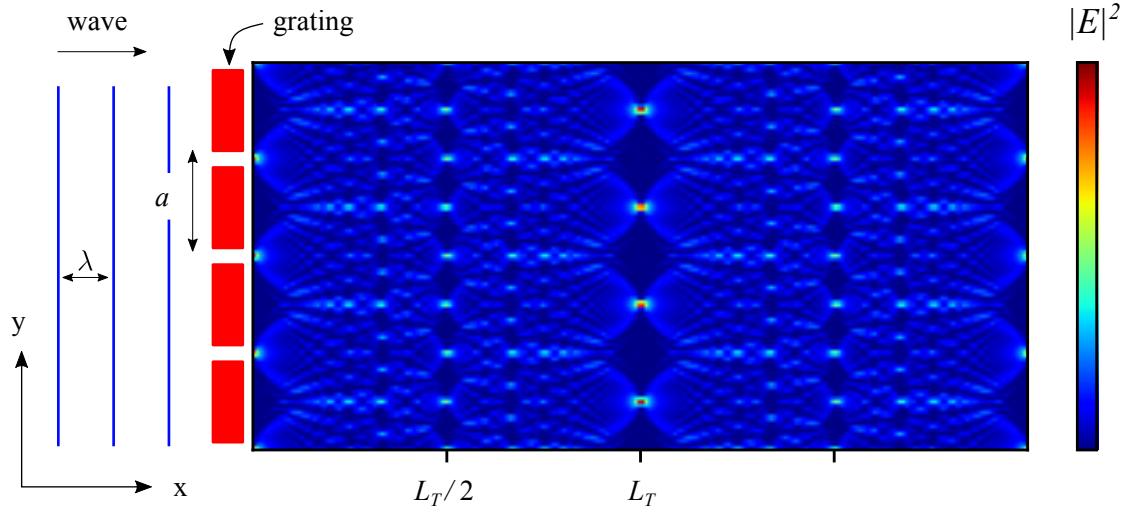


Figure 1.4: The optical Talbot effect: Simulated intensity profile $|E|^2$ of a plane wave with wavelength λ incident from the left on a grating with period a . The color bar on the right is an indicator of the same (intensity = $|E|^2$, E being the electric field amplitude). The intensity pattern is repeated with a shift of $a/2$ in the y -direction after integer multiples of L_T . The fractional Talbot effect at $x = L_T/2$ is also visible.

self-imaging of the grating structure enables numerous applications of this effect in the optical domain such as creating accurate grating copies [58], Talbot array illuminators as optical interconnects [59], Talbot cavities for phase locking of a laser diode array [60], X-ray phase contrast imaging of soft tissue [61], EIT based imaging of atoms [62], etc. Since this phenomenon is based on coherent interference of waves, it has also been observed in other quantum mechanical systems as well for example: surface plasmon polaritons [63], molecular beams [64], atomic systems [25] etc.

In the case of atomic systems, the spatial Talbot effect was first demonstrated for a beam of Na atoms [65]. Apart from the spatial Talbot effect, a temporal version of the effect also exists for the case of matter-waves. In this ‘temporal Talbot effect’, the wavefunction of the atoms/molecules diffracting from a pulsed optical lattice undergoes periodic revivals in time. The time period of these revivals is called the Talbot time. The origins of this Talbot effect lie in the discrete nature (in integral units of $\hbar K$) of the momentum exchange from interaction with the optical lattice. To observe this effect with good signal-to-noise ratio (SNR), the atomic ensemble must possess a sub-recoil momentum width ($\sigma_p \ll \hbar K$) and thus it was demonstrated first for the case of a

BEC [66]. This near-perfect revival of the initial state in the ‘BEC + pulsed optical lattice’ system, also called as the BEC δ -kicked rotor. In the δ -kicked rotor, the BEC is subjected to a series of sharp Dirac- δ like pulses of a far detuned optical potential. It is an experimental realization of the quantum δ -kicked rotor Hamiltonian [67]. The classical version of the Hamiltonian displays chaotic behavior in a certain parameter regime and some signatures of this chaotic behavior is imprinted in the quantum dynamics. This makes it a paradigmatic model for quantum chaos studies such as: chaos assisted quantum dynamical tunneling [68], quantum-accelerator modes [69], quantum ratchets [70], etc. A more detailed description of quantum chaos is given in chapter 4. The BEC δ -kicked rotor system is also an emerging platform for executing highly controllable quantum walks, where the atomic spin constitutes the internal coherent ‘coin state’ which is entangled with the external momentum state [71].

The measurement of Talbot time (T_T) is equivalent to that of the single-photon recoil frequency as $T_T = \pi/2\omega_r$. An attractive feature of measuring Talbot time in the δ -kicked rotor is that the signal width has been shown to display sub-Fourier scaling with the interrogation time i.e $\Delta f \times T < 1$ (Δf being the frequency resolution) [72]. This type of scaling has been shown with BEC based δ -kicked rotor, where the Talbot time measurement resolution increased as N^2 , N being the number of pulses [73]. In chapter 5, we explore in detail a BEC δ -kicked rotor scheme which is even more sensitive where the resolution scales as N^3 . Apart from these BEC based approaches there have been promising demonstrations of cold atom based recoil frequency measurement schemes. These schemes are based on the Talbot-Lau effect, which is the Talbot effect analog for incoherent ensembles ($\sigma_p \gg \hbar K$).

1.4.2 The Talbot-Lau effect

In an initial ensemble with a broad distribution of momentum $\sigma_p \gg \hbar K$, each momentum state carries a different Doppler shift. After the first optical lattice pulse, the diffracted wavefunction originating from each momentum state revives after Talbot time but due to the different Doppler shifts, the net effect gets washed out and there is no clear spatial pattern in the atomic distribution. If two pulses with a temporal separation of $T = nT_T/2$ (n being a positive integer) are applied, the density distribution

at time T after the second pulse is spatially periodic consisting of several components at integer multiples of the optical lattice vector K . In the double pulse approach, the Doppler shifts get canceled out at time $2T$ after the first pulse [74]. This is analogous to realizing a double slit experiment with an incoherent light source, where a single slit is required between the illumination and the double slit arrangement to observe interference. The contrast of the density modulation periodically repeats in intervals of the recoil frequency $2\omega_r$, and the readout of this pattern constitutes measurement of the recoil-frequency.

In Ref. [75], ω_r was measured with a statistical precision of 37 ppb using Talbot-Lau interferometer geometry. Here, the readout of the spatial modulation was carried out by back-scattered light from the Bragg structure formed due to the interference. The cold atom Talbot-Lau interferometer was also demonstrated to be capable of performing ppm level measurement of local gravity [76, 77]. Here, a dissipative mechanism was used where the lattice light was tuned very close to the resonance. At each pulse only the atoms which fell at the nodes of the periodically repeating structure and the lattice light survived. Monitoring these ‘survival resonances’ enabled measurement of gravitational acceleration.

The Talbot-Lau interferometer is also used for studying the quantum interference of large molecules (mass ~ 800 -2000 amu), where the deBroglie wavelength is orders of magnitude lesser than the size of the molecules [78, 79]. The study of quantum interference in such large and complex structures helps in answering fundamental questions about decoherence and quantum to classical transition [80]. It is also used to study the magnetic and electronic properties of large molecules [81].

1.5 Objective of the thesis

As discussed in section 1.4.1, there are BEC based δ -kicked rotor schemes where the Talbot time measurement resolution scales favorably with the interrogation time. This thesis explores the utility of a particular scheme proposed in Ref. [82]. It sets up the simulation and experimental methods that are required to carry out δ -kicked rotor experiments with BEC. The experimental results that are obtained, confirm for the first time, the theoretical constraints placed on the measurement scheme proposed in Ref. [83].

These were not observed in the earlier experiment [84]. These findings are also relevant in light of the recent revival of the BEC δ -kicked rotor platform for conducting quantum random walks [71].

In addition to the above, the thesis presents two previously unexplored asymmetry effects in the momentum distribution of the BEC δ -kicked rotor. Based on these, we suggest an alternative way of measuring the Talbot time and the lattice phase. In another atom-light interaction regime, where the optical lattice pulse duration can no longer be approximated as a Dirac- δ function, we study the preparation of initial states with a net non-zero momentum using Bragg diffraction. These states in combination with the δ pulses were then used to demonstrate a controllable quantum ratchet. This demonstration paves the way for next generation of BEC based δ -kicked rotor experiments where the dynamics can be tuned by controlling the initial state preparation [85, 86]. Bragg diffraction was also used to measure the momentum distribution of the BEC, which is an important factor that affects the δ -kicked rotor experiments.

1.6 Organization of the thesis

Chapter 2 describes the production of the Bose-Einstein condensate (BEC) of ^{87}Rb atoms via laser cooling in a Magneto-Optical Trap (MOT) and evaporative cooling in a hybrid crossed Optical Dipole Trap (ODT). Simplified expression for the scattering force in a MOT and the conservative force in an ODT for a two level system is derived. The chapter also discusses the BEC wavefunction confined in a harmonic potential and the effects of repulsive interactions on it. This gives an estimate of evolution of the momentum width of the BEC after releasing it from the trap.

Chapter 3 describes the coherent diffraction of the BEC in different regimes when subjected to a far detuned optical lattice potential. Two extreme interaction regimes are discussed i.e the Raman-Nath regime where the lattice potential is relatively high and interaction time is short and the Bragg regime where the conditions are vice versa. The optical and electronic layout for the preparation and control of the optical lattice is also briefly discussed.

Chapter 4 introduces the δ -kicked rotor Hamiltonian. Classical dynamics and approach to the chaotic regime is briefly discussed. The quantum version of this Hamil-

tonian can be realized with the Atom Optics δ -Kicked rotor (AOKR). The quantum dynamics can be classified broadly in two regimes i.e the generic ‘dynamical localization’ where the wavefunction is effectively ‘frozen’ due to destructive interference and the ‘quantum resonances’ where the system undergoes ballistic growth in energy.

Chapter 5 introduces a BEC based AOKR pulse scheme to measure the Talbot time. The scheme relies on the initial state revival or the fidelity, under the action of the optical lattice pulses. For a plane wave initial state, it is expected that the scaling of the measurement sensitivity of this scheme goes up as N^3 , where N is the number of pulses in the sequence. This sub-Fourier scaling is highly desirable for the measurement of Talbot time. The effect of momentum width of the BEC on the performance of the pulse scheme is discussed. We find that the scaling of measurement sensitivity deviates from the cubic law due to the finite momentum width. We also demonstrate the AOKR functioning as a momentum filter due to the momentum sensitivity of the pulse sequence to quasi-momentum.

Chapter 6 describes two different types of asymmetries in the momentum distribution of the BEC based AOKR, which are a function of the relative phase of the optical lattice between pulses. This chapter discusses this ‘intra-order’ and ‘inter-order’ asymmetry which occur at the Talbot time and away from the Talbot time respectively.

Chapter 7 describes the realization of a quantum-ratchet using AOKR dynamics. The initial state is placed in a superposition of the first and the zeroth order momentum state using Bragg diffraction. The subsequent application of AOKR pulse sequence induces a net momentum current in the system which grows with the number of pulses, thus forming a quantum ratchet. The direction of this momentum current is a function of the relative phase between the AOKR lattice and the Bragg diffraction lattice.

Chapter 8 describes the numerical methods used for simulating the AOKR dynamics. The simulations are done using the split-operator method where, the free propagation operator is diagonal in momentum space and the optical lattice kick operator is diagonal in position space in the δ -kick approximation. The numerical code is implemented in Python 2.7.

Chapter 9 is the concluding part of the thesis which summarizes the work. Based on the experiments presented in this thesis, suggestions are listed for the future experiments

that can be carried out in the ^{87}Rb BEC setup.

Appendix section describes phase noise characterization using optical interferometry, Bragg spectroscopy for BEC momentum width measurement and absorption imaging theory.

Chapter 2

Introduction to laser cooling and Bose-Einstein Condensate

This chapter elucidates the principles of laser cooling of atoms and the subsequent production of a Bose-Einstein condensate (BEC) of ^{87}Rb atoms. The atoms are first trapped and cooled to sub-Doppler temperature in a Magneto-Optical Trap (MOT) and are then transferred to a far-detuned optical dipole trap for evaporative cooling. The atomic gas reaches the BEC state at the end of the evaporative cooling cycle. We briefly discuss the ground state of the BEC under harmonic confinement and its expansion after release from the trap.

2.1 Phase space density (PSD)

The ultimate goal of cooling techniques that are described below is to reach the quantum degenerate state i.e the Bose-Einstein condensate. Before we introduce the concepts behind laser and evaporative cooling, we define phase-space density (PSD). PSD is a metric that is useful for quantifying the overlap between the current state of the atomic cloud and the quantum degenerate state. It is defined as:

$$\rho = n\lambda_{dB}^3 \quad (2.1)$$

Where, n is the density and $\lambda_{dB} = h/\sqrt{3Mk_B T}$ is the deBroglie wavelength of the atoms. For an un-trapped gas, the BEC phase transition occurs at $\rho \simeq 2.612$ [87].

Typically, an atomic gas starts its journey towards BEC at $\rho \sim 10^{-10}$ [88]. We now discuss the cooling techniques that lead to a gain in PSD.

2.2 The two-level system

To understand the optical forces behind laser cooling, it is useful to model the atom-light interaction using a two-level system. This reduction of multi-level atomic states is valid as long as the light addressing the relevant transition possess narrow frequency spread, which is true for the case of laser radiation [89]. The two-level atomic wavefunction can be given by:

$$|\psi(t)\rangle = C_a(t)e^{-i\omega_a t} |a\rangle + C_b(t)e^{-i\omega_b t} |b\rangle \quad (2.2)$$

Where, $|a\rangle$ and $|b\rangle$ represent the eigenkets of the bare Hamiltonian without the electromagnetic interaction. Separating out the $e^{-i\omega t}$ terms from the complex coefficients, we ensure that $C_a(t)$ and $C_b(t)$ are influenced only by this interaction. The term describing the interaction between the atomic electron (charge q) and an electromagnetic field with the electric field vector $\vec{E}(\vec{R}, t)$, is given by:

$$V = -\vec{d} \cdot \vec{E}(\vec{R}, t) \quad (2.3)$$

Here $\vec{d} = q\vec{r}$ is the dipole moment, \vec{r} is the position vector of the electron and \vec{R} is the same for the center of mass of the atom. This interaction term is valid in the limit that the electric field doesn't change appreciably over the size of the atom and is known as the *electric dipole approximation* [88]. Unless the atom has a permanent electric dipole moment, the diagonal matrix elements of the interaction term like $\langle a|V|a\rangle$ will vanish. Thus, the off-diagonal matrix elements are given by:

$$V_{ab} = -d_{ab}E(\vec{R}, t) \quad (2.4)$$

Where, $d_{ab} = \langle a|q\vec{r} \cdot \hat{E}|b\rangle$ is the component of the dipole vector along the direction of the electric field. Since this matrix element couples the two states, it can be called as the transition matrix element. Consider an electric field oscillating with frequency ω_l i.e. $E(t) = E_0 \cos(\omega_l t)$. Ignoring the spatial dependence, for this oscillating electric field,

the transition matrix element becomes:

$$V_{ab} = -d_{ab}E_0 \cos(\omega_l t) \quad (2.5)$$

We now proceed to derive how this oscillating electric field affects the time evolution of the two states. To make calculations convenient, we use a unitary transformation on the state vector $|\psi\rangle$, such that:

$$|\psi(t)\rangle = C_a(t)e^{i(\delta/2-\omega_a)t} |a\rangle + C_b(t)e^{i(-\delta/2-\omega_b)t} |b\rangle \quad (2.6)$$

Where $\delta = \omega - \omega_l$ is the frequency detuning of the radiation from resonance. Substituting Eq. 2.6 in the Schrödinger's equation gives rise to two coupled differential equations in C_a and C_b . These equations are:

$$\dot{C}_a + i\frac{\delta}{2}C_a = i\frac{E_0 d_{ab}}{2\hbar}C_b \quad (2.7)$$

$$\dot{C}_b - i\frac{\delta}{2}C_b = i\frac{E_0 d_{ba}}{2\hbar}C_a \quad (2.8)$$

The term $\Omega = E_0 d_{ba}/\hbar$ is termed as the ‘Rabi frequency’ of the transition. These equations are used to derive the two kinds of forces resulting from the dipolar interaction. These forces are used to cool and confine the atomic sample and will be discussed in the subsequent sections.

2.2.1 The scattering force

The success of cold atom experiments comes from their ability to confine and cool down atoms in a highly controllable manner. At the centerpiece of these experiments is the technique of laser cooling. This method of cooling relies on the near resonant scattering of laser light by atoms. The properties of the radiation field can be tailored such that it also provides spatial confinement. We will now take a look at some basic concepts that are behind this cooling technique.

The subsequent discussion is for a two level atom. The dynamics of the two level

system can be recast in terms of the density matrix, which is defined as:

$$|\Psi\rangle\langle\Psi| = \begin{pmatrix} \tilde{C}_a \\ \tilde{C}_b \end{pmatrix} (\tilde{C}_a^* \quad \tilde{C}_b^*) = \begin{pmatrix} \rho_{aa} & \rho_{ab} \\ \rho_{ba} & \rho_{bb} \end{pmatrix} \quad (2.9)$$

Where, $\tilde{C}_a = C_a e^{i\delta t/2}$ and $\tilde{C}_b = C_b e^{-i\delta t/2}$. The Schrödinger equation can be now written as a set of three coupled differential equations in terms of the density matrix elements. These equations are collectively known as the optical Bloch equations:

$$\dot{u} = \delta v \quad (2.10)$$

$$\dot{v} = -\delta u + \Omega w \quad (2.11)$$

$$\dot{w} = -\Omega v \quad (2.12)$$

Where, $u = \rho_{ab} + \rho_{ba}$, $v = -i(\rho_{ab} - \rho_{ba})$ and $w = \rho_{aa} + \rho_{bb}$. We now incorporate the effect of spontaneous emission on these equations such that the population of the excited state decays with a time constant Γ . Therefore, $\rho_{aa}(t) = \rho_{aa}(0)e^{-\Gamma t}$. Under steady state conditions $t \gg \Gamma^{-1}$ and strong driving $\Omega \rightarrow \infty$, the Bloch equations can be used to derive the population of the excited state [88]:

$$\rho_{aa} = \frac{\Omega^2/4}{\delta^2 + \Omega^2/2 + \Gamma^2/4} \quad (2.13)$$

Thus, the force imparted by the field with wave-number $k = 2\pi/\lambda$ and light intensity I :

$$F_{scattering} = \hbar k \rho_{aa} \Gamma = \hbar k \frac{\Gamma}{2} \frac{I/I_s}{1 + I/I_s + 4\delta^2/\Gamma^2} \quad (2.14)$$

Where, $I_s = \pi\Gamma\hbar c/3\lambda^3$ is defined as the saturation intensity of the transition. In conjunction with a varying magnetic field, this scattering force force is first employed to slow down the atoms from the heated atomic reservoir in cold atom experiments. This is done in the form of a laser beam pointed in a direction anti-parallel to the oven flux . A spatially varying magnetic field is also utilized to keep the slowed atoms near resonance by using the Zeeman effect. This setup is called the Zeeman slower and is an essential first stage as the potential depth of the subsequent traps which are used is not enough for efficient capture of the hot atoms emanating from the oven [90]. For typical

alkali metal experiments, it can slow down atoms to milli-Kelvin temperatures in about a meters distance [91]. More details of the Zeeman slower that is used in our setup, are described elsewhere [92,93]. After the atoms have been slowed down, they are captured by another trap which employs the resonant scattering force and a quadrupole magnetic field. This trapping configuration is called a magneto-optical trap (MOT) and will be discussed in the next section.

2.3 The magneto-optical trap (MOT)

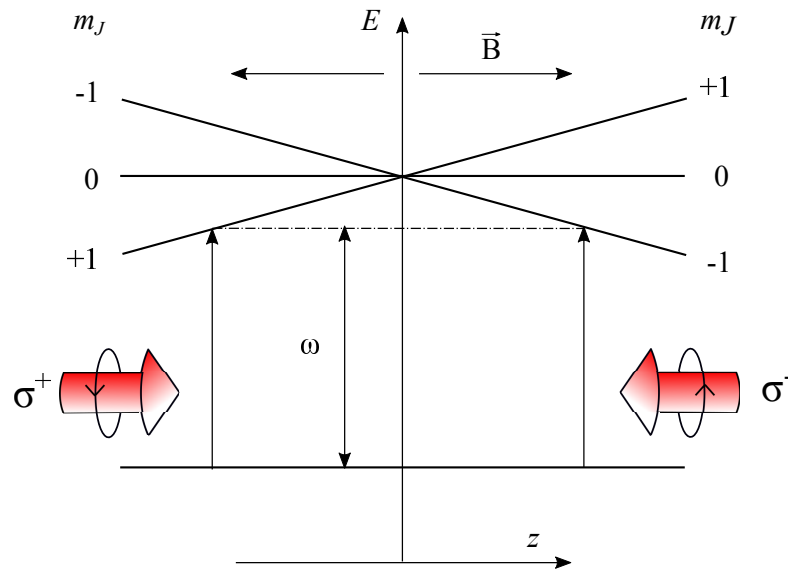


Figure 2.1: MOT schematic for $J = 0 \rightarrow J = 1$ transition. The Zeeman splitting (exaggerated in the figure) caused by the magnetic field gradient causes preferential absorption of light from either the σ^+ or the σ^- beams depending on the atoms position along the z -axis. This position dependent imbalance between the imparted force from the two beams drives the atoms towards $z = 0$ resulting in a net confinement.

The magneto-optical trap (MOT) uses a combination of six red-detuned laser beams arranged in orthogonal pairs along with a quadrupole magnetic field to achieve confinement of neutral atoms. It has been a work-horse for cold atom experiments and is the first trap that the atoms encounter after being slowed down by the Zeeman slower. The captured atoms can then be transferred to other traps for further experiments. The spatially varying magnetic field induces a Zeeman shift in the atoms, causing an imbalance in the absorption from a pair of orthogonal laser beams thus creating a trapping

configuration.

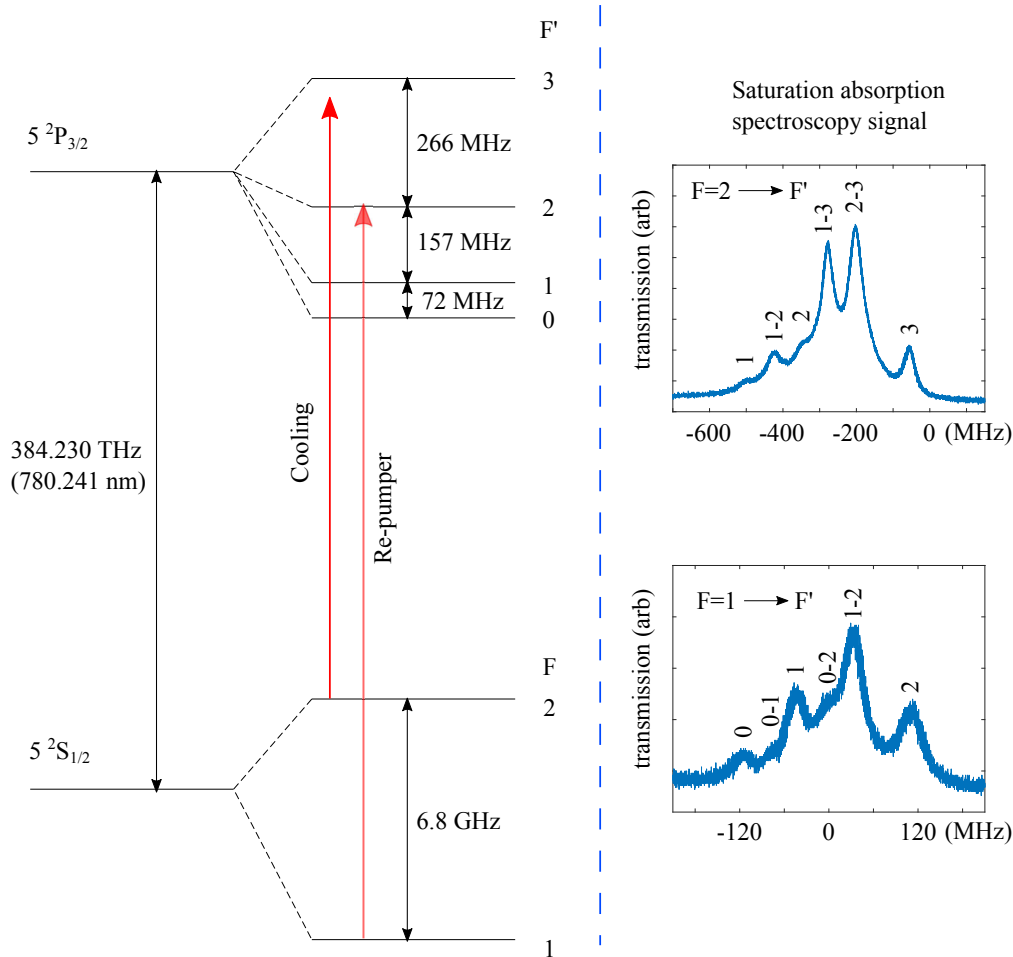


Figure 2.2: ^{87}Rb D2 line: **(Left)** The energy level diagram of the D2 transition with hyperfine splitting. The cooling laser is red detuned by about 2Γ from $|F = 2\rangle \rightarrow |F' = 3\rangle$, where $\Gamma = 2\pi \times 6$ MHz while the repumper is almost resonant to the $|F = 1\rangle \rightarrow |F' = 2\rangle$ transition. **(Right)** the saturation absorption spectroscopy signal which is used to lock the lasers on the relevant transitions. The numerals on top of the spectra denote the F' state. The lines which possess two numbers represent the cross-over resonances.

We now discuss this mechanism for a simplified $|J = 0\rangle \rightarrow |J = 1\rangle$ transition. As shown in the Figure 2.1, the degeneracy of the excited state $|J = 1\rangle$ is broken by the magnetic field gradient and it splits into three magnetic sublevels $m_J = -1, 0, +1$. To have selective absorption on the transitions $|J = 0, m_J = 0\rangle \rightarrow |J = 1, m_J = \pm 1\rangle$, pairs of orthogonal beams have circularly polarized light with opposite helicity. On the left side of the $B = 0$ axis, the beam having σ^+ polarization is absorbed and scattered

preferably in comparison to the σ^- beam due to the detuning of the σ^+ beam being closer to the laser frequency. In addition to this, according to the selection rules for electric-dipolar transition, absorption of the σ^+ beam is favored over the σ^- beam. This pushes the atoms towards the field zero resulting in confinement. It can be seen that the detuning and the field gradient decides the spatial point at which the maximum absorption takes place and hence the extent of the trap. Thus, the trap can be compressed by reducing the detuning or ramping up the field gradient. In addition to confinement, the atoms also undergo cooling in all directions, due to the directional absorption and scattering in random direction. The atoms undergo a random walk in momentum space due to these scattering events and it can be shown that the ultimate limit on the reduction of kinetic energy via these processes has a limit [88]. This is called ‘the Doppler limit’ and its temperature equivalent is given by:

$$k_B T_{Doppler} = \frac{\hbar\Gamma}{2} \quad (2.15)$$

Figure. 2.2 shows the energy level diagram of the D2 line of ^{87}Rb . The transition used for cooling is $|F = 2\rangle \rightarrow |F' = 3\rangle$. For cooling, the laser beams are kept red-detuned at -2Γ where, Γ is the natural linewidth of the cooling transition ($\sim 2\pi \times 6$ MHz) and the magnetic field gradient is about 13 Gauss/cm. The value of Γ puts the laser cooling Doppler limit at $\sim 146 \mu\text{K}$. Since the detuning is enough to cause finite spontaneous emission an additional repumping laser is required at $|F = 1\rangle \rightarrow |F' = 2\rangle$ bring the atoms back to the cooling cycle. The apparatus for generation of this cooling light is described in more detail in the following works Ref. [92, 93].

In order to further cool and increase the density of the trapped atoms (causing a corresponding increase in PSD), the atoms have to be transferred to a different trap which has a smaller volume than MOT [94]. Thus to facilitate the transfer, the MOT field gradient is increased to 22 G/cm over 40 ms to compress the atomic cloud and the repump beam is gradually extinguished. The detuning is also increased to -12Γ in order to decrease the atom-atom repulsion effects due to photon re-absorption [95]. This is called as the compressed MOT technique. Due to the limitations on laser cooling discussed before, further cooling has to be done using another kind of technique called

the evaporative cooling. This is done in an optical dipole trap which will be discussed in the next section.

2.4 The optical dipole trap

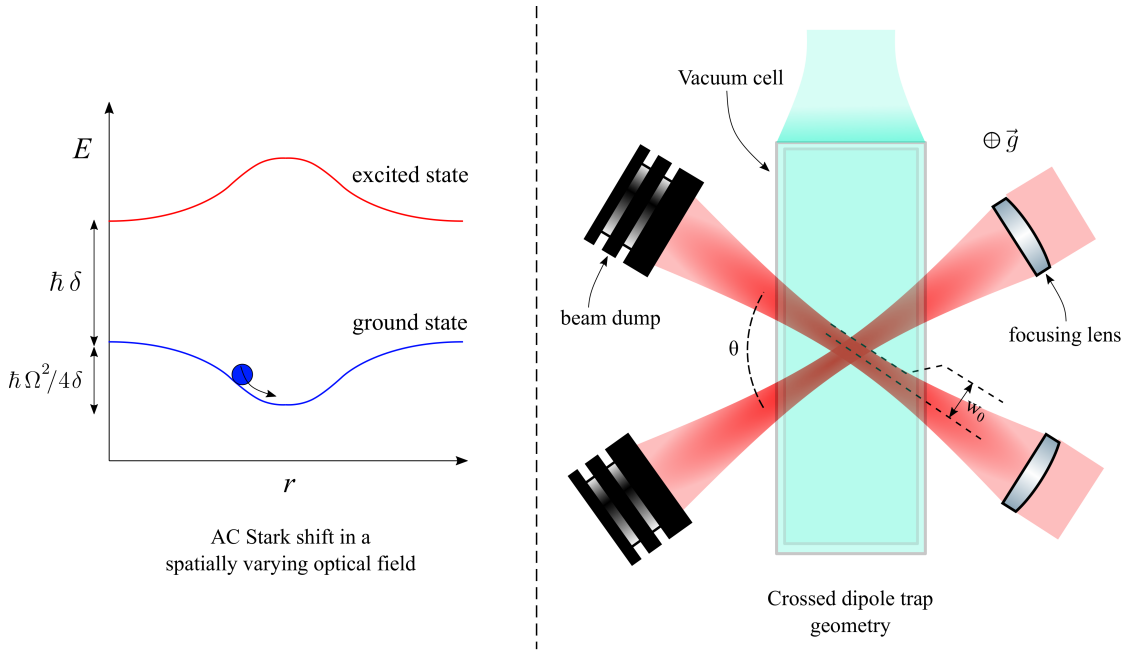


Figure 2.3: The AC Stark effect. (Left) The spatially varying energy splitting between the ground and the excited state of the ‘atom+light field’ system for a negative detuning δ . The blue sphere represents the atoms which are attracted towards the point where the down shift in energy is the highest i.e the point of highest intensity of the beam. (Right) Schematic of the far-detuned crossed dipole trap configuration used in our setup. A pair of 1064 nm laser beams are focused at the position of the atoms with a beam waist ($2w_0$) of about $70 \mu\text{m}$. The initial power in the beams is about 6 W, providing confinement potential in the range of $\sim 100\text{s } \mu\text{K}$.

To understand the origin of the optical dipole first let us recast the equations derived previously for the two-level system interacting with a monochromatic light field i.e Eq. 2.7 and 2.8:

$$i\frac{d}{dt}\begin{pmatrix} C_a \\ C_b \end{pmatrix} = \begin{pmatrix} \delta/2 & -\Omega/2 \\ -\Omega^*/2 & -\delta/2 \end{pmatrix} \begin{pmatrix} C_a \\ C_b \end{pmatrix} \quad (2.16)$$

Here, $\Omega = E_0 d_{ab}/\hbar$ is the resonant Rabi frequency of the transition. This system has solutions of the form:

$$\begin{pmatrix} C_a \\ C_b \end{pmatrix} = \begin{pmatrix} a \\ b \end{pmatrix} e^{i\lambda t} \quad (2.17)$$

The phase term λ can be calculated from solving the determinant of the matrix in Eq. 2.16 and comes out to be $\lambda = \pm\sqrt{\delta^2 + \Omega^2}/2$. As shown in Figure 2.3, in the absence of interactions ($\Omega = 0$), the two states can be interpreted as being separated by δ . Typically for the optical dipole traps employed in cold atom experiments, the trapping laser is kept far detuned from the resonant transition to reduce decoherence due to spontaneous emission [96]. Therefore, in the limit $\delta \gg \Omega$:

$$\lambda = \pm \left(\frac{\delta}{2} + \frac{\Omega^2}{4\delta} \right) \quad (2.18)$$

The eigen-states corresponding to the two values of λ are called the ‘dressed states’ of the atoms and contain a superposition of the atomic ground and excited state [88]. The energy separation between these two states in the absence of the dipolar interaction is $\hbar\delta$. The presence of light induces a shift in these two states w.r.t the unperturbed energies and is called the ‘light shift’ or ‘AC Stark shift’. In the presence of a spatially varying laser field, the shift in the state having lower energy can be considered as a potential and the atom feels a conservative force as the gradient of this potential field:

$$U_{dipole} = -\frac{\hbar}{4\delta}\Omega^2(r) = -\frac{\hbar\Gamma^2}{8\delta I_s}I(r) \quad (2.19)$$

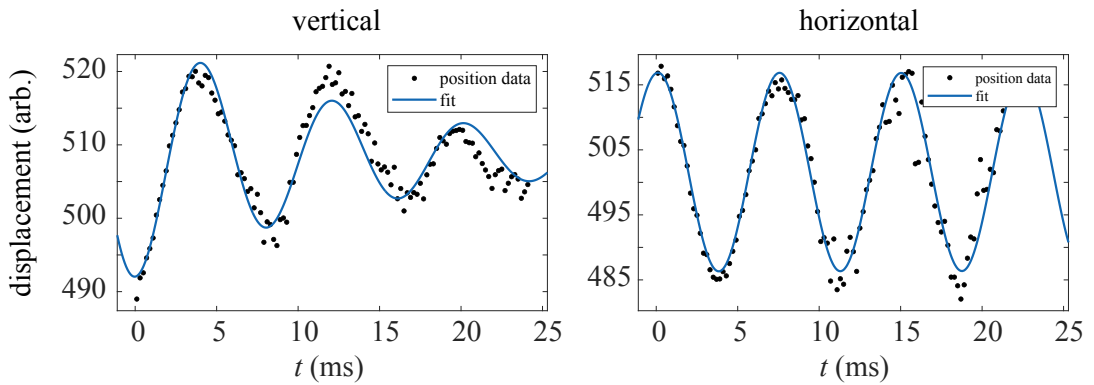


Figure 2.4: Trapping frequency measurement: Atoms were given an impulse of magnetic field force and allowed to oscillate for a variable time t in the optical dipole trap before being released. The y-axes of the plots denote the displacement after a period of time-of-flight which captures the velocity of the atoms when the trap is turned off. Vertical ($2\pi \times 122 \pm 5$ Hz) and horizontal ($2\pi \times 134 \pm 7$ Hz) denote orientation w.r.t gravity.

For a red-detuned field the potential minima occurs at the point of highest intensity. Thus a far detuned focused laser beam can be used to create a confinement for the atoms. This type of trap is called a far-detuned optical trap (FORT) and is an alternative to magnetic traps for carrying out evaporative cooling and ultimately achieving BEC. For a Gaussian beam with waist w_0 and peak intensity I_0 , the transverse dipole potential is given as:

$$U_{dipole} = -\frac{\hbar\Gamma^2 I_0}{8\delta I_s} e^{-2r^2/w_0^2} \quad (2.20)$$

For alkali atoms, this type of trap provides a trap depth in the range of $\sim 100 \mu\text{K}$ using commercially available high power infra-red (IR) lasers and thus can capture atoms with good efficiency from MOT. As shown in Figure. 2.3 (right), the dipole trap in our setup is arranged in a crossed beam configuration. The two beams are derived from a 20 Watt IR fiber laser (IPG photonics, YLR-20-1064-LP-SF). The initial beam is split into two paths, each one going through an acousto-optic modulator (AOM) for intensity control. The two beams are then focused to achieve tight 3-D confinement for atoms. We also keep the magnetic field gradient on at a value of 24.7 Gauss/cm to support the crossed dipole trap in the direction of gravity. This configuration is explained in more detail in Ref. [93]. One can characterize the harmonic confinement of this trap by measuring the trapping frequencies along different axes. This is done by giving an impulse to the atoms to displace them and observing the resultant oscillations in position. Fig. 2.4 demonstrates this measurement for the case of crossed dipole trap used in this work. The trapping frequencies are in the range of kHz when the atoms are first transferred from MOT to the dipole trap. The evaporative cooling carried out in this trap will be described in the next section.

2.5 Evaporative cooling

Laser cooling techniques are not enough to provide the required PSD for achieving BEC. After laser cooling, the optical density of the atomic cloud increases to the extent that the light scattered by an atom is absorbed by the neighboring atoms causing the sample to heat up [95]. Resonant light also leads to induced losses via inelastic collisions between the atomic ground and excited states [97]. Thus to achieve further increase in PSD, the atoms are transferred to an optical dipole trap for evaporative cooling. This

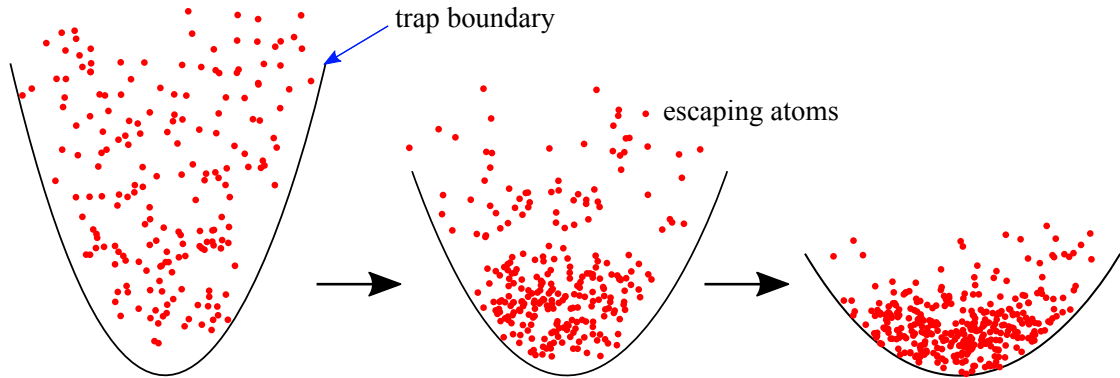


Figure 2.5: Evaporative cooling: The trapping potential is slowly lowered from left to right resulting in the ejection of atoms having energy higher than the confinement threshold. The rest of the atoms re-thermalize at a lower temperature via elastic collisions.

type of cooling can be modeled as several steps, where at each step the trap depth is lowered by a fraction $\gamma k_B T$, T being the temperature of the ensemble at that step. The fraction of atoms having energies above the threshold depth, escape from the trap. The remaining atoms then re-thermalize to a lower temperature via elastic collisions. These atoms also occupy a lower volume due to their reduced energy and hence results in a net increased density and thus increased rate of collisions. This phenomenon is called 'run-away evaporation' [88]. The collision rate in a harmonic trap is dictated by its trapping frequencies. The optical dipole trap typically possess $\omega_0 \sim \text{kHz}$ at the beginning of the evaporation ramp which is enough for efficient re-thermalization. As shown in Fig. 2.5, the power in the optical dipole beams and hence the trap depth is then lowered in an exponential fashion, till the atomic gas reaches quantum degeneracy. The temperature of the atomic gas is probed by turning off the trap and letting it undergo expansion and free-fall under gravity. The momentum distribution and hence the temperature of the gas can then be probed by acquiring an absorption image of the atomic gas. In Fig. 2.6, the last few steps of the evaporation stage are shown, where the signature of BEC is visible. In the next section we discuss the condensation process and the properties of the BEC state.

2.6 Condensation of a non-interacting Bose gas

It has been empirically established that all indistinguishable particles can be grouped into two categories based on the behaviour of their collective wavefunction under an exchange of any pair of particles [98]. These are called:

Bosons

$$\begin{aligned} P_{ij} |\psi(x_1 x_2 \cdots x_i x_{i+1} \cdots x_j \cdots x_N)\rangle &= |\psi(x_1 x_2 \cdots x_j x_{i+1} \cdots x_i \cdots x_N)\rangle \\ &= + |\psi(x_1 x_2 \cdots x_i x_{i+1} \cdots x_j \cdots x_N)\rangle \end{aligned} \quad (2.21)$$

Fermions

$$\begin{aligned} P_{ij} |\psi(x_1 x_2 \cdots x_i x_{i+1} \cdots x_j \cdots x_N)\rangle &= |\psi(x_1 x_2 \cdots x_j x_{i+1} \cdots x_i \cdots x_N)\rangle \\ &= - |\psi(x_1 x_2 \cdots x_i x_{i+1} \cdots x_j \cdots x_N)\rangle \end{aligned} \quad (2.22)$$

Where, $|\psi\rangle$ is the N -particle wavefunction, x_i is the index for a complete set of observables for the i^{th} particle and P_{ij} is the permutation operator that interchanges the i^{th} and the j^{th} particle. As it can be observed, the Bosonic wavefunction is symmetric under the action of P_{ij} , while the Fermionic wavefunction is anti-symmetric. No two Fermions can share the same set of observable indices x_i i.e. they can't be in the same quantum state, as such a wavefunction would be inherently symmetric. This is the celebrated Pauli exclusion principle which states that no two Fermions can have the same set of quantum numbers. This can also be elucidated by a two particle system, which can occupy states a or b . If ψ_1 and ψ_2 are the wavefunctions of the two particles, then their collective wavefunction is given by:

$$\psi_{\pm} = \frac{1}{\sqrt{2}} [\psi_1(a)\psi_2(b) \pm \psi_1(b)\psi_2(a)] \quad (2.23)$$

Here, the positive and the negative subscript of the collective wavefunction denotes the Bosonic and the Fermionic state. In the case of the Fermionic state, the collective wavefunction becomes 0 if the states a and b are the same, which is in agreement with the exclusion principle. On the other hand, Bosons do not have this limitation and any number of them can occupy the same quantum state. As the system temperature

is lowered below a certain critical point, this exchange degeneracy leads to a phase transition called as Bose-Einstein condensation where, the ground state of the system becomes macroscopically occupied. It is purely driven by the quantum statistics arising from the symmetric nature of the wavefunction as shown in Eq. 2.21. This transition was first predicted by Einstein in Ref. [99], following the work of Satyendra Nath Bose for the case of photon statistics in [100].

Experimental observation of BEC was thought to be difficult to observe as most particles form solids at low temperatures. Thus the ideal candidates for producing BECs were weakly interacting dilute gases. The experimental possibility of producing a BEC was first put forth by Hecht in 1960 [101] and later by William Stwalley and Lewis Nosano in 1976 [102] for the case of spin-aligned hydrogen atoms in high magnetic fields. The choice of hydrogen as the first species to attempt BEC on was natural due to its simplicity and the fact that it was theorized to stay gaseous even at low temperatures. Despite the simplicity, the attempts were hindered by two body collision losses due to long range interaction [88]. After two decades of laborious experiments, the hydrogen BEC was finally achieved in 1998 in T. Greytak's group at MIT [103]. Owing to the rapid development in cooling and confinement of dilute samples of alkali atoms using lasers and magnetic fields, the BEC was first achieved in this system in 1995. The observation was first reported by Eric Cornell and Carl Wieman with Rb atoms at NIST [104] and later by Wolfgang Ketterle with Na atoms at MIT [105]. They received the 2001 Nobel prize in physics for this achievement. Since this first observation, BEC has been achieved in many other atomic species: $^4\text{He}^*$ [106], ^7Li [107], ^{41}K [108], ^{40}Ca [109], ^{52}Cr [110], ^{84}Sr [111], ^{133}Cs [112], ^{164}Dy [113], ^{168}Er [114], ^{169}Tm [115], ^{174}Yb [116] and molecules: Li_2 [117]. The cold atom platform offers exquisite control over the quantum state of the BEC. It also allows precise measurement of the condensate wavefunction properties such as observation of matter-wave interference [118], collective common-mode oscillations [119] and super-fluid vortices [120]. In contrast to photons which interact weakly with each other, the atomic BEC possess tunable inter-particle interaction strength which has lead to observation of several exotic phenomenon such as solitons [121], super-radiant scattering [122], formation of quantum droplets [123],etc. The atomic spin degree of freedom also allows creation of

multi-component BECs [124]. We will now discuss the BEC transition in more detail for the case of harmonically trapped particles.

For 3D harmonic confinement, the energy states that the particles can occupy are of the form:

$$\epsilon_{n_x n_y n_z} = \left(n_x + \frac{1}{2}\right) \hbar\omega_x + \left(n_y + \frac{1}{2}\right) \hbar\omega_y + \left(n_z + \frac{1}{2}\right) \hbar\omega_z \quad (2.24)$$

Where, $\{n_x n_y n_z\}$ are the quantum numbers of an harmonic oscillator m with trapping frequencies of $\omega_x, \omega_y, \omega_z$ in the x, y and z direction respectively and m is the mass of the trapped particle. The single particle wavefunction corresponding to the ground state of the trap is given by a Gaussian:

$$\Psi_0 = \left(\frac{m\omega_0}{\pi\hbar}\right)^{3/4} \exp\left[-\frac{m}{2\hbar}(\omega_x x^2 + \omega_y y^2 + \omega_z z^2)\right] \quad (2.25)$$

Where, $\omega_0 = (\omega_x \omega_y \omega_z)^{1/3}$. The harmonic oscillator length introduces a natural length scale for the spatial extent of the wavefunction given by:

$$a_{HO} = \left(\frac{\hbar}{m\omega_0}\right)^{1/2} \quad (2.26)$$

For ^{87}Rb and $\omega_0 \sim 2\pi \times 100$ Hz, which are typical trapping frequencies for experiments, $a_{HO} \sim 1 \mu\text{m}$. As we will see later, the wavefunction extent is significantly larger than a_{HO} i.e. the corresponding momentum spread of the wavefunction is narrower for typical BECs due to inter-atomic interactions. Let us now consider a grand canonical ensemble of N particles [87]. At a temperature T , the average occupation of a state with energy ϵ is given by $f(\epsilon, T)$ and is called the Bose-Einstein distribution:

$$f(\epsilon, T) = \frac{1}{\exp[\beta(\epsilon - \mu)] - 1} \quad (2.27)$$

Here, $\beta = k_B T$, k_B is the Boltzmann constant and $\mu = \partial A / \partial N$ is the chemical potential, A being the Helmholtz free energy of the system. The above distribution function places a bound on the value of the chemical potential to be $\mu < \epsilon_0$ [125]. If $\mu > \epsilon_0$ then the occupation number for states with $\epsilon < \mu$ becomes negative, which

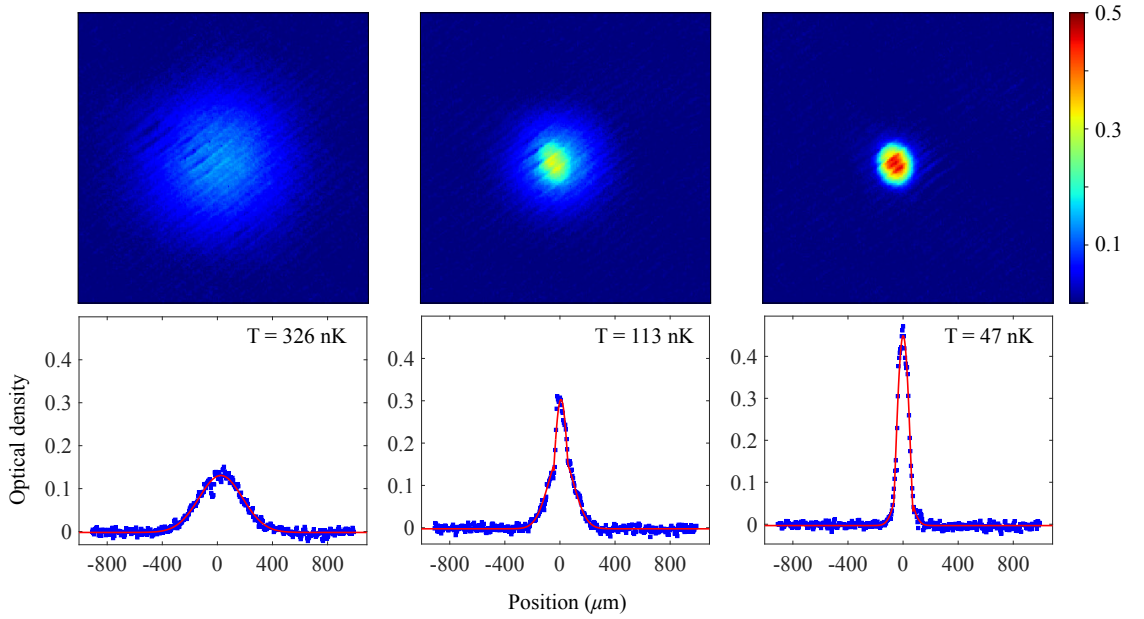


Figure 2.6: Bose-Einstein condensation of ^{87}Rb in an optical dipole trap: The figure shows time-of-flight images during the final evaporation steps in the ODT. The momentum distribution starts developing a deviation from the thermal distribution as the transition is approached. The center image clearly shows this bimodal (Gaussian+Thomas-Fermi) distribution, where the central component represents from the atoms in the condensed state. The final image shows an almost pure BEC state. The mentioned temperature is of the thermal component.

is un-physical. As $\mu \rightarrow \epsilon_0$ from smaller values, the occupation of the ground state starts becoming macroscopic, leading to the formation of the BEC state. We define the critical temperature T_c for a given number of particles N , at which the all the atoms occupy states other than the ground state when $\mu = \epsilon_0$:

$$N(T = T_c, \mu = \epsilon_0) = \int_0^\infty d\epsilon g(\epsilon) f(\epsilon) \quad (2.28)$$

Where, $g(\epsilon)$ is the density of states for the 3D harmonic oscillator and is given by:

$$g(\epsilon) = \frac{\epsilon^2}{2(\hbar\omega_0)^3} \quad (2.29)$$

Assuming that the ground state energy is small compared to the other terms in the integrand:

$$\begin{aligned} N &= \int_0^\infty d\epsilon \frac{g(\epsilon)}{e^{\epsilon/kT_c} - 1} = \frac{1}{2} \left(\frac{kT_c}{\hbar\omega_0} \right)^3 \int_0^\infty dz \frac{z^2}{e^z - 1} = \frac{1}{2} \left(\frac{kT_c}{\hbar\omega_0} \right)^3 \Gamma(3)\zeta(3) \\ &= \left(\frac{kT_c}{\hbar\omega_0} \right)^3 \zeta(3) \end{aligned} \quad (2.30)$$

Where, Γ and ζ is the gamma function and the Riemann-zeta function respectively. The critical temperature for the transition to occur is then calculated as:

$$k_B T_c = \hbar\omega_0 \left(\frac{N}{\zeta(3)} \right)^{1/3} \quad (2.31)$$

From this expression, it is seen that the transition temperature energy equivalent can be many times larger than the ground state of the harmonic oscillator. The temperature dependency of the condensate fraction N_0/N can be calculated by separating out the occupation of the ground state at any temperature $T < T_c$ and carrying out the integration similar to the one done above. This gives:

$$\frac{N_0}{N} = 1 - \left(\frac{T}{T_c} \right)^3 \quad (2.32)$$

For $N = 25000$ and $\omega_0 = 2\pi \times 130$ Hz (measurement shown in Fig. 2.4), the value of $T_c \approx 170$ nK using Eq. 2.31. This agrees with the transition as shown in Fig. 2.6, where a significant fraction is seen to be condensed at $T = 113$ nK. The non-interacting model lets us calculate the relevant thermodynamic parameters of the BEC transition. These properties do not differ significantly from the experimentally obtained values. Even so, the effect of inter-particle interactions is significant and needs to be included to explain effects such as suppression of peak density, increase in spatial extent of the wavefunction relative to the harmonic-oscillator ground state and other non-linear properties of the BEC state.

2.6.1 Effect of interactions on the ground state of a trapped BEC

We are ultimately interested in the density profile of the trapped condensate and its temporal evolution once the trapping potential has been turned off. We start by considering the time independent Gross-Pitaevskii (GP) equation [125]:

$$\left(-\frac{\hbar^2 \nabla^2}{2m} + V(r) + g|\Psi(r)|^2 \right) \Psi(r) = \mu \Psi(r) \quad (2.33)$$

Where, $V(r)$ is the harmonic confinement potential and $g = 4\pi\hbar^2 a/m$, a being the s -wave scattering length of the species in consideration. The form of two-body interaction energy $g|\Psi(r)|^2$ comes from approximating the collision events between atoms at these temperatures to be purely s -wave in origin. Even with such a simple form of the interactions, the above equation can satisfactorily explain many experimentally observed properties of the BEC. In the absence of this term i.e $g = 0$, the equation reduces into single particle time independent Schrödinger equation. From the normalization condition, the density of the condensate n is related to the order parameter by $\Psi = \sqrt{n}$. The kinetic energy term in the GP equation is of the order of $\sim \hbar^2/2mR^2$ for a cloud with spatial extent $\sim R$. In the case of strong interactions, the kinetic energy can be ignored and the spatial extent R is decided by the equilibrium condition between the harmonic potential and the interactions [126]. Thus, the cloud size is $R \sim a_{HO}(Na/a_{HO})^{1/5}$. This allows us to calculate the ratio of the kinetic energy to the other contributions to the total energy, which is $\sim (a_{HO}/Na)^{4/5}$. For ^{87}Rb , $N = 25000$ and $\omega_0 = 2\pi \times 130$ Hz, this ratio is ~ 0.02 . Thus, it is justifiable to ignore the kinetic energy term in the GP equation. This is called the Thomas-Fermi approximation and under this the GP equation reduces to:

$$|\psi(r)|^2 = n(r) = \frac{1}{g}(\mu - V(r)) \quad (2.34)$$

The normalization condition $\int n(r)dr = N$, gives a relation between μ and the number of particles N :

$$\mu = \frac{15^{2/5}}{2} \left(\frac{Na}{a_{HO}} \right)^{2/5} \hbar\omega_0 \quad (2.35)$$

Using the above relation yields the characteristic inverted parabolic form of the den-

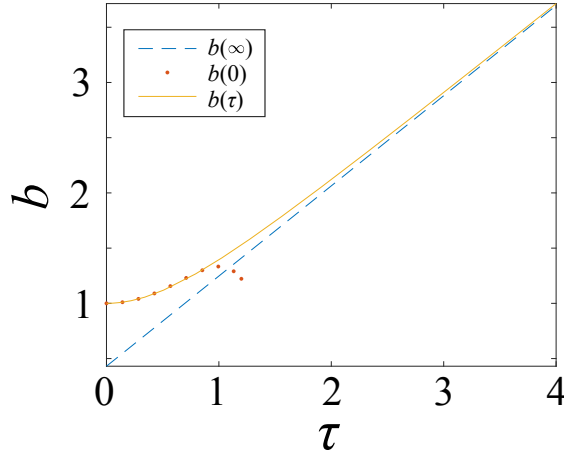


Figure 2.7: Temporal evolution of the expansion scale factor b_i : The plot shows the analytical solutions for $b(\tau)$ in different regimes along with the solution obtained from solving the second order differential equation directly in MATLAB ($\tau = \omega_0 t$). The solution is linear in the long term showing that the expansion velocity attains a saturation after sometime.

sity profile:

$$n(r) = n_0 \left(1 - \frac{x^2}{R_x^2} - \frac{y^2}{R_y^2} - \frac{z^2}{R_z^2} \right) \quad (2.36)$$

Where, $n_0 = \mu/g$ is the peak density of the BEC and R_i is called the Thomas-Fermi radius. It demarcates the extent of the BEC in the i^{th} dimension and is given by:

$$R_i = a_{HO} 15^{1/5} \left(\frac{Na}{a_{HO}} \right)^{1/5} \frac{\omega_0}{\omega_i} \quad (2.37)$$

The width of the momentum distribution of the atomic ensemble plays a vital role in the applications related to atom interferometry [127]. A narrow momentum width is often desired as it leads to more efficient beam splitting for the interferometry sequence. With several experiments now utilizing BEC as a source for performing atom interferometry it is worthwhile to investigate the momentum distribution of the BEC and its evolution. The momentum distribution is obtained by performing a Fourier transform on the spatial density profile as given by Eq. 2.36 [125]:

$$n(\tilde{p}) = N \frac{15R^3}{16\hbar^3} \left(\frac{J_2(\tilde{p})}{\tilde{p}^2} \right)^2 \quad (2.38)$$

Where, $R = (R_x R_y R_z)^{1/3}$, $\tilde{p} = \sqrt{p_x^2 R_x^2 + p_y^2 R_y^2 + p_z^2 R_z^2} / \hbar$ and J_2 is the second order

Bessel function of the first kind. As mentioned in Ref. [128], this distribution along any direction resembles a Gaussian with a standard deviation $\Delta p_x = \sqrt{21/8}\hbar/R_x$. This width is significantly narrower in comparison to that of the Gaussian ground state wave-function of the harmonic trap due to the inter-particle interactions. The ratio between the two is given by:

$$\frac{\Delta p_{TF}}{\Delta p_{Gaussian}} \approx 1.33 \left(\frac{a_{HO}}{Na} \right)^{1/5} \quad (2.39)$$

For $N = 25000$, $\omega_0 = 2\pi \times 130$ Hz and $a = 5.31$ nm (^{87}Rb) the ratio calculated using Eq. 2.39 comes out to be ~ 0.5 . Though the BEC momentum distribution is narrow in the trap, once it is released the momentum distribution is broadened. This occurs as the interaction energy gets converted into kinetic energy which leads to expansion of the density profile. This conversion of energy also causes the momentum width of the released BEC to broaden. This broadening of momentum distribution of BEC after being released from the trap, was measured with Bragg spectroscopy in Ref. [128]. As shown by Castin and Dum in Ref. [129], one can obtain analytical expressions for studying the expansion of the BEC. These expressions are derived under the assumption that the condensate maintains its initial parabolic form. Let $R_i(t)$ be the Thomas-Fermi radius of the BEC at time t :

$$R_i(t) = b_i(t)R_i(0) \quad (2.40)$$

Where, b_i is the dimensionless scale factor. As shown in Ref. [129], the time evolution of b_i is governed by three coupled differential equations:

$$\ddot{b}_i + \omega_i^2(t)b_i - \frac{\omega_i^2(0)}{b_i b_x b_y b_z} = 0 \quad (2.41)$$

The above equations are subject to constraints $b_i(0) = 1$ and $\dot{b}_i(0) = 0$. We are interested in the evolution of b_i when the trap is turned off i.e. when $\omega_i(t) = 0$. Assuming a spherically symmetric trap and scaling the time as $\tau = \omega t$ we get:

$$\frac{d^2 b}{d\tau^2} - \frac{1}{b^4} = 0 \quad (2.42)$$

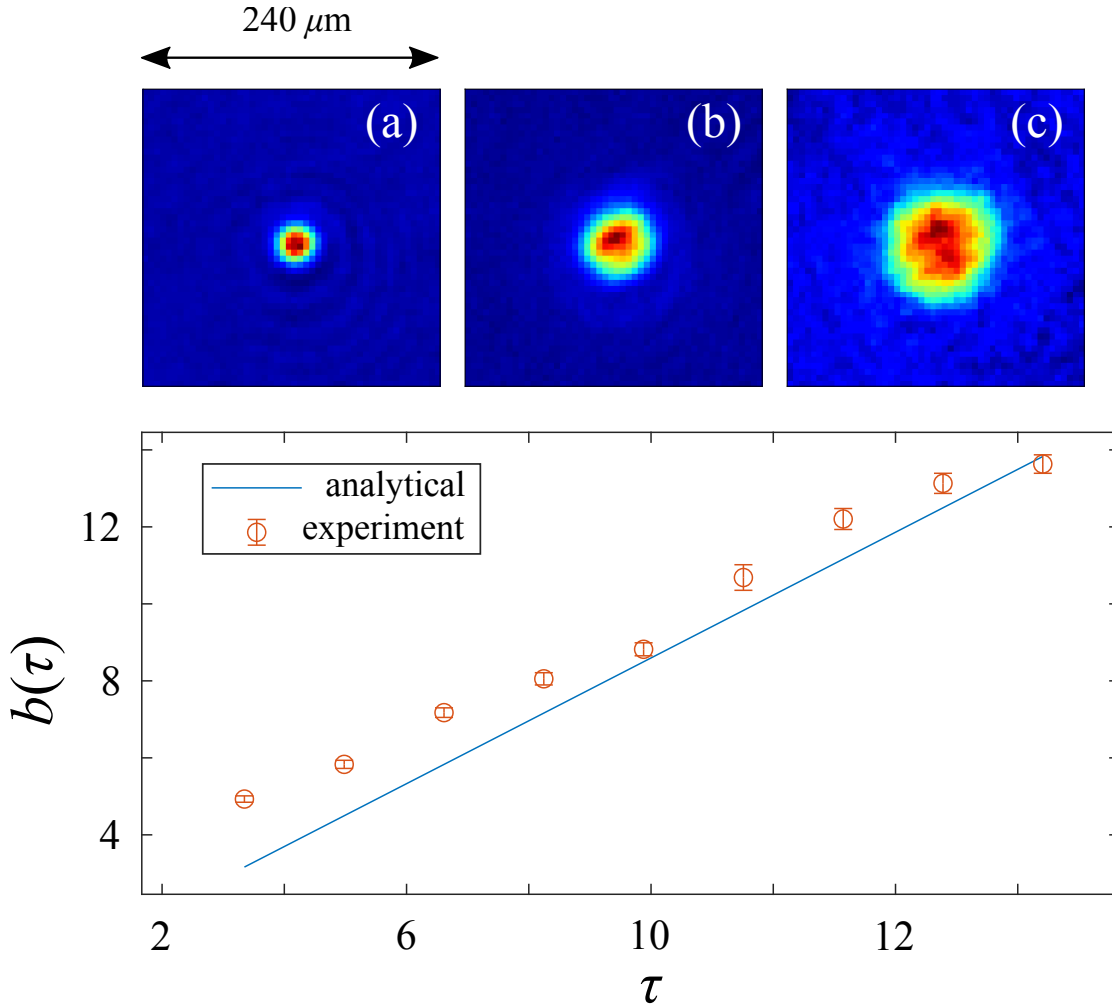


Figure 2.8: Expansion of BEC after release from the trap: (Top) Absorption images of the BEC for different time-of-flights. The BEC undergoes expansion as the interaction energy of the BEC is released as kinetic energy. **(Bottom)** The calculated expansion coefficient along with the experimentally observed one assuming a spherical trap with a trapping frequency of $\omega_0 = 2\pi \times 129$ Hz. τ is expressed in dimensionless units as $\tau = \omega_0 t$.

As shown in Ref. [130], one can get simplified expressions for $b(\tau)$ under certain limits:

$$b(\tau) \approx 1 + \frac{\tau^2}{2} - \frac{\tau^4}{6}, (\tau \rightarrow 0) \quad (2.43)$$

$$b(\tau) \approx \sqrt{\frac{2}{3}}\tau + \frac{\sqrt{\pi}\Gamma(2/3)}{\Gamma(1/6)}, (\tau \rightarrow \infty) \quad (2.44)$$

These solutions are plotted in Fig. 2.7 alongside the solution found by MATLAB's differential equation solver. It can be seen that after the initial accelerated expansion the

BEC attains a constant velocity profile.

2.6.2 Calculation of BEC momentum width

For $N = 25000$ and $\omega_0 = 2\pi \times 129$ Hz the initial Thomas-Fermi radius comes out to be $R_0 = 4.37 \mu\text{m}$. Fig. 2.8 plots the experimentally observed expansion coefficient with $R_0 = 4.37 \mu\text{m}$ as the initial value alongside the analytically calculated one using Eq. 2.44. The analytically determined expansion coefficient can be used to estimate the momentum width of the BEC at different instances of time. The velocity of the atoms at the edge of the atomic cloud i.e at the Thomas-Fermi radius is 0.0289 m/s or $0.246 \hbar K$ in terms of recoil momentum, a unit that will be relevant in later chapters ($K = 4\pi/\lambda$, $\lambda = 780$ nm). For comparison, the momentum width in the trap calculated from Eq. 2.38 is $0.023 \hbar K$. This value agrees with the one suggested by the δ -kicked rotor experiments presented in the later chapters.

Chapter 3

Matter-wave diffraction

Matter-wave diffraction is the matter-wave analog of optical diffraction. This chapter introduces the basic concepts behind diffraction of matter waves from an optical lattice and presents the relevant results for understanding it in different interaction regimes.

3.1 Coherent transfer of momentum from an optical potential

When a plane wave optical beam is incident on an optical grating, the periodic modulations of the grating refractive index are imprinted as phase modulations on the plane wave. This results in the k -vector of the initial plane wave to possess additional components with a magnitude decided by the grating period. This phenomenon is called as diffraction and is of immense importance in the field of optics and spectroscopy [131]. An analogous phenomenon occurs for matter-waves where the momentum wavefunction of particles undergoes diffraction and splits into several momentum components when incident on a grating. The matter-wave diffraction first predicted by Louis de Broglie in 1923 is a hallmark of the wave particle duality nature of quantum mechanics [4]. The predicted diffraction pattern was first observed for the case of electrons incident on a nickel crystal in the famous Davisson and Germer experiment in 1926 [5]. They were awarded the 1937 physics Nobel prize for this discovery, then – the newly emerging field of quantum mechanics.

For matter-wave diffraction to occur at an observable amplitude in the case of par-

ticles, their deBroglie wavelength ($\lambda_{dB} = p/\hbar$, p being the particle momentum) must be much larger than the period of the diffraction grating. The initial experiments which studied matter-wave diffraction used physical gratings and atomic beams with a high degree of collimation to increase the transverse coherence length [23]. In 1933, Pyotr Kaptisa and Paul Dirac proposed a novel mechanism for inducing coherent diffraction in electrons using an optical standing wave potential [132]. The coupling potential in this effect was due to the Lorentz force produced by the oscillating electromagnetic field. This prediction was very exciting because it involved the exact role reversal of matter and light and its demonstration would be a shining example of the wave-particle duality principle. The demonstration of KD effect for electrons had to wait until the invention of high power lasers as the spectral density of the light sources available in 1930s was not enough to appreciably observe the effect. It was finally observed by H. Batelaan's group at University of Nebraska-Lincoln in 2001 [133]. It was demonstrated much earlier (1986) for the case of a beam of neutral Na atoms by D. Pritchard's group at MIT [26]. This was possible due to that fact that the electric-dipole type coupling potential in this case was orders of magnitude higher.

We will now discuss the interaction between an optical lattice and neutral atoms in more detail.

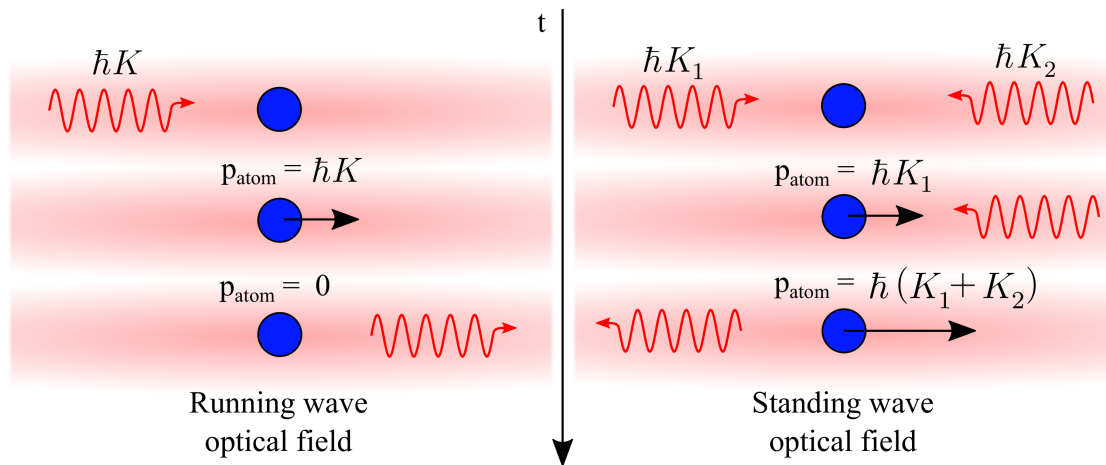


Figure 3.1: Momentum transfer using optical fields: (Left) No net momentum is imparted to the atom (blue sphere) via a coherent process in the case of a running wave. (Right) In this case a net momentum is imparted to the atom as it can absorb a photon from one field and emit it into the other through a stimulated emission process.

3.2 Two photon transitions

The requirement of a standing wave field as opposed to a running one for inducing momentum to an atom can be understood in the following manner: Fig. 3.1 (left), shows an atom in a running wave field. Assuming coherent excitation, a photon imparts a momentum of $\hbar K$ to the atom ($K = 2\pi/\lambda$, λ being the wavelength of the optical field). The excited atom now can only emit the photon in the same mode of the optical field and thus cannot gain a net momentum under this process. On the right, the two photons $\hbar K_1$ and $\hbar K_2$ belong the two propagating modes that constitute the standing wave. After absorbing a photon from one mode the atom can emit it in the other, gaining a net momentum of $\hbar(K_1 + K_2)$ in the process. To gain a quantitative understanding of the diffraction process, we now turn to the two-level model which was introduced in section 2.2.

We start by considering Eq. 2.7 and 2.8. For atoms that are initialized in the ground state $|b\rangle$, the excited state $|a\rangle$ can be adiabatically eliminated by using $\dot{C}_a = 0$ in the limit of low interrogation time and sufficiently large detuning [134]. Thus, the ground state evolution can be given as:

$$\dot{C}_b = i\frac{\delta}{2}C_b + i\frac{\Omega^2}{2\delta}C_b \quad (3.1)$$

Where, $\Omega = E_0|d_{ab}|/\hbar$ is the Rabi frequency of the system. In case of a standing wave formed by two counter-propagating laser beams of wavelength λ , the Rabi frequency will have a spatial variation of the form $\cos(2kx)$ ($k = 2\pi/\lambda$). Thus, Eq. 3.1, becomes:

$$\dot{C}_b = i\frac{\delta}{2}C_b + i\frac{\Omega^2}{2\delta}\cos^2(k\hat{x})C_b = i\frac{\delta}{2}C_b + i\frac{\Omega^2}{4\delta}(1 + \cos(2k\hat{x}))C_b \quad (3.2)$$

The dynamics so far only concerned the internal state manipulation of the atomic wavefunction. We are interested in the effect of this light-atom interaction on the motional state of the atom. For this matter, the components in Eq. 3.2 which are not a function of \hat{x} are of no concern as they will not affect the evolution of the momentum state occupation. Thus this “structureless” wavefunction of the atom obeys the Hamiltonian [67]:

$$H(\hat{x}, \hat{p}, t) = \frac{\hat{p}^2}{2m} - V_0 \cos(K\hat{x}) \quad (3.3)$$

Here, $V_0 = \hbar\Omega^2/4\delta$ is the lattice potential, $\hat{p} = -i\hbar\partial_x$ is the momentum operator, M is the mass of the atom under consideration and $K = 2k$ is the lattice wave-number. The Hamiltonian in Eq. 3.3 represents the underlying mechanism responsible for the coherent exchange of momentum between an atom and an electromagnetic field via the electric dipole interaction. Utilization of such an off-resonant optical lattice for imparting momentum to an initially stationary ensemble of atoms is typically carried out by temporally varying the potential V_0 in Eq. 3.3 in the form of a pulse. Such creation of a coherent multi-momentum state using an optical lattice pulse is the atomic Kapitza-Dirac effect. The Kapitza-Dirac diffraction is categorized in three regimes: Raman-Nath, Bragg and Stern-Gerlach [135]. In the first two regimes the spatial extent of the initial ensemble of atoms (Δx) is larger than the periodicity of the lattice ($2\pi/K$) and are the relevant ones for the case of cold atom sources.

We now discuss the Raman-Nath regime and the Bragg regime in detail.

3.3 The Raman-Nath regime

In the Raman-Nath regime the kinetic energy term in Eq. 3.3 is ignored. We now formally derive the equation for calculating the population in each diffracted order for a given set of parameters. We begin by observing that the $\cos(K\hat{x})$ operator in Eq. 3.3 can be expanded as:

$$H(\hat{x}, t) = -\frac{V_0}{2}(e^{iK\hat{x}} + e^{-iK\hat{x}}) \quad (3.4)$$

The operators $e^{\pm iK\hat{x}}$ act as translation operators in momentum space such that:

$$e^{\pm iK\hat{x}} |p\rangle = |p \pm \hbar K\rangle \quad (3.5)$$

Eq. 3.4 and 3.5 imply that interaction with the standing wave potential with a spatial period of $2\pi/K$ couples the momentum states differing by discrete units of $\hbar K$ [135]. Thus, the quantized nature of the momentum exchange emerges even though we treat the light field classically. The evolution of the coefficient of the ground state vector in the momentum space can be then calculated using the Schrödinger's equation:

$$i\hbar\dot{C}_b(p, t) = -\frac{V_0}{2}[C_b(p + \hbar K, t) + C_b(p - \hbar K, t)] \quad (3.6)$$

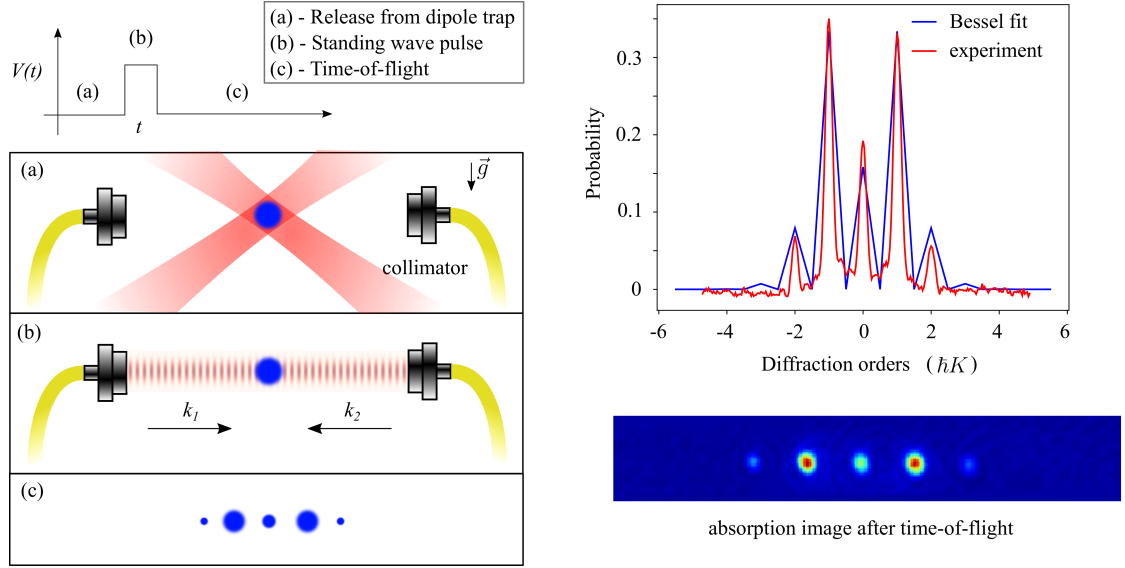


Figure 3.2: Raman-Nath regime of diffraction: (Left) (a) The BEC, prepared and confined in a crossed optical dipole trap is released after a certain wait time. (b) A standing wave is pulsed on for a variable time. This standing wave periodically modulates the condensate wavefunction, thus causing the BEC to diffract into different momentum states. (c) The BEC is then allowed to undergo free fall till the diffracted wavepackets can be resolved via absorption imaging. (Right) Experimentally observed absorption image of the diffraction process. The pulse period was kept as $t = 0.225 \omega_r^{-1} (9.5 \mu\text{s})$. The population in the diffracted orders agree with the Bessel distribution formula (Eq. 3.10) applicable in the Raman-Nath regime for a Bessel function argument of 1.7 as explained in the text below.

Now consider the initial momentum state of the atom to be a plane wave with momentum p . According to Eq. 3.6, the evolution in momentum state will only populate plane wave states which differ from p by $m\hbar K$, where m is an integer. Therefore, $C_g(p, t)$ can be decomposed in a basis set spanned by the plane wave momentum states $|p - m\hbar K\rangle$.

$$C_b(p, t) = \sum_m c_{b,m}(t) \delta(p - m\hbar K) \quad (3.7)$$

Substituting Eq. 3.7 in Eq. 3.6 and dropping the index b denoting the internal ground state, we get an infinite array of coupled differential equations:

$$i\hbar \dot{c}_m = -\frac{1}{2} V_0 [c_{m-1} + c_{m+1}] \quad (3.8)$$

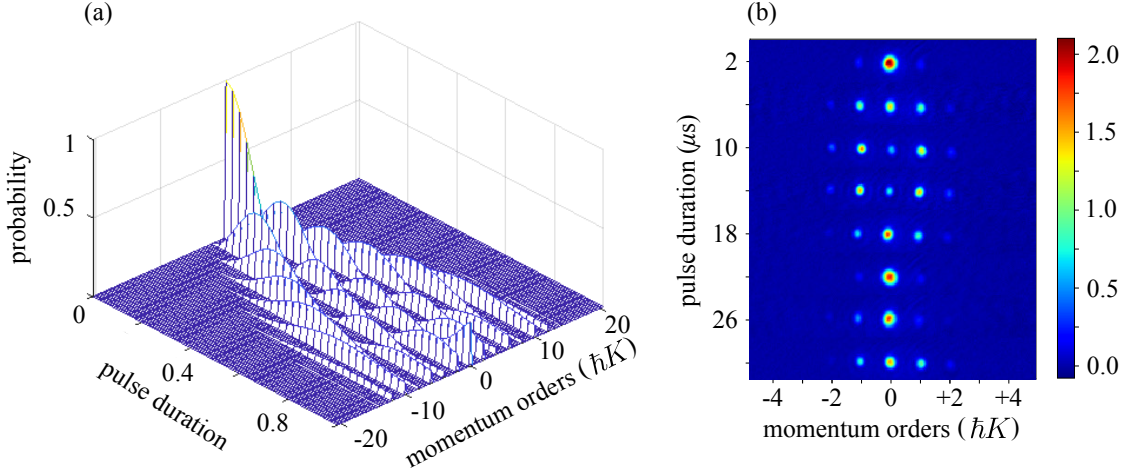


Figure 3.3: Beyond the Raman-Nath regime: (a) Simulated momentum distribution of momentum states for variable evolution time under optical lattice potential with $V_0 = 80 \hbar\omega_r$. The time axis is scaled w.r.t to the total pulse duration of $6 \mu s$. It can be seen that after $\sim 3 \mu s$, the population in diffracted orders beyond $m \sim \pm 10$ does not increase because of the breakdown of the Raman-Nath regime. (b) Experimentally observed momentum distribution of BEC subjected to a lattice potential for variable time. It can be seen that after sometime the initial zero momentum state is again populated. This ‘rephasing’ time roughly corresponds to a quarter of the oscillation period of the lattice harmonic potential.

As mentioned in Ref. [135], the solution to Eq. 3.8 is of the form:

$$c_m(t) = i^m J_m \left(\frac{V_0 t}{\hbar} \right) = i^m J_m \left(\frac{\Omega^2 t}{4\delta} \right) \quad (3.9)$$

Where, J_m is an m^{th} order Bessel function of the first kind. Thus, the probability $P_m(t)$ of occupying the momentum state $|m\hbar K\rangle$ after evolving under the interaction for time t is given by:

$$P_m(t) = J_m^2 \left(\frac{\Omega^2 t}{4\delta} \right) \quad (3.10)$$

This Bessel like intensity distribution is also observed in a light beam diffracted by acoustic wave in a crystal. This distribution was first explained by C. V. Raman and N. S. Nath in Ref. [136] and thus this regime for diffraction is named after them. For ^{87}Rb atoms and a lattice formed of $\lambda = 780 \text{ nm}$, the recoil frequency is $\omega_r \approx 2\pi \times 3.77 \text{ kHz}$. Fig. 3.2 shows the diffraction of the BEC under Raman-Nath regime. After being released from the trap, the optical lattice is applied for $t = 9.5 \mu s$ ($0.225 \omega_r^{-1}$) and

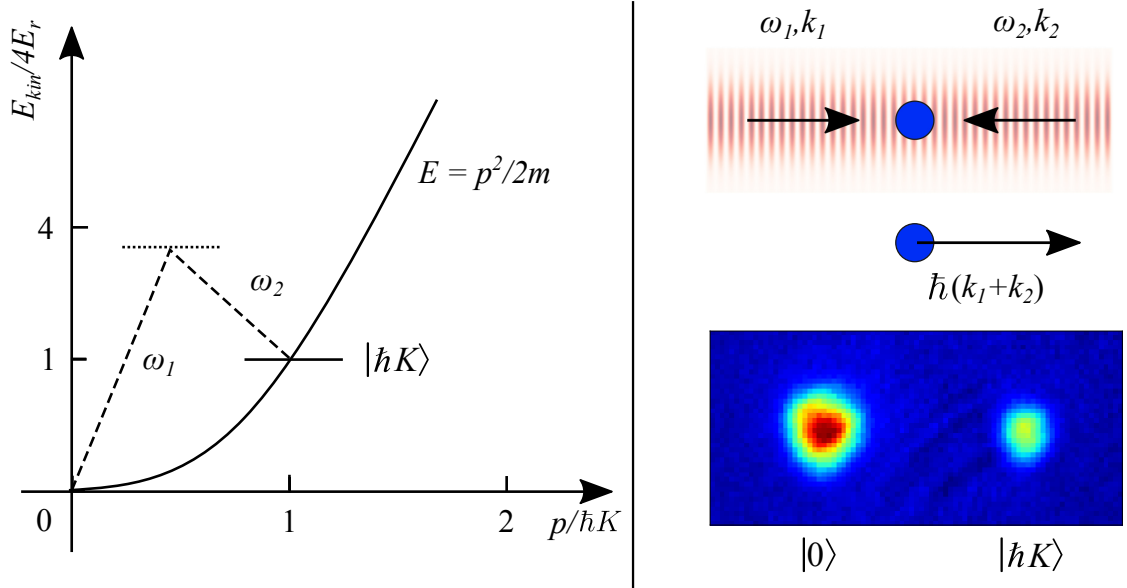


Figure 3.4: Bragg diffraction: (Left) Energy conservation condition for a two-photon transition connecting $|0\rangle \rightarrow |1\hbar K\rangle$ momentum states. The difference in frequencies of the two beams that make the running lattice should be $\omega_1 - \omega_2 = 4E_r/\hbar \approx 2\pi \times 15.2$ kHz for ^{87}Rb with 780 nm light. (Right) experimentally observed first order Bragg diffraction of the BEC.

agrees with the Bessel distribution for $V_0 t/\hbar = 1.7$. Thus, the optical lattice depth can be determined as $V_0 = 7.56 \hbar\omega_r$. If the pulse duration is increased further, population of the higher diffraction orders becomes significant enough to breakdown approximation of ignoring the kinetic energy term in Eq. 3.3. Fig. 3.3 (right) shows the evolution of with the same lattice potential ($V_0 = 7.56 \hbar\omega_r$) for longer time. As it can be seen in the figure, the momentum growth is arrested and reversed at around $22 \mu\text{s}$. This can be understood as the diffracted atoms oscillating in the potential formed by the optical lattice. The period of reversal is roughly equal to a quarter of the time period corresponding to the trapping frequency of the lattice potential [137]. The trapping frequency ω can be calculated using $V_0 = M\omega^2 X^2/2$, where $X = \lambda/4$ is the extent of the potential. For $V_0 = 7.56 \hbar\omega_r$ and $\lambda = 780$ nm, $\omega = 13.2$ kHz and the quarter oscillation period to be $\sim 19 \mu\text{s}$ which is in agreement with Fig. 3.3 (right).

Increasing the lattice potential depth increases the amount of diffraction orders which are initially populated, in turn decreasing duration of the Raman-Nath regime to be valid. This is seen in Fig. 3.3 (left) which plots the simulated evolution of the momentum state distribution under the Hamiltonian as given in Eq. 3.6. The simula-

tion parameters are the following: $V_0 = 80 \hbar\omega_r$, $t = 6 \mu s$ and the initial momentum state $C_g(p, t = 0) = \delta(0)$. As observed in the figure, the number of diffraction orders grow for a certain amount of evolution time after which the growth is arrested. From the analytical properties of Bessel function used in Eq. 3.9, the maximum number of the populated order (m_{max}) after an interaction time t should increase according to $m_{max} = 2V_0t/\hbar$ [135].

3.4 The Bragg regime

The regime where Raman-Nath condition is violated and the duration of the interaction is comparatively large is called the Bragg regime. Due to this large interaction duration, the energy-momentum conservation requirements are strict and only the momentum states which satisfy these are populated during evolution. The evolution of the ground state $C_b(x, t)$ without ignoring the kinetic energy term, is:

$$i\hbar \frac{\partial C_b}{\partial t} = -\frac{\hbar^2}{2M} \frac{\partial^2 C_b}{\partial x^2} - V_0 \cos(K\hat{x})C_b \quad (3.11)$$

Dropping the subscript denoting the ground state, we expand the wavefunction in a series of plane wave momentum states as shown before and obtain a series of an infinite set of coupled differential equations of the form:

$$i\hbar \dot{c}_m = m^2 \hbar\omega_r c_m - \frac{V_0}{2}(c_{m+1} + c_{m-1}) \quad (3.12)$$

The energy-momentum conservation for a n -photon transition is completely described by the condition [128]:

$$n\hbar\Delta\nu = \frac{q^2}{2m} + \hbar \frac{\vec{k}_i \cdot \vec{q}}{m} \quad (3.13)$$

Where, $q = n\hbar K$ is the total amount of momentum transfer to the atoms in the Bragg process and $n\delta\nu$ is the frequency detuning of between the two Bragg beams $N\Delta\nu = \omega_1 - \omega_2$. This reduced two level system then oscillates with a frequency of $V_0/2\hbar$ [135]. These oscillations are called as Pendellösung oscillations, derived from similar oscillations in neutron diffraction [138]. For ^{87}Rb and a lattice formed from 780 nm laser

beams, the frequency difference for carrying out first order diffraction can be calculated using Eq. 3.13. For an initially stationary BEC in the lab reference frame, $\vec{k}_i = 0$, the frequency difference turns out to be $\Delta\nu = \hbar K^2/2m = 2\pi \times 15.07$ kHz. Fig. 3.4 shows the first order diffraction with BEC.

3.5 Preparation and control of diffraction beams

This section briefly describes the optical arrangement for the production of the lattice beams. The light used to create this lattice is derived from the same laser as used for the primary cooling transition and hence is naturally ~ 6.8 GHz red detuned for the atoms which are in the $|F = 1, m_F = -1\rangle$ state. As shown in the Fig. 3.5, this laser beam is first reduced in size by lenses L1 and L2 and is then divided into two paths. Each of these beams is then passed through an acousto-optic modulator (AOM) from IntraAction Corp. (model no. ATM-801A2). The acoustic wave inside the AOM acts like a diffraction grating for the laser beam and the first order Bragg diffracted beam is steered into an optical fiber for delivery to atoms. The diffracted beam is frequency up or downshifted according to the order of diffraction:

$$E_d = E_0 e^{2\pi i[(f+n f_0)t + \Phi_d]} \quad (3.14)$$

Where, E_d is the diffracted beam, f_0 is the frequency of the acoustic wave running in the AOM crystal (80 MHz), $n = 0, \pm 1, \pm 2, \dots$ is the order of diffraction and Φ_d is the phase of the drive frequency. Thus if the two AOMs are driven by the RF sources which are phase locked to each other then the interference of the diffracted orders will create a standing wave whose phase can be arbitrarily controlled. The fast (compared to all other time scales in the experiment) rise time of the AOMs (~ 100 ns) also allows precise control on the pulse duration. The lattice depth V_0 is controlled by the amplitude of the RF drive. The beams are then coupled into polarization maintaining optical fibers and delivered to the atoms. The beam radius at the position of the atoms is ~ 350 μm . For realization of Bragg diffraction the frequency difference between the two AFGs is kept as required by the Bragg condition as given in Eq. 3.13.

The next section describes how the diffraction of cold atoms in the Raman-Nath

regime is used to emulate a Hamiltonian known as δ -kicked rotor.

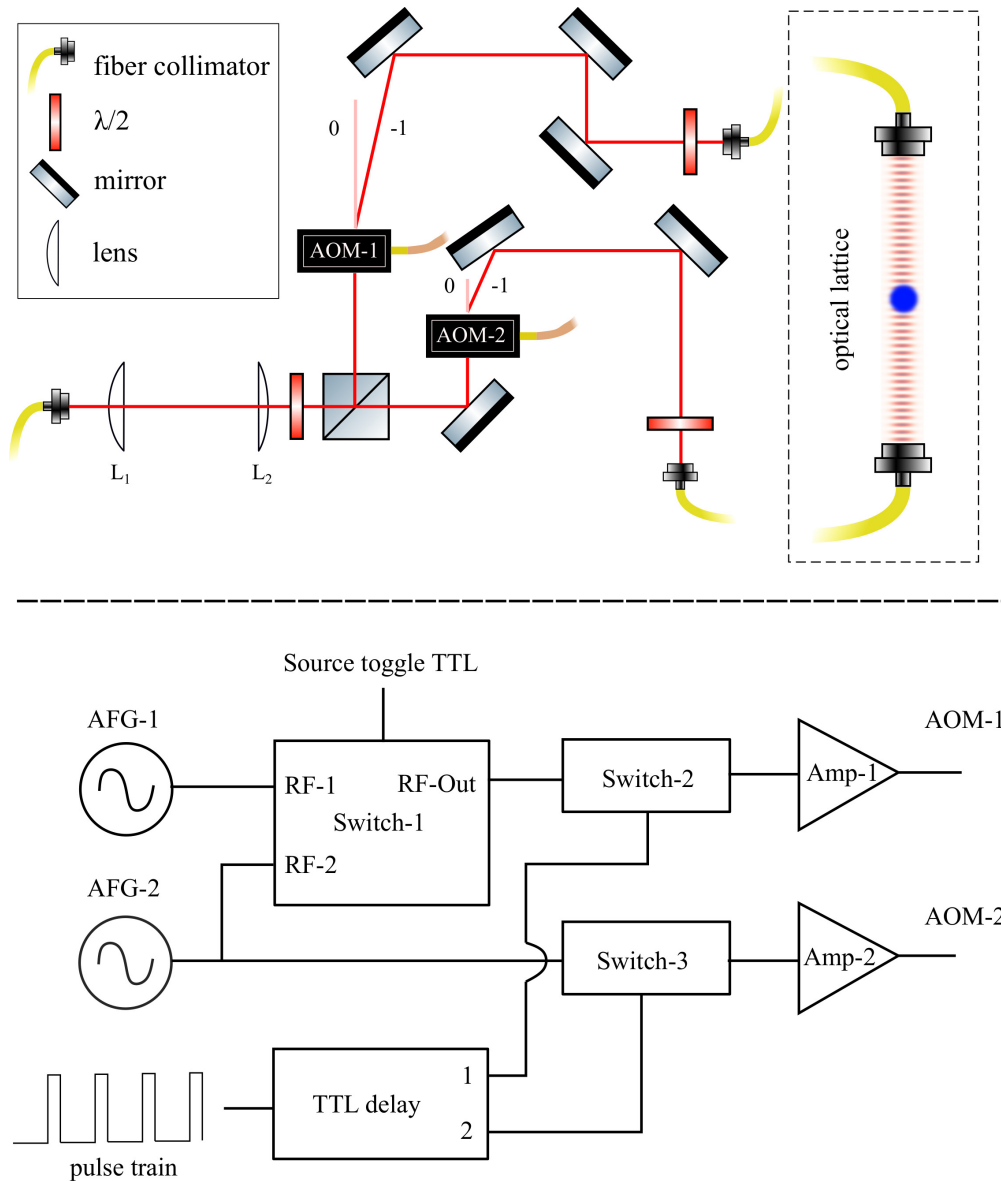


Figure 3.5: Lattice preparation: (Top) The optical lattice is formed from two counter propagating beams, each derived from a diffracted AOM order and delivered to the atoms via optical fibers. The AOMs are driven by two phase locked RF sources AFG-1 and AFG-2 (Tektronix, AFG 3101). Their relative phase can be set to any value. (Bottom) The signal from these AFGs is fed to the AOMs via RF amplifiers (Mini-Circuits, ZHL-1-2W). AOM-1 can be driven by either of the two function generators depending on the state of the source toggle TTL (Mini-Circuits, ZYSWA-2-50DR). Thus the phase of the optical lattice beam can be toggled between any two fixed values within ~ 10 s of ns. The amplitude of the optical lattice is pulsed via switches 2 and 3. The pulse train for these is passed through a delay generator (SRS, DG-535) to adjust for a time lag between the pulses caused due to different electronic paths.

Chapter 4

The δ -kicked rotor

This chapter introduces the implementation of the δ -kicked rotor Hamiltonian in a system consisting of a cold atom ensemble subjected to pulses of standing wave lattice potential. The quantum version of the kicked rotor shows resonant features which are absent in the classical version and can be potentially useful for precision measurements.

4.1 Classical δ -kicked rotor and chaos

The δ -kicked rotor has been a paradigmatic system for the study of chaos. It can be visualized as a particle attached to a mass-less rigid rod of length R and is allowed to rotate with one end of the rod fixed. The angular momentum of the particle is given by L and its moment of inertia is given by I . As shown in the figure, the system is then driven by application of an impulse force F having a shape of a δ with time period T , such that $F(t) = f \sum_{n=0}^{\infty} \delta(t - nT)$ [139]. The Hamiltonian of the classical kicked rotor is then given by:

$$H_{\delta KR} = \frac{L^2}{2I} - fR \cos(\theta) \sum_{n=0}^{\infty} \delta(t - nT) \quad (4.1)$$

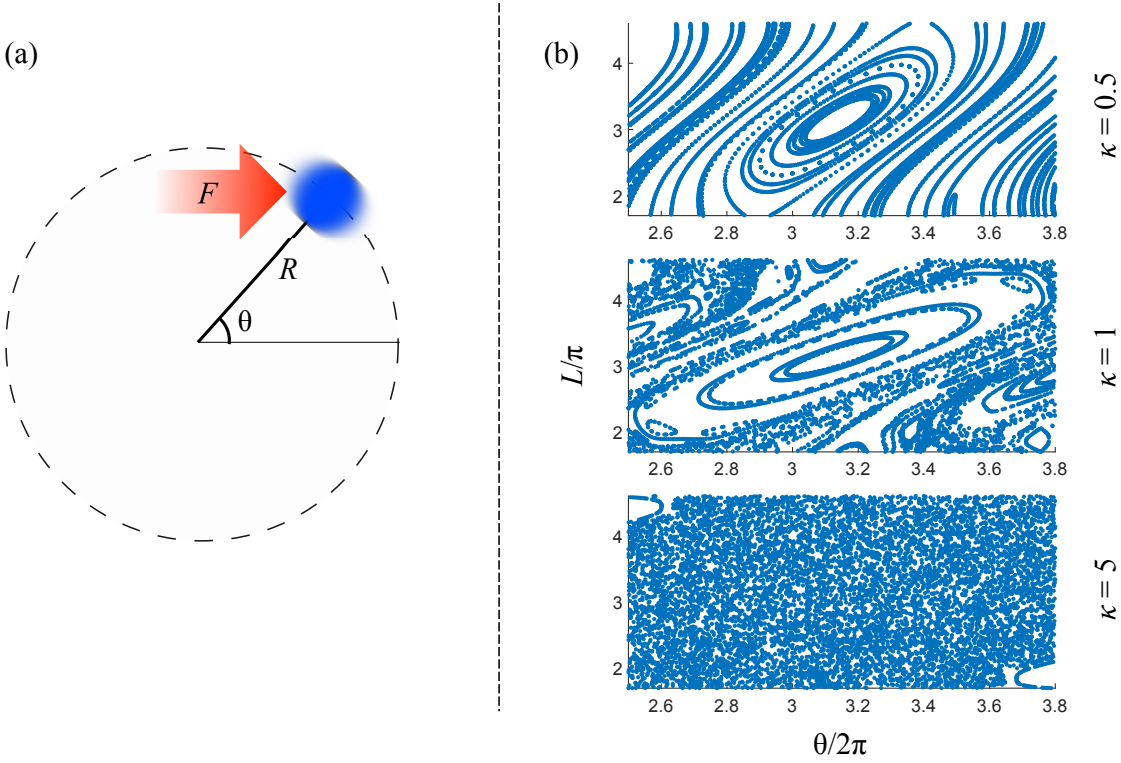


Figure 4.1: Classical chaos in δ -kicked rotor: (Left) Representative model of the δ -kicked rotor. A particle (blue sphere) which is free to rotate on a ring of radius R , is periodically ‘kicked’ with a force F . (Right) Poincaré sections of the δ -kicked rotor, governed by the standard map (Eq. 4.3). As the stochasticity parameter κ is increased beyond ~ 1 the system dynamics become chaotic.

Solving the Hamilton’s equation of motion for this, one can get iterative equations for the evolution of particle trajectory in the phase-space:

$$\theta_{n+1} = \theta_n + L'_{n+1} \quad (4.2)$$

$$L'_{n+1} = L'_n + \kappa \sin(\theta_n) \quad (4.3)$$

Where, $L' = LT/I$ is the dimensionless angular momentum parameter and $\kappa = fRT/I$ is called the stochasticity parameter. These set of equations are called the standard map or the Chirikov map and have been subjected to extensive studies to model chaos [140]. The phase-space behavior of the system is dictated by the single parameter κ . The critical parameter region where the transition from stability is predicted to occur is $0.971635 < \kappa_c < 63/64$. The transition to chaos can be clearly seen in the Poincaré

plots for different κ shown in Fig. 4.1.

4.2 Atom-optics quantum δ -kicked rotor (AOKR)

Chaos doesn't exist for a quantum system as its evolution is completely deterministic and governed by the Schrödinger's equation [141]. Even then, quantum analogues of systems whose classical phase space is chaotic, exhibit signatures of this chaos in their evolution [142]. The δ -kicked rotor is one such system where some aspects of the quantum behavior can be explained by studying the underlying chaotic or mixed phase space [143, 144]. The quantum δ -kicked rotor has been realized in several systems such as ionization of Rydberg atoms in microwave field [145], molecular rotors [146], etc. The most resourceful of these realizations has been the atom-optics δ -kicked rotor or AOKR [147]. Owing to the advancement in techniques for preparation of cold atomic ensembles and manipulation of their momentum state, the typical parameter space required for AOKR can be easily reached in a standard cold atom laboratory. We will now discuss this system in detail.

We recast the Hamiltonian of a two level atom subjected to a far-detuned standing-wave light potential ($K = 4\pi/\lambda$) as derived in Eq. 3.3 in the following form:

$$\hat{H} = \frac{\hat{p}^2}{2m} - \hbar\phi_d \cos(K\hat{x}) \sum_{n=0}^{\infty} \delta(t - nT) \quad (4.4)$$

Where, \hat{p} and \hat{x} are the momentum and position conjugate variables respectively. The optical field is applied as a series of pulses with time period T . The shape of the pulses is assumed to be a Dirac- δ function. The parameter $\phi_d = V_0 t_p / \hbar$ is called the kick strength, where t_p is the duration of the pulse. The form of this Hamiltonian is valid only under the Raman-Nath regime, where the kinetic energy evolution is ignored for the duration of the pulse. Since the momentum exchange happens in discrete units of $\hbar K$, there is a natural time scale to the kinetic energy phase evolution. At a pulse period of $T_T = 4\pi m / \hbar K^2$, the kinetic energy term becomes unity. This time is called the Talbot time and its significance will be discussed later. Using this, the Hamiltonian can

be expressed in a dimensionless form:

$$\hat{H}' = \pi \hat{p}^2 - \phi_d \cos(\hat{x}) \sum_{n=0}^{\infty} \delta(t - nl) \quad (4.5)$$

Where the scaling that is used is $p \rightarrow p/\hbar K$, $x \rightarrow xK$ and $t \rightarrow 2t/T_T$. $l = 2T/T_T$ denotes the scaled period. Since the pulses are applied with a definite period, the dynamics of the system is governed by the one period Floquet operator [139]. This operator is a time ordered product of the free evolution operator and the phase modulation or the kick operator:

$$\tilde{F} = \exp [i\pi l \hat{p}^2] \times \exp [-i\phi_d \cos(\hat{x})] \quad (4.6)$$

The quantum dynamics is influenced by two parameters, the kick strength ϕ_d and the scaled Plank's constant $\hbar_{eff} = 2\pi l$. The relation between the stochasticity parameter κ introduced earlier and these two parameters is $\kappa = \phi_d \hbar_{eff}$. Depending on the value of \hbar_{eff} the behavior of the quantum δ -kicked rotor can be divided into three categories: dynamical localization, resonance and anti-resonance. We will discuss these regimes below.

4.3 Dynamical localization

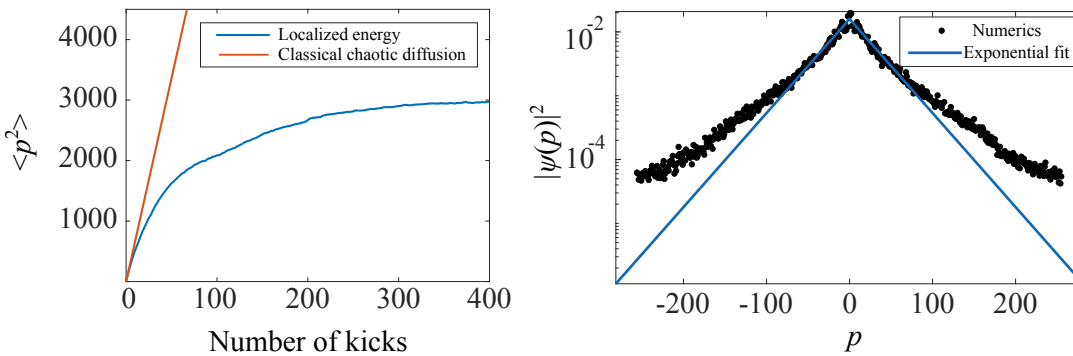


Figure 4.2: Localization in quantum δ -kicked rotor: (Left) The average energy of the system as a function of the number of kicks. The energy growth is arrested beyond a certain ‘quantum break time’. The simulation parameters are $\kappa = 11.6$ and $\hbar_{eff} = 1$. (Right) The momentum distribution in this ‘localized’ regime assumes a double-exponential profile.

In the classical picture, the energy evolution can be considered as a random walk in

phase space and the energy growth of the system is diffusive in nature with the diffusion constant being a quadratic function of the kick strength, such that $\langle p^2 \rangle = \kappa^2 l / 2$ [140]. In contrast to this, when \hbar_{eff} is an irrational multiple of π , the corresponding quantum system follows this behavior until a certain ‘Heisenberg time’ or ‘quantum break time’ after which the dynamics effectively freezes. Upon further application of pulses the energy does not grow and the system is said to be ‘localized’. This can be seen in Fig. 4.2, where the simulated energy plot for clearly shows saturation in comparison to the classical energy growth. The plot on the right in the same figure shows the simulated momentum distribution after 400 pulses assuming a double exponential ‘localized’ profile ($e^{-|p|/c}$). The experimental demonstration of quantum localization in AOKR was first done by M. Raizen in 1995 [148]. This demonstration rejuvenated the experimental efforts towards quantum chaos studies using AOKR. The phenomenon of quantum localization is of a broader interest as it has been exactly mapped to the Anderson localization problem in condensed matter physics [149, 150]. When confined in a disordered potential, the electron wavefunction in position space has the same functional form ($e^{-|x|/c}$) as the localized momentum profile in AOKR. This is behavior of electrons is known as the Anderson localization. Apart from the generic dynamical localization which occurs at any period satisfying the irrationality condition of the effective Plank’s constant, the δ -kicked rotor also exhibits resonant behavior at integer multiples of Talbot time. The next sections introduces these ‘quantum resonances’.

4.4 Quantum resonances

When $\hbar_{eff} = 2\pi(q + 1)$ or $4\pi q$ ($q = \text{integer}$), the dynamics of the system shows a dramatic deviation from the generic localized behavior. These can be understood in the following manner. Consider a plane wave state with zero momentum denoted as $|0\rangle$. The resulting wavefunction immediately after the application of the first standing wave δ -pulse can be given by [151]:

$$|\psi(t = 0^+)\rangle = e^{i\phi_d \cos(\hat{x})} |0\rangle = \sum_{n=-\infty}^{\infty} i^n J_n(\phi_d) |n\rangle \quad (4.7)$$

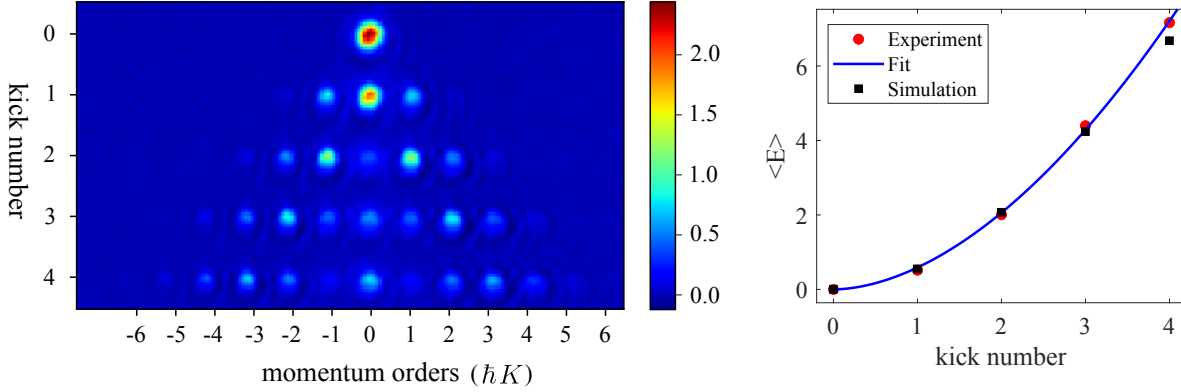


Figure 4.3: Quantum resonance: (Left) Time-of-flight images after subjecting the BEC to δ -pulses of standing wave at resonant period ($T = 66.34 \mu\text{s}$ for ^{87}Rb) with kick strength $\phi_d = 0.8$. The momentum orders get progressively populated as number of kicks increase. (Right) Energy growth corresponding to the images shown on the left along with a power law fit ($E = AN^B$). The fit parameters are $A = 0.59 \pm 0.11$, $B = 1.81 \pm 0.15$, implying that the energy grows quadratically with each kick. The red circles correspond to the experimental data. The black squares correspond to the numerical simulations.

For a pulse period of l , the wavefunction just before the second pulse is:

$$|\psi(t = l^-)\rangle = \sum_{n=-\infty}^{\infty} i^n e^{-i\pi l n^2} J_n(\phi_d) |n\rangle \quad (4.8)$$

Where, each basis state ($\langle x|n\rangle = e^{-inx}$) is tagged with its corresponding free evolution term. If the pulse period l is an even number, then this free propagation phase turns out to be unity and the wavefunction resembles the initial one.

$$|\psi(t = l^-)\rangle = \sum_{n=-\infty}^{\infty} i^n J_n(\phi_d) |n\rangle = |\psi(t = 0^+)\rangle \quad (4.9)$$

This revival of the wavefunction after a period of free propagation is called the matter-wave Talbot effect. This is analogous to the optical Talbot effect, where similar revival of the interference pattern occurs in the near field of a diffraction grating [56]. If a second pulse of same kick strength is applied then it doubles the phase modulation of the previous pulse and results in even more states being populated.

$$|\psi(t = l^+)\rangle = e^{i2\phi_d \cos(\hat{x})} |0\rangle \quad (4.10)$$

This effect is called as Talbot resonance and leads to a quadratic increase in the total energy of the system with the number of kicks [152]. This can be seen in Fig. 4.3.

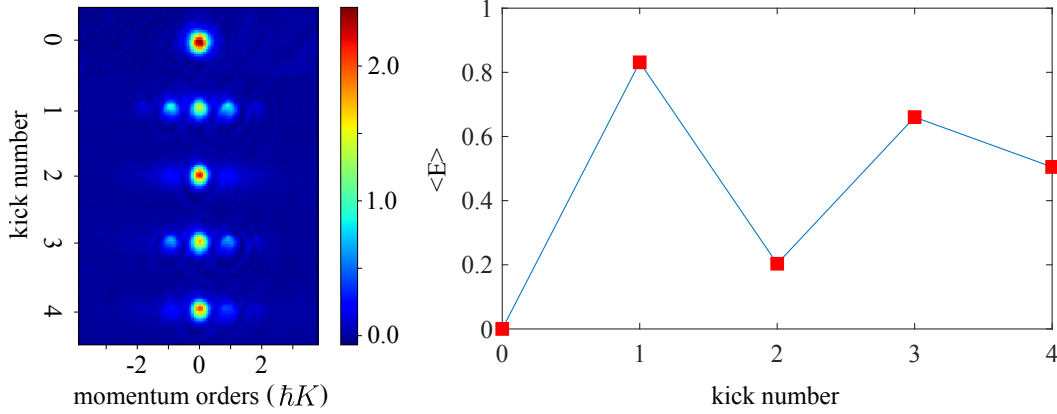


Figure 4.4: Quantum anti-resonance: (Left) Time-of-flight images after subjecting the BEC to δ -pulses of standing wave ($\phi_d = 0.8$) at anti-resonant period ($T = 33.15 \mu\text{s}$ for ^{87}Rb). Each kick cancels out the phase modulation produced by the previous one. (Right) Energy evolution corresponding to the images shown on the left. The contrast in anti-resonant behavior is not perfect due to a finite momentum width of the BEC.

For pulse periods which are odd, the free propagation phase that is gathered for each basis state in this case depends on its momentum. The resulting summation can then be reduced to a form where the ϕ_d gets a negative sign:

$$|\psi(t = l^-)\rangle = e^{-i\phi_d \cos(\hat{x})} |0\rangle \quad (4.11)$$

Thus after the application of the next pulse keeping the lattice phase unchanged, the modulation of the previous pulse is exactly canceled out. This leads to revival of the initial state:

$$|\psi(t = l^+)\rangle = e^{i\phi_d \cos(\hat{x})} e^{-i\phi_d \cos(\hat{x})} |0\rangle = |0\rangle \quad (4.12)$$

This revival can be seen in Fig. 4.4. The revival is not perfect because of the finite momentum spread of the BEC [153]. This can be understood by looking at the Floquet operator for a wave-packet $|\beta\rangle$ which is not an integral multiple of $\hbar k$. In this case, the free propagation phase at resonance will be $e^{-2\pi i \beta^2}$, which is not unity. Thus, for an initial state ensemble with a distribution $\Delta\beta$, the resonance and anti-resonance dynamics will deviate from ideal behavior with the extent of deviation depending on the

narrowness of the spread [152].

The fidelity of the reversal process is sensitive to the pulse period and the pulse sequence can be considered as an atom interferometer where any deviation from the anti-resonance condition leads to drop in reversal fidelity. This is the general idea behind the pulse sequence for measurement of Talbot time which will be introduced in the next chapter.

Chapter 5

Measurement of Talbot time using AOKR

The results presented in this chapter have been published in:

“Effects of finite momentum width on the reversal dynamics in a BEC based atom optics δ -kicked rotor”

Jay Mangaonkar, Chetan Vishwakarma, S Sagar Maurya, Sumit Sarkar, Jamie L. MacLennan, Pranab Dutta and Umakant D. Rapol

Journal of Physics B: Atomic, Molecular and Optical Physics, 53, 235502 (2020)

The Talbot time in AOKR is essentially a measurement of the recoil frequency of the atom. As shown in Fig. 1.3, together with other well known constants, this is used to determine the fine structure constant α . This chapter introduces a Talbot time measurement scheme in AOKR that uses a fidelity based approach. The AOKR pulse scheme is demonstrated which maximizes the initial state fidelity when the pulse period is set to an integer multiple of Talbot time. We study the effect of initial state width on the performance of this pulse sequence.

5.1 Measurement scheme

As discussed in the previous chapter, apart from the generic localization behavior in AOKR, for certain pulse periods the system shows resonant behavior. In the resonance

case, the energy imparted to the system after N kicks is sensitive to the pulse period and peaks at the Talbot time ($l = 2q$, where q is an integer). It has been shown that, due to the quantum interference between the participating basis states, the width of this measurement is not limited by the Fourier relation ($\Delta T \propto N^{-1}$, N being total number of pulses or the total interrogation time). In fact it has been shown that the width of the resonance in energy scales as N^{-2} [73].

In Ref. [154], it was shown that the sensitivity to deviation from the resonant pulse period of the final wavefunction obtained after application of a pulse series, did not fully reflect in the momentum space measurement. Thus the energy measurement based approach used in Ref. [73] did not fully exploit the changes in the relative phases between the basis states participating in the interference. A better technique was proposed in Ref. [154], where the final pulse returned the evolved state back to the initial state at exact resonance. The overlap of the final state to the initial one (fidelity), is then maximum for resonance and drops for any deviations from resonance. The width of the resonance in this case was theoretically predicted to scale as $\Delta T \propto N^{-3}$. We discuss this pulse sequence in the next section.

5.1.1 Pulse scheme-1

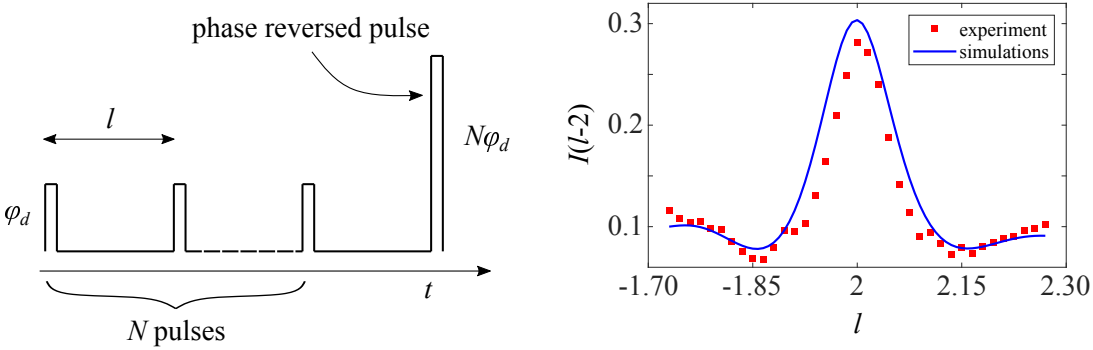


Figure 5.1: Pulse scheme-1: (Left) Schematic of the pulse scheme. After the first N pulses, the phase of the optical lattice is shifted by π radians and the lattice power is ramped up such that the phase modulation depth is $N\phi_d$. At resonance this last pulse cancels out the phase modulation of the previous pulses and revives the initial state. **(Right)** Experimental implementation of the pulse sequence for $N = 4$, $\phi_d = 0.8$. As it can be seen the fidelity at resonance is less than unity due to the momentum width of the BEC. Simulated values accommodate this momentum spread in initial ensemble ($\Delta p = 0.035$).

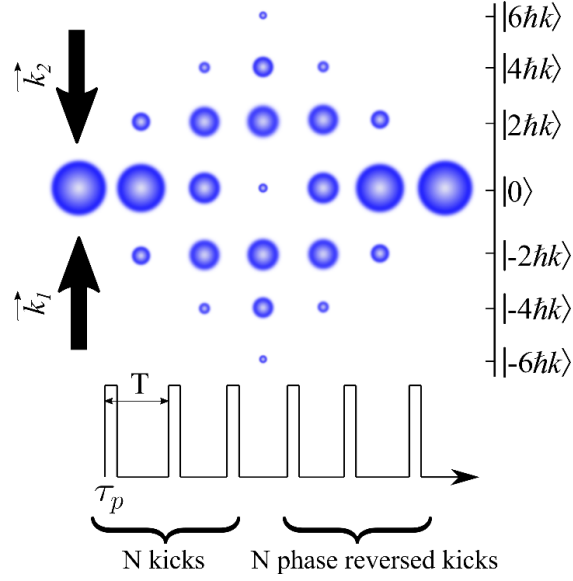


Figure 5.2: Pulse scheme-2: The evolution of the BEC wavefunction is shown in momentum space at the resonance condition ($T = T_T$). The spheres represent of the relative population present in different momentum states after each pulse in the sequence shown at the bottom. The number in n^{th} order is $\propto |\langle 2n\hbar k | \psi(p) \rangle|^2$. \vec{k}_1 and \vec{k}_2 denote the wave vectors of the two laser beams forming the standing wave that is pulsed for a duration of τ_p , according to the shown sequence.

As shown in Fig. 5.1(left), the pulse sequence mentioned in Ref. [154] used N kicks at a constant kick strength ϕ_d and a final kick with N times the kick strength but having a negative sign. The sign of the kick strength is inverted by shifting the phase the standing wave by π radians. The Hamiltonian for the pulse sequence for N is then:

$$\hat{H}' = -\pi\hat{p}^2 + \phi_d \cos(\hat{x}) \sum_{n=0}^{N-1} \delta(t - nl) - N\phi_d \cos(\hat{x})\delta(t - Nl) \quad (5.1)$$

As shown in Ref. [154], for a plane wave initial state ($\Delta\beta = 0$) and in the limit of large N , the expression for fidelity I for a small deviation $\epsilon = (l - 2)$ from the resonance condition is

$$I(\epsilon) = J_0^2 \left(\frac{\pi N^3 \phi_d^2 \epsilon}{6} \right) \quad (5.2)$$

Where, J_0 is the Bessel function of the first kind. From Eq. 5.2, it can be seen that the width of the resonance decreases as $\propto N^{-3} \phi_d^{-2}$. This scaling in N was demonstrated in Ref. [84] and is very favorable for measurement of the Talbot time. Fig. 5.1(right) shows

the implementation of this sequence for $N = 4$, $\phi_d = 0.8$. We used this measurement-set to benchmark the phase inversion sequence with our setup. One of the limitations of this scheme is that the power in the last pulse needs to be dynamically ramped up to a higher value at the end of the sequence. To circumvent this, another variant of the pulse sequence was proposed in Ref. [82]. This pulse sequence keeps the kick strength uniform throughout but utilizes twice the amount of kicks in comparison to the previous one.

5.1.2 Pulse scheme-2

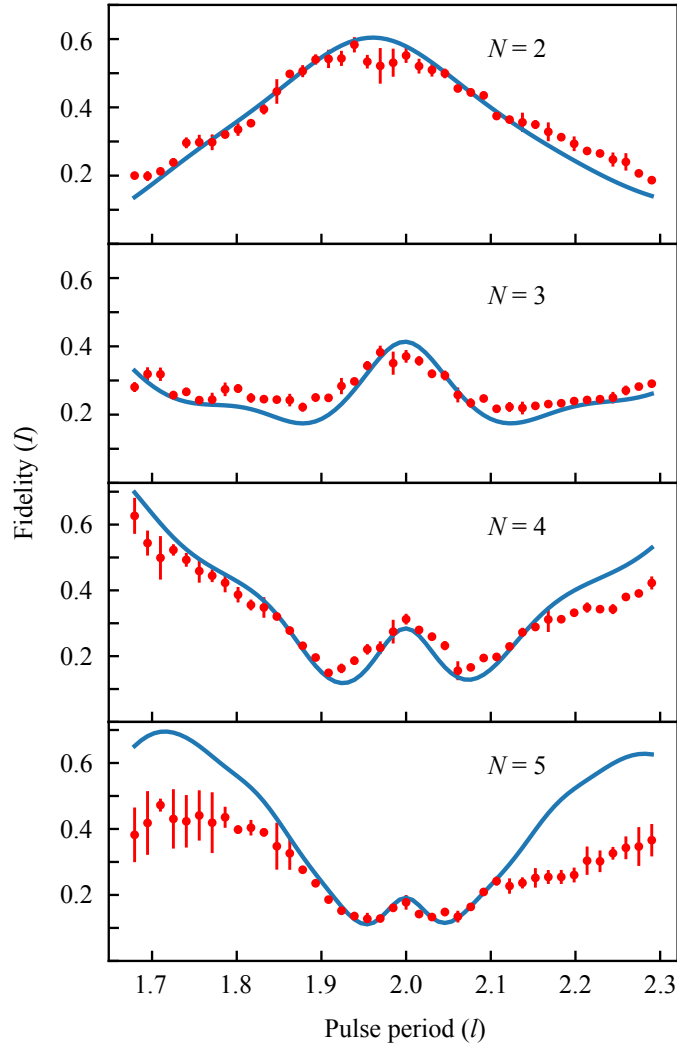


Figure 5.3: Variation of fidelity $I(l)$: Fidelity (I) as a function of scaled pulse period (l) for different number of kicks N at a constant kick strength $\phi_d = 0.8$. The red dots are the experimental data and the blue solid lines are the numerical simulations. The error bars represent \pm one standard deviation over 5 data points. $\Delta\beta$ is the only free parameter used to match the experimental values at different number of kicks. The values for $\Delta\beta$ used are 0.023 for $N=2$ and 0.017 for $N = 3, 4, 5$ respectively. Data for $N = 1$ is not shown here as fidelity doesn't undergo significant change at this scale.

As seen in Fig. 5.2, the pulse sequence proposed in Ref. [82] is symmetric in time. The phase of the lattice is shifted by π radians after the first N pulses are delivered. At resonant pulse period ($l = 2$), each subsequent pulse after this phase shift, reverses the

dynamics of the previous pulses and the initial state is retrieved. The Hamiltonian for this pulse scheme is:

$$\hat{H}' = -\pi\hat{p}^2 + \phi_d \cos(\hat{x}) \left(\sum_{n=0}^{N-1} \delta(t - nl) - \sum_{n=N}^{2N-1} \delta(t - nl) \right) \quad (5.3)$$

We have seen previously that the resonant dynamics is affected by the momentum width of the initial ensemble $\Delta\beta$ affects the state evolution of the system. The dependency of fidelity I on deviation from the zero-momentum plane wave state can be calculated by incorporating the quasi-momentum β , ($-1/2 \leq \beta < 1/2$) into the Floquet operator:

$$\tilde{F}(\beta) = \exp \left[-i\pi l (\hat{k} + \hat{\beta})^2 \right] \times \exp [i\phi_d \cos(\hat{x})] \quad (5.4)$$

Considering the initial state as $|\beta\rangle$, the final state after $2N$ pulses then becomes

$$|\psi(t = 2N)\rangle = \tilde{F}_\pi^N(\beta) \tilde{F}_0^N(\beta) |\beta\rangle \quad (5.5)$$

Where, $\tilde{F}_0(\beta)$ is the Floquet operator for each of the first N kicks and $\tilde{F}_\pi(\beta)$ is that for the subsequent phase-shifted kicks. The reversal fidelity is given as:

$$I(l, \beta) = |\langle \beta | \tilde{F}_\pi^N(\beta) \tilde{F}_0^N(\beta) | \beta \rangle|^2 = \left| \sum_{n=-\infty}^{\infty} d_n^* e_n \right|^2 \quad (5.6)$$

Where $e_n = \langle n\hbar K | \tilde{F}_0^N | \beta \rangle$ and $d_n^* = \langle n\hbar K | \tilde{F}_\pi^N | \beta \rangle^*$. An analytical expression can be derived for $I(l, \beta)$ to the first order in l and β , as shown in Ref. [82]. We briefly present the relevant results here. Recasting e_n and d_n^* in polar form and using a first-order Taylor expansion in the variable $\epsilon = (l - 2)$, one arrives at their analytical forms:

$$e_n = J_n(N\phi_d) \exp\{i\pi[L_+(l - 2) - 2\beta n(N + 1) - n/2]\} \quad (5.7)$$

$$d_n^* = J_n(N\phi_d) \exp\{i\pi[L_-(l - 2) + 2\beta n(N - 1) + n/2]\} \quad (5.8)$$

$$L_{\pm} = \frac{1}{6} \left(N - \frac{1}{N} \right) n - \frac{1}{6} \phi_d (N^2 - 1) \frac{J_{n-1}(N\phi_d)}{J_n(N\phi_d)} - \left(\frac{1}{3} N \pm \frac{1}{2} + \frac{1}{6} \frac{1}{N} \right) n^2 \quad (5.9)$$

Where J_n is an n^{th} order Bessel function of the first kind. The sum in Eq. 5.6 can be appropriately truncated to compute this value, as only finite number of orders are populated significantly during a pulse sequence. In the asymptotic limit of large N and for $|\beta = 0\rangle$, a simple expression can be obtained by keeping only the dominant terms $\propto n^2 N$ in Eq. 5.9. As shown in Ref. [82], under these approximations Eq. 5.6 can be reduced to:

$$I(l, \beta = 0) \approx J_0^2 \left(\frac{\pi}{3} N^3 \phi_d^2 (l - 2) \right) \quad (5.10)$$

Thus, the scaling for this sequence is $\propto N^{-3}$ which is the same as that for pulse sequence-1. It was observed that the experimentally determined scaling deviates from the first order prediction made in Eq. 5.10 and never reaches the value of -3 which is predicted in the limit of large N . To understand the reason behind this, we look at the regimes in which the approximations made in deriving Eq. 5.10 fail to be valid. The first assumption is that the initial state is a plane wave with zero momentum, which is not true even for very narrow momentum ensembles like the BEC. The typical value of the momentum width of BECs varies around $\Delta\beta \sim 0.1 - 0.01$. Thus to determine the scaling for experimentally realistic ensembles we need to calculate the ensemble fidelity. Approximating the ensemble by a Gaussian $G(\beta)$ with a standard deviation of $\Delta\beta$, the fidelity is thus:

$$I'(l) = \int_{-0.5}^{0.5} G(\beta) I(l, \beta) d\beta \quad (5.11)$$

The fidelity width S predicted by Eq. 5.6 under the plane wave approximation of $\beta = 0$, is in agreement with Eq. 5.11 when the distribution $G(\beta)$ is narrower than the momentum width of the pulse sequence, i.e the width of $I(l = 2, \beta)$. In Ref. [82], Daszuta and Andersen derive an expression for the fidelity $I(l = 2, \beta)$:

$$I(l = 2, \beta) \simeq J_0^2(4\pi N^2 \phi_d \beta) \quad (5.12)$$

The width of $I(l = 2, \beta)$ represents the range of values of β which well-approximate the zero-momentum plane-wave state. The width of $I(l = 2, \beta)$ decreases inversely proportionally to N^2 . The deviation of $I'(l)$ from the analytically expected scaling due to the effect of finite β distribution has been reported in the simulation work done in Ref. [82]. We now proceed to validate this model with experimental data.

5.2 Experimental results

The pulse sequence as shown in Fig. 5.2 was applied $\sim 100 \mu\text{s}$ after the hybrid dipole trap was turned off. The pulse duration and kick strength was $\tau_p = 550 \text{ ns}$ and $\phi_d = 0.8$ respectively. For these parameters the Raman-Nath regime is valid as long as $\tau_p \ll 12 \mu\text{s}$ [155]. The state fidelity was calculated using time-of-flight method which will be discussed in a later section. Fig. 5.3, shows this calculated fidelity I as a function of pulse period l for different number of pulses $N = 2 - 5$. The simulation data shown in the plot was calculated using split-operator method which is explained in detail in chapter 8. The value of $\Delta\beta$ for carrying out the simulations was estimated from the measured trapping frequencies of the hybrid optical dipole trap in which the BEC was created. The trapping frequency measurement is shown in Fig. 2.4. For the mean value of the measured trapping frequencies ($129 \pm 7 \text{ Hz}$), the momentum width of the harmonic-oscillator ground state is $\Delta\beta = 0.0229 \pm 0.007$. The fidelity plots can be used to determine the sensitivity of the pulse sequence for Talbot time measurement. This is defined as $S = \Delta T/T_T = \Delta l/2$. To determine the experimental sensitivity S of the pulse scheme, a Gaussian peak is fitted between the first minimas on either side of the central maxima of the experimental $I(l)$ curves for each N and the width (Δl) thus obtained is used to calculate $S = \Delta l/2$ ($\Delta l = \sqrt{2} \times \text{standard deviation}$). Fig. 5.4 shows the variation of S as a function of N . We observe the experimental scaling exponent ($S \propto N^{-a}$) to be $a = -1.85 \pm 0.12$, which is smaller in magnitude than the expected value from Eq. 5.10 ($a = -3$). As mentioned before, this discrepancy can happen due to two reasons: (1). the asymptotic approximation is invalid or (2). the initial state as a plane wave is not a good approximation. For our experimental parameters (i.e. for $\phi_d = 0.8$), the values of S calculated using Eq. 5.6 and Eq. 5.10 differ significantly for low N but become close for $N = 4 - 5$. The two functions

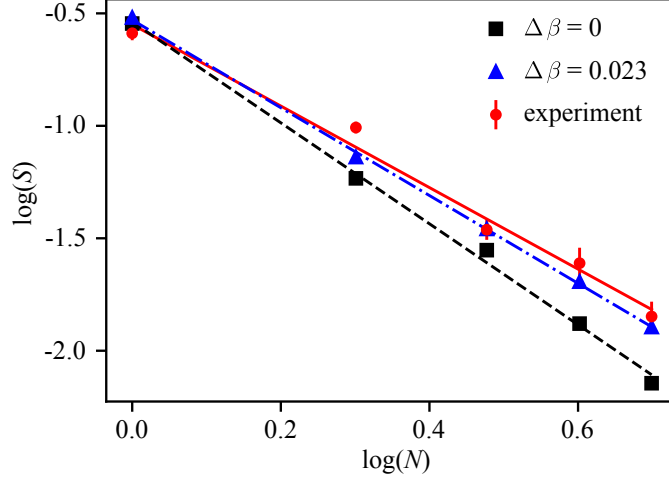


Figure 5.4: Scaling of sensitivity ($S = \Delta l/2$) with number of pulses ($N = 1 - 5$): using fidelities obtained from the experimental measurements (red circles), from the analytical equations with $\Delta\beta = 0$ (Eq. 5.6, black squares) and with $\Delta\beta = 0.0229$ (Eq. 5.11, blue triangles), each with linear fits for $\phi_d = 0.8$. The slopes of the linear fits are -1.85 ± 0.12 (red solid line), -2.23 (black dashed line) and -1.95 (blue dash-dot line). Eq. 5.6 and 5.11 were truncated to $n = \pm 20$ (convergence observed for $|n| \geq 7$).

converge for $N > 5$. The scaling exponent for $N \leq 5$ according to Eq. 5.6 is -2.23 . Thus, the reduced magnitude of the experimentally-derived value from -3 is mostly but not fully explained by the failure of the asymptotic approximation. We now look at the approximation of the initial state as a plane wave. This approximation will hold in the regime where the width of the initial wave-packet in momentum space is significantly narrower than the width of $I(l = 2, \beta)$ as calculated using Eq. 5.12. For $\phi_d = 0.8$, the width of $I(l = 2, \beta)$, at $N = 2$ is 0.021 . This is not significantly higher than the value of 0.023 , which our simulations and experiment suggest is the momentum width ($\Delta\beta$) of our BEC. Thus we can expect the experimentally observed reduction of the scaling of sensitivity with N for $N \geq 2$. For $N = 1$ and $\phi_d = 0.8$, the width of $I(l = 2, \beta)$ is ≈ 0.1 . Since $\Delta\beta = 0.02 < 0.1$, the plane wave approximation is valid. The value of S calculated using Eq. 5.6 for $N = 1$ and $\phi_d = 0.8$ is 0.285 , which is close to the experimentally obtained value of 0.26 ± 0.02 . We can also analytically calculate the fidelity for an ensemble possessing finite momentum width $\Delta\beta$ from Eq. 5.11. As seen in Fig. 5.4, the scaling exponent obtained from using this equation and $\Delta\beta = 0.0229$ is -1.95 . This value is within the error bounds of the experimentally determined value

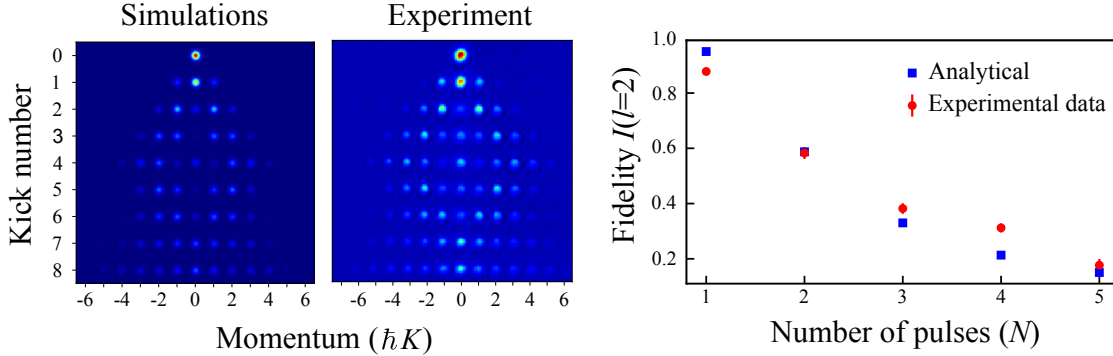


Figure 5.5: Suppression of resonant fidelity with number of pulses: (Left) The evolution of population in different momentum states as a function of kick number at resonant pulse period $l = 2$, where the phase of the lattice is inverted from kick 5 onward. The simulation data depicts the amount of population in each momentum state for parameters $\phi_d = 0.8$, $N = 4$ and $\Delta\beta = 0.023$. The experiment data contains the absorption images taken for $\phi_d \sim 0.8$ after 7 ms time of flight. (Right) Peak fidelity at resonance $I(l = 2)$ as a function of number of kicks N . The red dots are experimental data of fidelity at resonance and the blue squares are theoretical values obtained from Eq. for parameters $\phi_d = 0.8$ and $\Delta\beta = 0.023$. Error bars on experimental values indicate \pm one standard deviation over 5 data points.

of -1.85 ± 0.12 . These observations validate our model, where the finite momentum width of the initial state is responsible for a loss in the scaling of sensitivity S with the number of pulses N . We also observe that the fidelity is higher for off resonant periods for $N \geq 4$. This occurs due to reduction in the energy imparted to the atoms for off-resonant pulse periods. Though the suppression is less in than the anti-resonant pulse period ($l = 1$), the energy minima near $l = 1.73$ has been observed before in Ref. [153].

The suppression of fidelity at resonance ($l = 2$) with N , can be calculated by combining Eq. 5.11 and 5.12:

$$I'(l = 2) \simeq \int_{-0.5}^{0.5} G(\beta) J_0^2(4\pi N^2 \phi_d \beta) d\beta \quad (5.13)$$

The atoms which cause this suppression in fidelity because of finite β , leak to the other non zero momentum states $|n\hbar K\rangle$ as the phase shifted kick sequence is applied. This leaking of atoms to the non-zero momentum states can be observed in the evolution of momentum distribution for a BEC as a function of kicks, as shown in Fig. 5.5. In the simulations section of the figure, each momentum order is depicted by a Gaussian distribution whose total area is proportional to the simulated population occupied by

that order for $N = 4$, $\phi_d = 0.8$ and $\Delta\beta = 0.023$. The experiment section of the figure shows the absorption images taken after each kick for the same parameters.

5.3 AOKR as a velocity filter

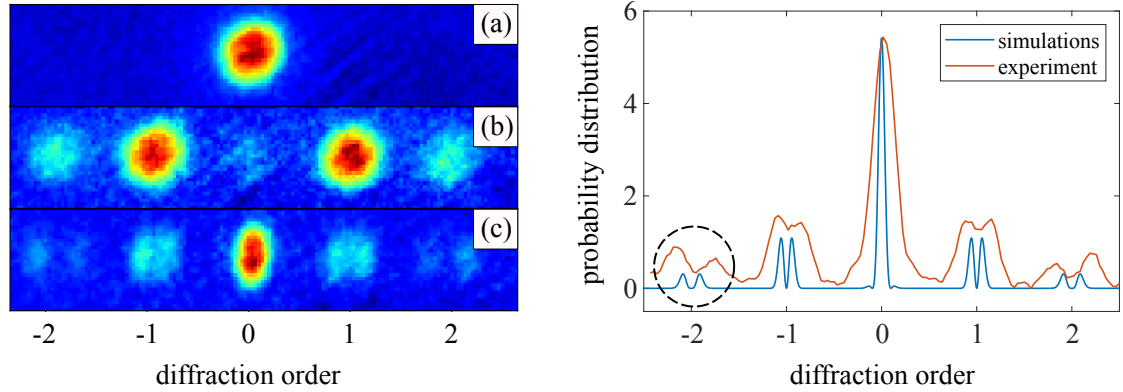


Figure 5.6: AOKR as a velocity filter: (Left) absorption images of the BEC subjected to two kicks ($\phi_d \sim 2.1$) with a relative lattice phase of π -radians between them. The pulse period was equal to the Talbot time. The kicks were delivered 5 ms after the trap release and images were captured after an additional 15 ms time-of-flight. In comparison to the un-kicked BEC (a), the narrowing of the zeroth momentum order profile in the direction of the lattice is clearly visible in (c). (Right) the absorption image data in (c) is integrated to give a line plot. The simulation data is also displayed for the parameters $\phi_d = 2.1$, $\Delta\beta = 0.031$. The dashed circle highlights the gap left in the second diffracted order due to momentum selectivity of the AOKR resonance.

The dependence of the initial state fidelity at resonant pulse period ($l = 2$) on deviation from zero momentum by an amount denoted by β (Eq. 5.12) gives rise to a momentum filtering action. Due to this selectivity, the atoms which return to the zeroth order after execution of the sequence, possess a narrower momentum distribution in comparison to the initial state. The filtering action can be seen in Fig. 5.6 for a two pulse sequence. In the figure, the BEC in (a) measures $0.33 \hbar K$ while the zeroth momentum state in (c) measures $0.17 \hbar K$. Thus, the post sequence profile of the zeroth order is twice as narrow. The effect of momentum selectivity is also seen in the other diffracted orders as gaps around the center of the order. This is seen in Fig. 5.6 (right), where the gap in the second order is highlighted by a dashed circle. These depleted regions in the higher orders represent atoms which have returned to the zeroth order as they are in a momentum state closer to an integer multiple of $\hbar K$. It can also be noticed that the gap in the first order is much narrower than the second order. This can

be explained as follows: an atom in the diffracted orders possess a momentum $(n + \beta)\hbar K$, where n is an integer. The free propagation phase contribution increases as n^2 and is relatively larger than the quasi-momentum phase $(\beta^2 + n\beta)$ for the second order in comparison to the first. This makes the atoms in the second order less sensitive to quasi-momentum phase and the gap in the momentum distribution more prominent. Reducing the momentum width of the initial ensemble is an important step in atom interferometry applications [127]. The AOKR sequence can be used as a momentum filter as demonstrated above [156]. It doesn't require a separate setup of laser beams for execution, as the AI diffraction beams themselves can be used for this purpose.

5.4 Conclusion

The results obtained here experimentally confirm, for the first time, the effect of finite width of the BEC on the Talbot time measurement sensitivity in the δ -kicked rotor schemes. The best measurement of Talbot time we obtain is $T_T = 65.567 \pm 0.0853 \mu\text{s}$ for $N = 4$ and $\phi_d = 0.8$. This translates to a relative uncertainty of 1.2×10^{-3} . Ref. [157], seems to have obtained similar measurement uncertainty using δ -kicked rotor with a cold thermal ensemble of ^{85}Rb atoms. The Talbot time is related to the atomic recoil frequency ω_r by the relation $T_T = \pi/2\omega_r$, which is in-turn related to the fine structure constant α as shown in Fig. 1.3. The current record for precision measurement of the atomic recoil frequency was accomplished using a Ramsey-Bordé atom interferometer where a relative uncertainty of 1.2×10^{-9} was achieved [53]. The recoil frequency has been measured by using Talbot resonances with a relative statistical uncertainty of 37×10^{-9} , however the systematic uncertainty is at 10^{-6} level [75]. Thus, the relative uncertainty that we obtain is far from the state-of-the-art measurements. As mentioned in the sensitivity can be improved by decreasing the momentum width of the initial momentum state. Initial states with momentum widths lower than the one used here have been reported in such as: $\Delta\beta = 0.008$ [158], 0.004 [73]. One can also use the technique of delta-kick cooling to lower the momentum width post BEC formation [159]. This has been demonstrated to produce very cold ensembles with temperatures: 50 pK [160], 1.3 nK [161].

While performing the phase-inversion sequence, it was noticed that when the phase

deviates significantly from π -radians the momentum distribution possessed an asymmetry. This occurs due to the breaking of the spatial symmetry of the Hamiltonian and is explored further in the next chapter.

Chapter 6

Asymmetry in AOKR

The results presented in this chapter have been published in:

“Effects of finite momentum width on the reversal dynamics in a BEC based atom optics δ -kicked rotor”

Jay Mangaonkar, Chetan Vishwakarma, S Sagar Maurya, Sumit Sarkar, Jamie L. MacLennan, Pranab Dutta and Umakant D. Rapol

Journal of Physics B: Atomic, Molecular and Optical Physics, 53, 235502 (2020)

This chapter describes the lattice-phase dependent intra-order and inter-order asymmetry observed in the momentum distribution post kicking. The inter-order asymmetry can be useful as an alternative technique to measure Talbot time. Both of these asymmetries can be used to monitor the phase drift of the lattice.

6.1 Intra-order asymmetry

The δ -kicked rotor dynamics gives rise to two types of asymmetries in the momentum distribution after application of the kick sequence. Both of them occur due to the relative lattice phase between the first and last sets of N pulses deviating from π . The first kind of asymmetry is seen in the quasi-momentum distribution within the diffracted orders and occurs at the resonant condition $l = 2$. One can derive a simplified expression for this asymmetry for a case of two pulses ($N = 1$) using a position space treatment as outlined in Ref. [139]. Thus, if c_{kj} denotes the probability of occupation in the state

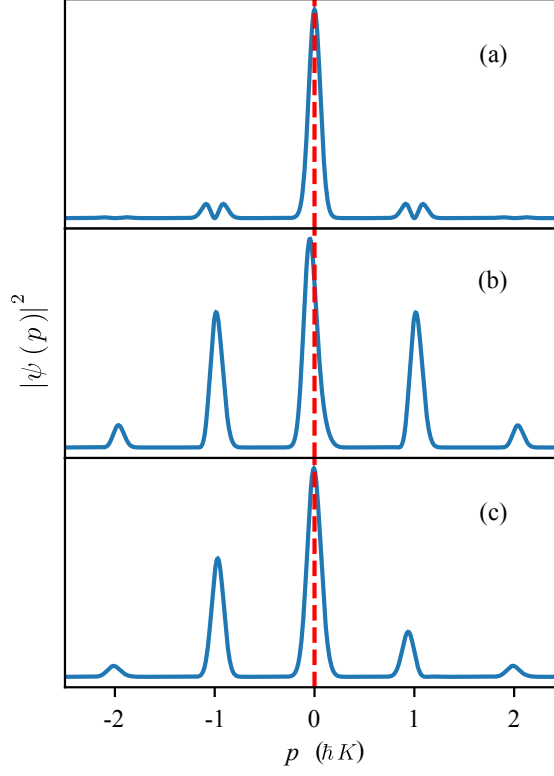


Figure 6.1: Intra-order and inter-order asymmetry: Simulated momentum distribution after an initial Gaussian wave-packet centered at $j = 0$ with momentum spread $\Delta\beta = 0.05$ is subjected to two pulses of kick strength $\phi_d = 0.8$. The red dashed line indicates $k, \beta = 0$. (a) Here, the pulse period is $l = 2$ and the relative lattice phase between the two pulses is $\Phi = \pi$. The distribution is symmetric about $\beta = 0$ for each j and no net momentum current is present. (b) At $l = 2$ and $\Phi = \pi + 2$, the asymmetry in the β distribution of $j = 0$ is clearly visible. As explained in the text, no net current is induced despite of the asymmetry. (c) For $\Phi = \pi + 0.5$ and $l = 1.5$, a net momentum current is induced, as seen in the population difference between the 1 and -1 orders. The y -axis scale is not the same for the three cases.

$|j + \beta\rangle$, with initial state being $|k + \beta\rangle$:

$$c_{kj}(\beta, \Phi) = J_{j-k}^2 \left[2\phi_d \cos \left(\frac{2\pi(1 + 2\beta) - \Phi}{2} \right) \right] \quad (6.1)$$

Here, β is the conserved quasi-momentum and Φ is the relative lattice phase shift between the two kicks. As seen in Eq. 6.1, for a fixed phase Φ and kick strength ϕ_d , the value of $c_{kj}(\beta, \Phi)$ will vary with the sign of β . This variation breaks the symmetry of momentum distribution in β about a discrete order k after application of the kick sequence. In Fig. 6.1(b), this asymmetry can be seen in the simulated distribution for two

kicks. For an initial state with a Gaussian distribution $G(\beta)$ centered around $k = 0$, the intra-order asymmetry in the j^{th} order can be defined as:

$$A_j(\Phi) = \frac{\int_{-0.5}^0 C_j(\beta, \Phi) d\beta - \int_0^{0.5} C_j(\beta, \Phi) d\beta}{\int_{-0.5}^0 C_j(\beta, \Phi) d\beta + \int_0^{0.5} C_j(\beta, \Phi) d\beta} \quad (6.2)$$

Where, $C_j(\beta, \Phi) = G(\beta)c_{0j}(\beta, \Phi)$. Any change in the occupation of the $|0 + \beta\rangle$ state from its initial value has to be balanced by an opposite change in the rest of the $|j + \beta\rangle$ states, as $\sum J_n^2(\alpha) = 1$, for a fixed argument α . This results in the sign of the asymmetry $A_j(\Phi)$ for $j = 0$ being opposite to that of the rest of the orders. Furthermore, $J_{-j}^2(\alpha) = J_j^2(\alpha)$, making the populations of any symmetric orders equal, as seen in Fig. 6.2. Thus, the phase offset between the two kicks gives rise to a curious phenomenon where a net asymmetry is present in the system without a net current. The sign of this asymmetry changes as the phase Φ is swept across π .

We study this asymmetry for $N = 1$, which is a simple case to theoretically model. As seen in Eq. 6.1, this asymmetry is tunable with the lattice phase of the second kick. This can be clearly seen in the experimental distribution plotted in Fig. 6.2 (top right panel), where the quasi-momentum distribution of each order differs across the $\beta = 0$ value. Fig. 6.2 (top left panel) plots the asymmetry as defined in Eq. 6.2. As expected, the sign of this asymmetry for $j = 0$ is opposite to that of $j = \pm 1$. The total population in $j = \pm 1$ is observed to be equal, implying the absence of a net momentum current. The asymmetry undergoes a sign change as the lattice phase Φ is scanned across π radians which can be seen in Fig. 6.2 (top left panel). The data for observing this asymmetry effect was taken at a relatively larger time-of-flight of 20 ms, to resolve the sub-recoil structure within the diffracted orders. Although the sub-recoil structure has been previously shown to be affected by the resonance dynamics in AOKR experiments [153], this is the first characterization of an asymmetry present within the momentum state distribution of the diffracted orders.

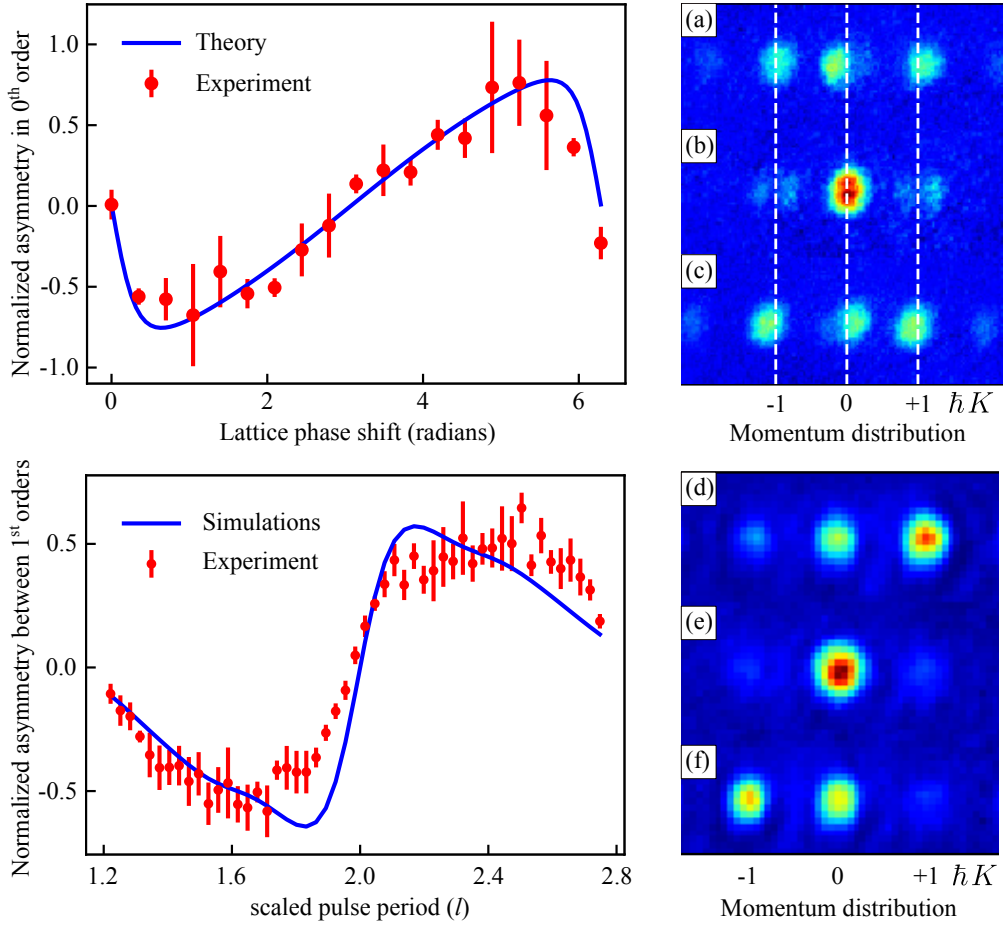


Figure 6.2: **Top left:** Intra-order asymmetry for $N = 1$ as a function of the lattice phase. The asymmetry (A_{00} in Eq. 6.2) is calculated as $(n_+ - n_-)/(n_+ + n_-)$, where n_+ and n_- denote the integrated probability density in the positive and the negative sections of the 0^{th} order momentum bin ($-0.5 \leq \beta < 0.5$). Red dots denote the average experimental asymmetry value over 3 data points. Blue solid line denotes the theoretically calculated value for $\phi_d = 1.15$ and $\Delta\beta = 0.023$ using Eq. 6.2. **Top right:** experimental absorption images taken after 20 ms time-of-flight for the following lattice phase settings $\Phi =$ (a) $\pi/3$, (b) π and (c) $5\pi/3$ radians. White dashed lines indicate the $\beta = 0$ position at each discrete momentum bin. **Bottom left:** Inter-order population asymmetry for $N = 1$ as a function of pulse period, at a fixed lattice phase. The asymmetry here is calculated in the same manner as above, where n_+ and n_- denote the integrated probability density in first order diffracted populations ($\pm 1 \hbar K$). Red dots denote the average experimental asymmetry value over 5 data points. Blue solid line denotes the simulated curve for $\phi_d = 0.8$, $\Delta\beta = 0.023$ and $\Phi = \pi + 0.35$. **Bottom right:** experimental absorption images taken after 7 ms time-of-flight for the following pulse periods $l =$ (d) 1.4, (e) 2 and (f) 2.5. Error bars in both the figures denote \pm one standard deviation.

6.2 Inter-order asymmetry

The second type of asymmetry is observed as a population difference between any pair of orders j and $-j$, when there is a phase offset from the reversal phase π for an initial state $k = 0$. This phase offset breaks the spatial symmetry of the kick-potential, inducing a net momentum current in the wavefunction, which can be seen in Fig. 6.1(c). As explained in the previous section, the population c_{kj} of any pair of orders $\pm j$ is the same for $l = 2$, resulting in zero asymmetry. Unlike the first case which is at resonance $l = 2$, no simple expression for c_{kj} can be derived in this case (lattice phase difference is a non-integer multiple of π and off resonant pulse period). Previous demonstrations of a net current in BEC based AOKR systems have been performed by using asymmetric potentials [162] and accelerator modes [163, 164] at resonant or near resonant conditions. However, a net current is manifested in our case for a zero-momentum initial state at pulse periods away from resonance.

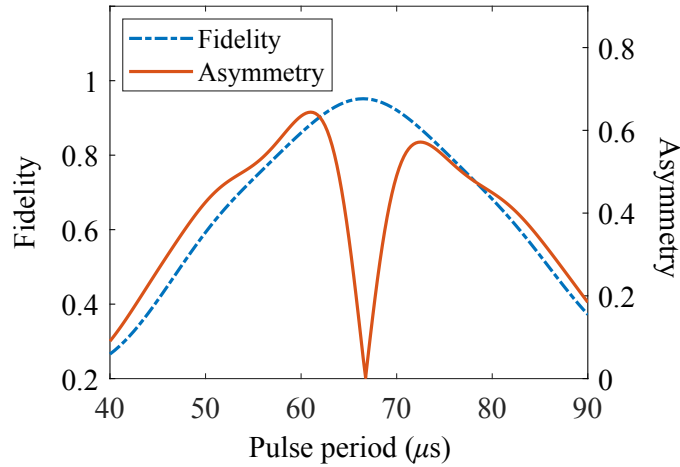


Figure 6.3: Comparison of asymmetry and fidelity for the measurement of Talbot time: The blue dash-dot line denotes the simulated fidelity for a two kick sequence based on the phase reversal scheme explained in section 5. The red solid curve denotes the simulated absolute value of the asymmetry for a two kick sequence as defined in Fig. 6.2. It can be clearly seen that the asymmetry signature is much narrower than the fidelity near resonance, for the same kick strength ($\phi_d = 0.8$) and initial state momentum width ($\Delta\beta = 0.023$). The phase offset between the two kicks for the asymmetry plot is 0.35 rad.

As seen in Fig. 6.2 (bottom left panel), this kind of asymmetry peaks at pulse periods away from resonance. It is quantified by the normalized population difference between

the first order diffraction population ($\pm 1 \hbar K$) as plotted in Fig. 6.2 (bottom left panel). The net momentum current induced is apparent in the absorption images shown in the Fig. 6.2 (bottom right panel). We compare the temporal response of this asymmetry with that of the initial state fidelity. For $N = 1$ and $\phi_d = 0.8$, the observed standard deviation in fidelity is 0.37. In comparison, the asymmetry reaches 0.61 times its peak signal of ≈ 0.5 in $l - 2 = 0.07$. Thus, the response of inter-order asymmetry is about 5.3 times sharper around resonance. This enhancement in sensitivity suggests that intra-order asymmetry can be used to measure Talbot time. Fig. 6.3 shows a simulated comparison between the fidelity based sequence and the inter-order asymmetry signature for the same set of parameters, where this enhancement in sensitivity is clearly visible. Further investigation is required for optimal definition of asymmetry as the number of diffracted orders grows. The effect can also be used as a coherent asymmetric beam splitter for BEC based interferometers [165]. Since the interaction time for Raman-Nath pulses is at least an order of magnitude less than the Bragg based beam splitters, using them can reduce the undesired AC-Stark phase shift associated with the pulse [166]. The zero-crossing signal obtained from the asymmetry effects can be used to diagnose any undesired phase shifts in the kick sequence at resonant and off-resonant pulse periods. Such phase shifts induced due to lattice vibrations can be a detriment in the applications of BEC based AOKR experiments to implement quantum walks in momentum space [71, 167].

Chapter 7

Quantum ratchet

The experiments with δ -kicked rotor in the previous chapters concerned with a plane wave initial state possessing a single momentum component. The position distribution of such a state is spatially uniform. When the spatial symmetry of the initial state is broken one can achieve a net momentum current with the application of δ -kicked rotor pulses. This current arises even though the driving optical lattice potential possess spatial symmetry and is hence unbiased. Such net motion in the absence of a biased drive force is known as the ratchet effect. The ratchet motion in classical microscopic systems arises from random dissipative processes such as Brownian motion [168] and is the underlying mechanism for the conversion of chemical energy to directed motion in tiny biological motors [169]. The conditions for realization of the ratchet motion in quantum systems were explained in Ref. [170]. Here, it was predicted that directed motion in quantum Hamiltonians with spatial and temporal periodicity, can arise when the underlying classical Hamiltonian has a mixed phase space. The ratchet effect has been demonstrated in quantum systems such as Josephson junction arrays [171], photons [172] and ultra-cold atoms [70].

In the ultra-cold atomic system, ratchet motion has been induced using an asymmetric driving potential [162, 173], lattice phase modulation [164, 174, 175] and engineering the initial momentum state [70]. The method of engineering the initial momentum state is interesting as it has been theoretically predicted to produce momentum distributions with tailored spread under the action of resonant δ -kicked rotor pulses [86].

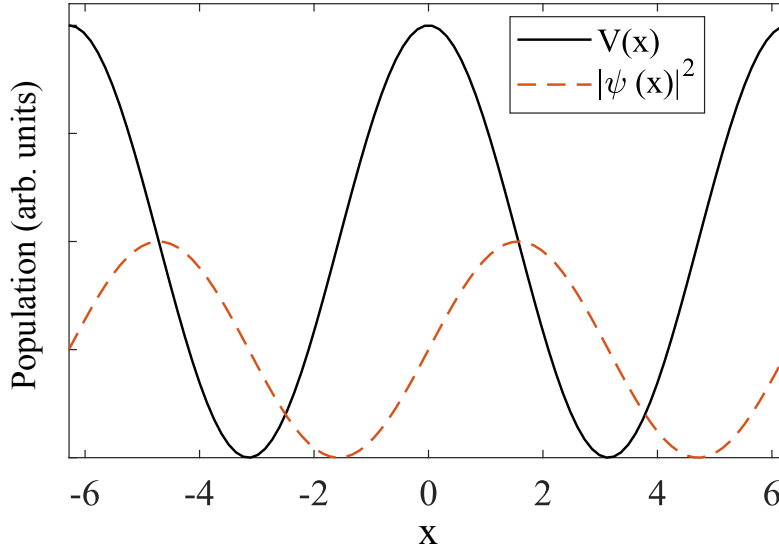


Figure 7.1: Gradient force on atoms: The distribution of the wavefunction $\psi(x) = |0 \hbar K\rangle + e^{i\pi/2} |1 \hbar K\rangle = 1 + ie^{iKx}$ is shown in position space alongside the optical lattice potential $V(x) = \cos(Kx)$. The maximum gradient of the potential coincides with the peak of the distribution. The force due to this gradient drives the ratchet.

Such control over the momentum distribution is desirable as the δ -kicked rotor is an emerging platform to perform quantum random walks in momentum space [71]. The dependence of the ratchet current on the initial state preparation has been extensively studied [163, 176, 177]. Its replication that we present here serves to demonstrate the capability of our setup for coherent preparation of asymmetric momentum states.

As mentioned previously, an asymmetric momentum state is needed for the directional motion to take place. This is done by utilizing Bragg diffraction. As described in section, one can create a coherent momentum state with almost equal population in the zeroth and any diffracted order with this technique. For this experiment, the Bragg pulse duration is kept as $66.34 \mu\text{s}$ so that the free propagation phase gathered by the first order during preparation is unity. Thus, the initial state at the end of the Bragg pulse is given by:

$$\psi = \frac{1}{\sqrt{2}}(|0 \hbar K\rangle + e^{i\gamma} |1 \hbar K\rangle) \quad (7.1)$$

Here, γ is the phase of the optical lattice when the Bragg pulse is being applied. The probability distribution $P(x)$ corresponding to this wavefunction in position space then

becomes [163]:

$$P(x) = |\psi(x)|^2 = \frac{1}{2\pi} [1 + \cos(x + \gamma)] \quad (7.2)$$

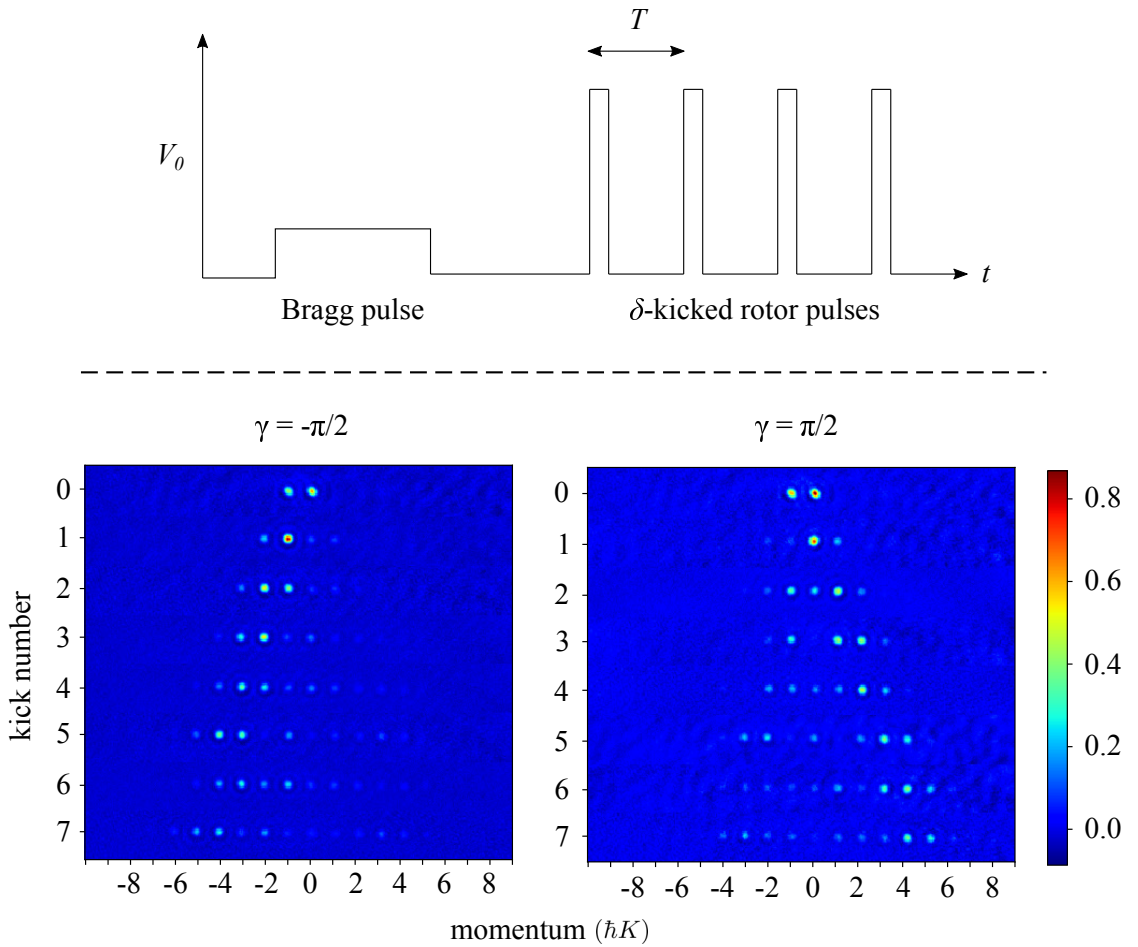


Figure 7.2: Realization of a quantum ratchet: Top: Pulse schematic for creation of the quantum ratchet. The Bragg pulse prepares the initial state which is then subjected to the δ -kicked rotor pulses. The phase offset of the optical lattice between the Bragg and the kicked rotor pulses was γ . The kicked rotor pulses were applied with a resonant period of $T = 33.17 \mu\text{s}$ and a frequency detuning of $\sim 15 \text{ kHz}$ between the kicking beams. The kick strength was kept as $\phi_d \sim 1$. **Bottom:** Time-of-flight images of the BEC after application the Bragg and δ -kicked rotor pulses. The color-bar indicates optical density.

After the preparation pulse is over, the phase of the optical lattice is adjusted such that its relative phase between w.r.t the Bragg pulse optical lattice is γ . In our setup this is done by using two phase locked function generators as described in chapter 3. Fig. 7.1 shows the position distribution of the wavefunction alongside the optical lattice potential

over two grating periods. When $\gamma = \pi/2$, the peak of the distribution $|\psi(x)|^2$ coincides with the maximum gradient of $V(x)$. Thus, when the optical pulse is applied, the atomic wavefunction feels a force in the direction defined by this gradient. If the phase is adjusted such that $\gamma = -\pi/2$, the direction of this force and thus that of the ratchet can be reversed. We keep the frequency difference between the kicking beams at 15 kHz and the kick period as $33.17 \mu\text{s}$ to be at Talbot resonance [73]. The experimentally obtained results are shown in Fig. 7.2, where the reversal of the ratchet current with lattice phase is clearly visible.

Chapter 8

Numerical methods

To simulate the evolution of a cold atom ensemble under the action of a sinusoidal optical potential in different parameter regimes, we use the split-operator method. It was proposed in Ref. [178] and has been successfully used to tackle a variety of problems concerning the solution of time-dependent Schrödinger equation. It uses discrete Fourier transform at its heart, for which a very fast algorithm is available [179]. The central tenet of the method is that the evolution operator $\exp(-i\hat{H}\Delta t/\hbar)$ can be split into $\hat{U}_p(\Delta t) \times \hat{U}_x(\Delta t)$ where, $\hat{U}_p(\Delta t) = \exp(-i\hat{p}^2\Delta t/2m\hbar)$ and $\hat{U}_x(\Delta t) = \exp(-iV(\hat{x})\Delta t/\hbar)$. Here, an error of the order of $O(\Delta t^2)$ is accumulated due to non-commutativity of \hat{U}_x and \hat{U}_p . The evolution unitary for a time step Δt is thus given as:

$$\hat{U}(t + \Delta t, t) \approx \hat{U}_p(\Delta t)\hat{U}_x(\Delta t) + O(\Delta t^2) \quad (8.1)$$

One can gain back an order of in accuracy by using the Baker-Campbell-Hausdorff theorem. This is called ‘Strang splitting’ [180].

$$\hat{U}(t + \Delta t, t) \approx \hat{U}_p(\Delta t/2)\hat{U}_x(\Delta t)\hat{U}_p(\Delta t/2) + O(\Delta t^3) \quad (8.2)$$

Thus, for n steps in time:

$$\hat{U}(t + n\Delta t, t) \approx \hat{U}_p(\Delta t/2)\hat{U}_x(\Delta t) \left(\prod_{n=1} \hat{U}_p(\Delta t)\hat{U}_x(\Delta t) \right) \hat{U}_p(\Delta t/2) + O(\Delta t^3) \quad (8.3)$$

In the spatial domain, application of the momentum evolution operator U_p is non-trivial as it involves a derivative. This operation in the momentum domain is achieved by simply multiplying the wavefunction by $\exp(-ip^2\Delta t/2m\hbar)$. Thus we switch back and forth from the momentum and position representations by Fourier transform for the application of the operators \hat{U}_p and \hat{U}_x respectively. For computation, we need to discretize the position and momentum space. The discrete approximation of the continuous Fourier transform looks like:

$$\phi(k, t) = \frac{1}{\sqrt{2\pi}} \int_{-\infty}^{\infty} \psi(x, t) e^{-ikx} dx \rightarrow \phi(k_m, t) \approx \frac{\Delta x}{\sqrt{2\pi}} \sum_{n=0}^{N-1} \psi(x_n, t) e^{-ik_m x_n} \quad (8.4)$$

Where we have switched the momentum notation to the so called k -space ($p = \hbar k$) to get rid of the \hbar in normalization of the Fourier transform. The x -space has been partitioned into N points which makes the corresponding k -space spacing to be $\Delta k = 2\pi/N\Delta x$. The code written in Python 2.7.15 that is used for implementing this routine for evolution under an optical lattice potential having a spatial periodicity of $2\pi/K_0$, is given below. Note that the physical quantities in the code are scaled in the following manner: $V(x) \rightarrow V(x)/E_r$, $t \rightarrow t\omega_r$, $x \rightarrow xK_0$, $k \rightarrow k/K_0$. The recoil energy, $E_r = \hbar^2 K_0^2/2m = \hbar\omega_r$, is the energy of an atom of mass m after exchange of two photons from the optical lattice field.

The code implemented in Python 2.7 is given below:

```

1
2 import matplotlib.pyplot as plt
3 import numpy as np
4 from scipy.fftpack import fft, ifft
5
6 #setting up simulation parameters

```

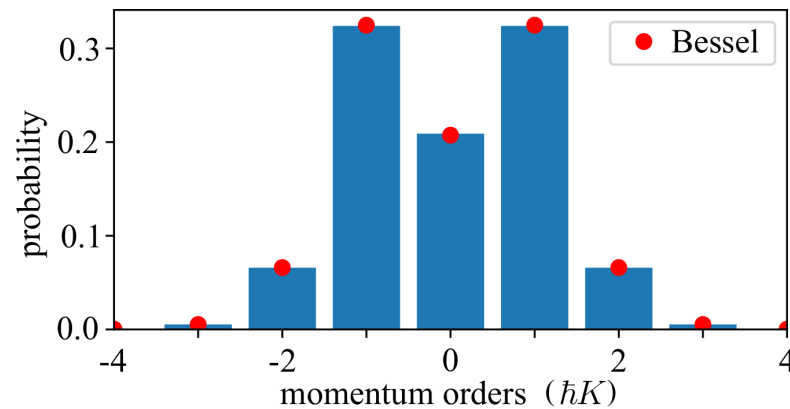


Figure 8.1: Simulated momentum distribution in the Raman-Nath regime. The simulation parameters are: potential depth $V_0 = 160 \hbar\omega_r$ and interaction time $t = 0.01 \omega_r^{-1}$. Since the parameters satisfy the Raman-Nath regime, the population distribution follows a Bessel distribution $J_n^2(V_0 t/\hbar)$, where n is the diffraction order.

```

7
8 time_division = 100 #number of temporal subdivisions
9 time_final   = 0.01 #final evolution time in units of recoil
   frequency
10 dt          = time_final/time_division #resolution in time
11 t_grid      = np.linspace(0,time_final,time_division)
12 x_max       = 40 #max extent of x_space in terms of lattice period
13 dx          = 0.01 #resolution in x_space
14 x           = np.arange(-x_max,x_max+dx,dx) #x_space
15 N           = len(x) #number of steps in space
16 k           = np.concatenate((np.arange(0,(N-1)*0.5+1,1),np.arange
   (- (N-1)*0.5,0,1)),axis=0)*(2*np.pi/(N*dx)) #k_space
17 k_mod       = np.roll(k,(len(k)-1)/2) #used for plotting
   convenience
18 V           = 160 #standing wave potential in units of recoil
   energy
19 dk          = (2*np.pi/(N*dx)) #step in momentum grid
20
21
22 #Define evolution operators
23
24 Vx          = V*np.cos(x) #periodic static potential
25 Vk          = k**2 #kinetic energy

```

```

26 Ux      = np.exp(-1j*Vx*dt)      #full time-step operator in x space
27 Uf      = np.exp(-1j*Vk*dt)      #full time-step operator in k space
28 Ufh     = np.exp(-1j*Vk*dt/2.0)  #half time-step operator in k space
29
30
31 #Prepare the initial state in space domain
32
33 sigma_K  = 0.02                  #scaled width in k_space
34 mu       = 0                    #offset in x_space
35 sigma    = 1/(2*sigma_K)        #width in x_space
36
37 def Gauss(x):
38     return np.exp(-0.5*(((x-mu)/sigma)**2))
39
40 psi_0     = Gauss(x)            #initialized as a Gaussian
41 psi_x_initial = psi_0
42 psi_p_initial = fft(psi_x_initial)
43 norm      = np.sum(np.abs(psi_p_initial)**2) #normalization
         factor for momentum distribution
44
45
46 ##### Begin evolution #####
47
48 psi_0 = fft(psi_0)
49 psi_0 = psi_0*Ufh
50 psi_0 = ifft(psi_0)
51 psi_0 = psi_0*Ux
52
53 for i in range(len(t_grid)-1):
54
55     psi_0 = fft(psi_0)
56     psi_0 = psi_0*Uf
57     psi_0 = ifft(psi_0)
58     psi_0 = psi_0*Ux
59
60     if i%(np.int(0.1*(len(t_grid)-1))) == 0: #displays % completion of
         loop in units of 10%
61     q = i/np.int((0.1*(len(t_grid)-1)))

```

```

62 print str((q+1)*10) + '% complete'
63
64 psi_0 = fft(psi_0)
65 psi_0 = psi_0*Ufh
66
67 ##### End evolution #####
68
69 psi_0_mod = np.roll(psi_0, (len(k)-1)/2) #rearrange for displaying
70
71 k_prob_density      = (np.abs(psi_0_mod)**2)/norm #normalized
    probabiliy index
72 k_max              = np.int(np.ceil(np.max(k_mod)))-1 #max val
    discrete k bin
73 store_int_pop      = np.zeros(2*k_max+1)          #
    store amount of population in each discrete k bin
74 discrete_index_array = np.arange(-k_max,k_max+1,1) #discrete k values
75 Bessel_array       = np.zeros(2*k_max+1)         #to store values
    according to Bessel formula
76 max_order          = np.int(len(Bessel_array)*0.5) #maximum order
    of diffraction
77
78 for i in range(len(discrete_index_array)): #loop for summing up
    quasimomentum in each discrete bin
79 indices = np.zeros(len(k_mod), dtype=bool)
80 for j in range(len(k_mod)):
81 indices[j] = discrete_index_array[i]+0.5 > k_mod[j] >
    discrete_index_array[i]-0.5
82 store_int_pop[i] = np.sum(k_prob_density[indices])
83
84 Bessel_array[i] = special.jv(np.int((i-max_order)),V*time_final)**2
85
86 plt.figure(figsize=(5,5))
87 plt.plot(discrete_index_array,Bessel_array,'ro', label ='Bessel')
88 plt.bar(discrete_index_array,store_int_pop)
89 plt.xlabel("Momentum orders ( $\hbar K$ )")
90 plt.ylabel("Probability")
91 plt.legend(loc='upper right')

```

Running the code as it is given above will generate a plot of the momentum distribution a narrow momentum wave-packet under the action of a standing wave potential which is displayed in Fig. 8.1. The momentum distribution is binned in units of the wave-number of the optical lattice potential (K_0). As seen in the plot, the distribution matches the calculated values matches the expected values under the Raman-Nath approximation. This code can be easily modified to realize different spatial and temporal profile than the one which we are interested in here.

Chapter 9

Conclusion and future experiments

9.1 Summary

9.1.1 Realization and characterization of BEC

The primary motivation of this thesis was to setup and characterize a BEC based δ -kicked rotor (AOKR) interferometer experiment for a fidelity based measurement of Talbot time. The pulse scheme that was experimentally demonstrated here was originally proposed in Ref. [82]. The initial state used as an input for this interferometer was a BEC of ^{87}Rb atoms obtained after laser cooling in a MOT and subsequent evaporative cooling in an hybrid optical crossed dipole trap. Since the quasi-momentum dynamics were theoretically predicted to play an important role in the dynamics of the AOKR pulse scheme, the characterization of the BEC initial state and its evolution was done. The Thomas-Fermi radius and thus the momentum width of the BEC in trap was estimated by measuring the trapping frequencies. These measurements were used to study the expansion dynamics of the BEC upon release from the trap and the results were in agreement with the theoretical model.

9.1.2 Preliminary experiments with diffraction using an optical lattice

The BEC thus obtained was subjected to a standing wave lattice of far-detuned laser radiation ($\lambda = 780 \text{ nm}$). The phase modulation of the BEC wavefunction causes it

to diffract into discrete momentum states separated by $\hbar K$, $K = 4\pi/\lambda$ being the lattice constant. This diffraction was studied in two different interaction regimes i.e. the Raman-Nath regime (short pulse duration) and the Bragg regime (long pulse duration). Diffraction in the Raman-Nath regime was then used to realize the δ -kicked rotor Hamiltonian using BEC as the initial state. This is called the atom-optics δ -kicked rotor or AOKR. The Talbot resonances, a unique feature of the quantum δ -kicked rotor, were observed at a pulse period of $T \sim 66 \mu\text{s}$ (resonant effect) and $T \sim 33 \mu\text{s}$ (anti-resonant effect). The revival of the initial momentum state in anti-resonant Talbot effect occurs due to cancellation of phase modulation of two subsequent pulses. This is the basic principle behind the Talbot time measurement schemes that were tested.

9.1.3 AOKR pulse scheme for measurement of Talbot time

The Talbot time measurement pulse schemes were based on the principle of initial state revival or fidelity (I) when the pulse period was set to Talbot time. In this case the cancellation of lattice phase modulation was induced by inverting its sign. This inversion was carried out by shifting the phase of the optical standing wave by π radians. In pulse scheme-1, the sign inverted pulse was applied with a kick strength of $N\phi_d$ after N pulses. Thus, when the pulse period was set to Talbot time, initial state fidelity was maximum. The sensitivity (S) of this pulse sequence i.e. the FWHM of I as a function of deviation from Talbot time $\epsilon = l - 2$ was proposed in Ref. [154] to decrease favorably as N^{-3} . We carried out this pulse sequence to benchmark the lattice phase inversion experimentally. The pulse sequence-2 circumvented the need of ramping up the power of the final pulse in sequence-1 by replacing it with another phase inverted N pulses having the same kick strength. The observed sensitivity for this sequence differed significantly from the theoretically predicted one for a plane wave. The observed scaling factor here was $a = -1.85 \pm 0.12$ differing from the ideal $a = -3$, where $S = N^a$. This is the first reported deviation of the scale factor from -3 which was predicted in Ref. [83]. Analysis showed that the difference arises whenever the sensitivity of the pulse sequence to the deviation of the initial momentum state from $0 \hbar K$ (ideal plane wave state), becomes narrower than the momentum width of the initial state. This amounts to breakdown of the approximation of BEC as a plane wave state. The best measurement of Talbot time

we obtain is $T_T = 65.567 \pm 0.0853 \mu\text{s}$ for $N = 4$ and $\phi_d = 0.8$. Ref. [157], seems to have obtained similar precision using δ -kicked rotor with a cold thermal ensemble of ^{85}Rb atoms. The sensitivity can be improved by decreasing the momentum width of the initial momentum state. Initial states with momentum widths lower than the one used here have been reported in such as: $\Delta\beta = 0.008$ [158], 0.004 [73].

In the context of the phase reversal sequence as a continuous-time quantum walk, the finite momentum width of the initial state needs to be considered while executing recently proposed schemes [85, 86]. The quantum-walk-based search algorithm described in Ref. [85] relies on detecting atoms of a predefined tagged momentum state, essentially demanding the reversal of wavepackets at non-tagged momentum states with high fidelity. The finite momentum width results are also important for simulation of quantum systems using AOKR as seen in Ref. [167]. Here, the simulated signature of the topological phase becomes distorted for distributions $\Delta\beta \sim 0.03$. Thus the effect of finite momentum width on reversal fidelity that we report, plays an important role in the above mentioned quantum walker dynamics.

9.1.4 Asymmetry in momentum distribution

While execution of the phase-inversion pulse sequences, it was observed that the momentum distribution within a diffracted order and the population of the orders about zero state, showed an asymmetry when the phase differed from π radians. This intra-order and inter-order asymmetry was characterized for the case of two pulses. The intra-order asymmetry has been previously unreported and is unique as it possess a net asymmetry without a net momentum current. The response of inter-order asymmetry is about 5.3 times sharper around resonance in comparison to fidelity for the same parameters. This enhancement in sensitivity suggests that intra-order asymmetry can be used as a probe in AOKR experiments. The effect can also be used as a coherent asymmetric beam splitter for BEC based interferometers [165]. Since the interaction time for Raman-Nath pulses is at least an order of magnitude less than the Bragg based beam splitters, using them can reduce the undesired AC-Stark phase shift associated with the pulse [166]. The zero-crossing signal obtained from the asymmetry effects can be used to diagnose any undesired phase shifts in the kick sequence at resonant and off-resonant pulse periods.

Such phase shifts induced due to lattice vibrations can be a detriment in the applications of BEC based AOKR experiments to implement quantum walks in momentum space [71, 167].

9.2 Future experiments

9.2.1 Continuous-time quantum walk (CTQW) with AOKR

The difference between a discrete quantum walk and a continuous one is the absence of the coin degree of freedom in the later. Ref. [85] proposes the realization of a quantum search algorithm using a BEC based CTQW. In this proposal, a uniform momentum state distribution is created by initiating the sequence with a coherent multi-component momentum state such that:

$$|\psi\rangle = \frac{1}{\sqrt{5}} (C_{-2} |-2\rangle + C_{-1} |-1\rangle + C_0 |0\rangle + C_1 |1\rangle + C_2 |2\rangle) \quad (9.1)$$

Where, $|n\rangle$ denotes the n^{th} diffraction order. An arbitrary combination of such states can be created by a Bragg pulse sequence. An example of this is the demonstration of a quantum ratchet in chapter 7 (Fig. 7.2), where the phase between the two participating states was used to steer the symmetry of the final distribution. As shown in Ref. [86], for certain values of the state coefficients C_n , subjecting the prepared state to δ -pulses at Talbot time creates an ensemble with almost uniform distribution. One can then use velocity selective Raman pulses to invert the phase of a particular diffraction order [181]. This ‘tagged’ momentum state from the uniform ensemble will then separate out at the end of the sequence. The reversal sequence without this momentum selective tagging has been realized in this thesis for 5 steps (Fig. 5.5).

9.2.2 Effect of interactions on the Talbot effect

This is a relatively unexplored area in BEC based AOKR. Most of the experiments are carried out in the regime after the interaction energy of the condensate has been converted to the kinetic energy. Ref. [182] predicts that the anti-resonance fidelity decreases with an increase in the interaction energy. Surprisingly, it also predicts that the state reversal is recovered upon being in the parameter range where the underlying classical

phase-space is chaotic. In ^{87}Rb the interaction term can be increased by accessing the magnetic [183] or optical Feshbach resonances [184].

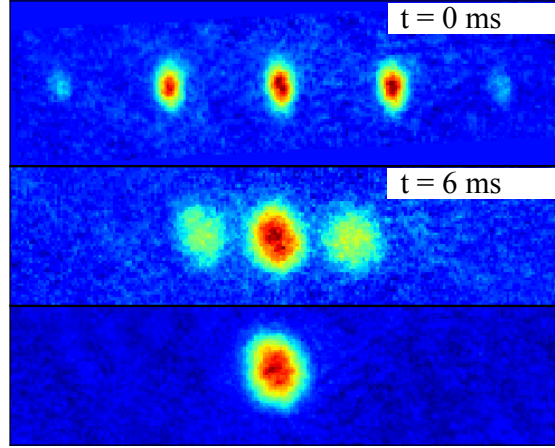


Figure 9.1: Diffraction profile for different pulse application times: In the first row the optical lattice pulse was applied immediately after releasing the BEC from the trap ($t = 0$ ms). It can be seen that the diffraction orders are significantly narrower in comparison to the case where the pulse is applied much later ($t = 6$ ms). No pulse is applied in the last row. All images are taken after 20 ms from the trap release.

There is another effect which is observed in the diffraction profile of the BEC which is possibly interaction induced. As seen in Fig. 9.1, when the optical lattice pulse is applied immediately after the BEC is released from the trap, the diffraction profile of the orders appear to be significantly narrow in comparison to the same when the pulse is applied a few milliseconds later. When the BEC is immediately released from the trap it takes sometime for the interaction energy to be released as kinetic energy. This can be seen in Fig. 2.7, where the accelerated expansion ceases past $\tau > 2$. For our case i.e. $\omega_0 = 2\pi \times 130$ Hz, the expansion ceases past $t > 2.5$ ms. Further simulation and experimental study is required to conclude the origins of this effect.

9.2.3 Realization of asymmetric beam splitter and combiner with AOKR

The $\pi/2$ Bragg pulse in a traditional Mark-Zehnder AI configuration can be replaced by an asymmetric AOKR beam splitter to couple the zeroth and the first diffracted order. As shown in Fig. 9.2 this AOKR beam splitter consists of a δ -pulse pair. The time separation of the pulse pair is away from the Talbot time ($l_1 \neq 2$) and there is a lattice phase

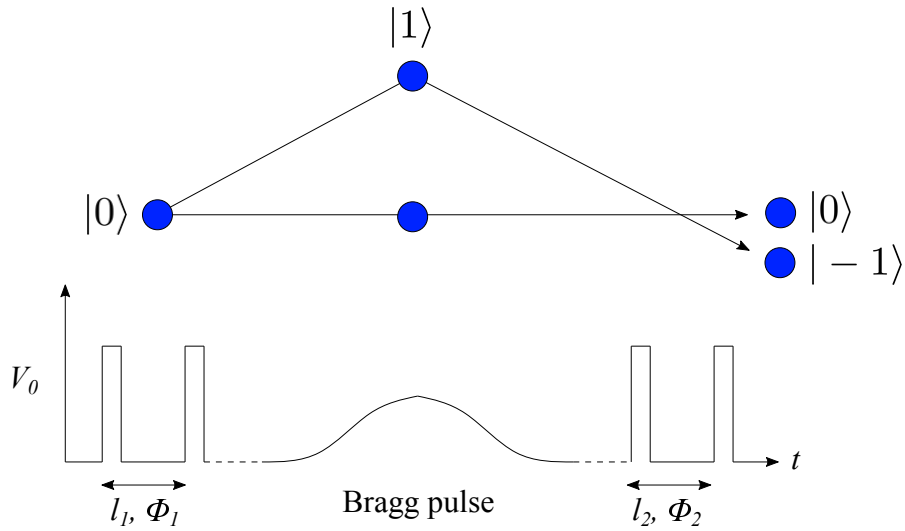


Figure 9.2: AOKR based interferometer: The blue spheres denote the atomic ensemble. The first pulse pair splits this ensemble into a equal superposition of $|0\rangle$ and $|1\rangle$ states, where $|n\rangle$ denotes the n^{th} diffraction order. l and Φ denote the pulse pair separation and the relative lattice phase between the pair respectively. The Bragg π -pulse transfers atoms into the $|-1\rangle$ state. The interferometer is then closed by the final pulse pair.

offset (Φ_1) between the two pulses. This splitting has experimentally been demonstrated in Fig. 6.2. An AI sequence can be constructed from the pulse pair as shown in Fig. 9.2. The Bragg pulse with zero frequency difference between the counter-propagating beams couples the $|1\rangle$ and $|-1\rangle$ states, while keeping the $|0\rangle$ state unchanged. The parameters for the final pulse pair for closing the interferometer and optimizing the entire sequence requires further theoretical modeling and simulations. Using such short duration pulses which are at least an order of magnitude lesser in duration in comparison to Bragg pulses will reduce systematic effects due to AC Stark shift [166] and diffraction phase [185].

Appendix A

Appendix

A.1 Characterization of lattice phase noise induced due to vibrations

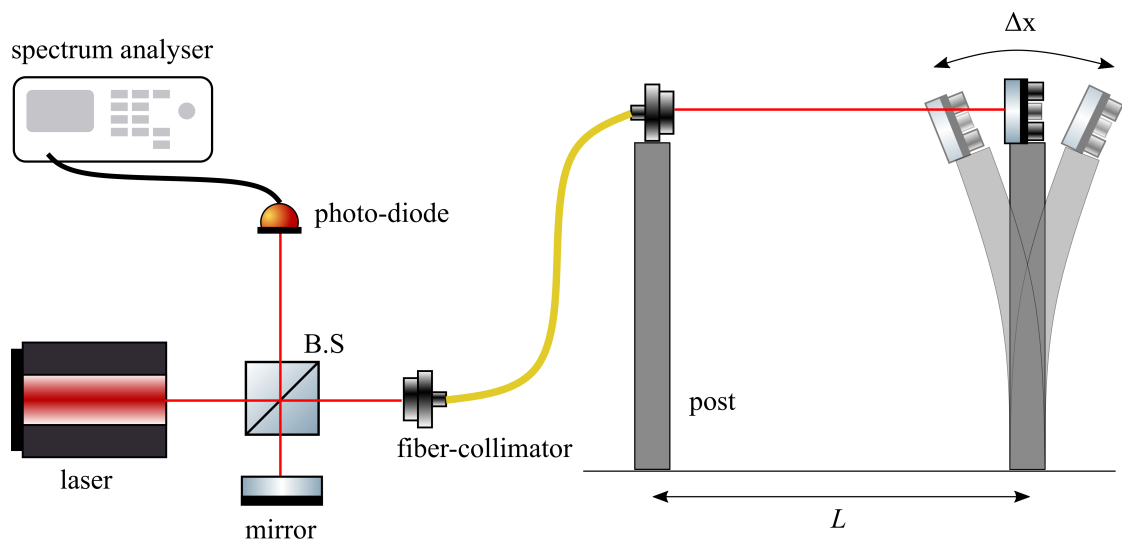


Figure A.1: Interferometric diagnosis of vibration noise: Schematic of the test setup used to characterize the vibration noise introduced in the optical lattice. Light from the laser was split into two paths using a non-polarizing beam splitter. The longer path traversed the optical fiber length and a distance $2L = 18$ cm, which is the separation between the two steel posts. This path was then interfered with the shorter one on the photo-diode. Any vibrations in the steel posts Δx (highly exaggerated in the figure) produced an intensity variation in the interferometer signal. The photo-diode signal was fed to a spectrum analyzer (SRS's SR785).

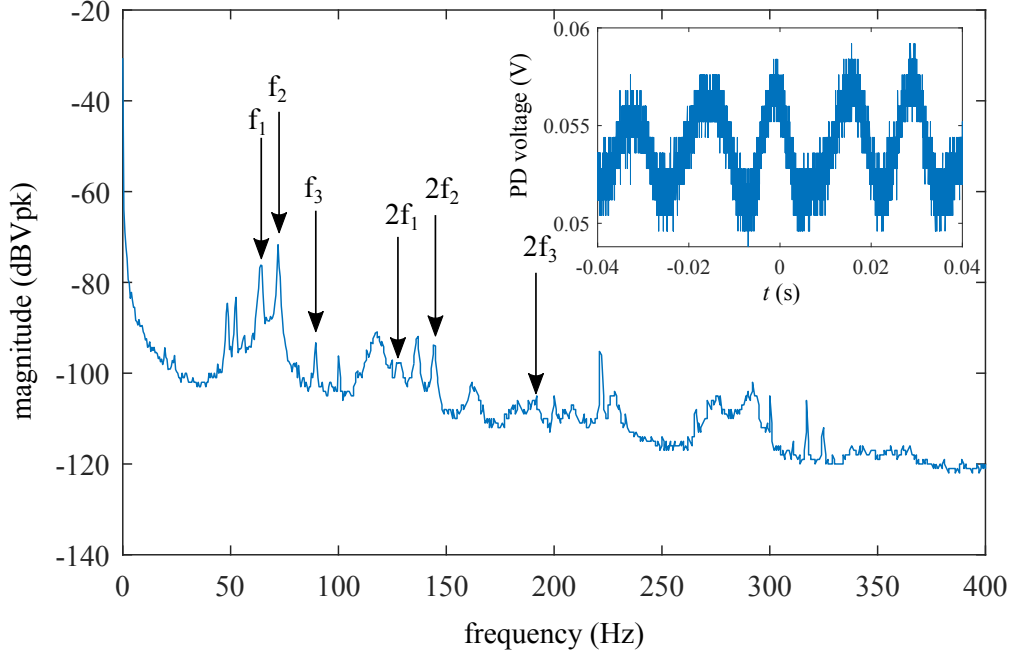


Figure A.2: FFT of photo-diode data: The marked peaks in frequency are as follows: $f_1 = 64.5$ Hz, $f_2 = 72$ Hz and $f_3 = 89.5$ Hz. Thus, the timescale for the vibrations is at the level of ~ 10 ms for this configuration of optics. Inset shows the time series data captured on an oscilloscope over a time scale of 80 ms.

Vibration noise is one of the major noise sources that affect the performance of an atom interferometer [186]. In the AOKR experiments, the vibration noise enters as fluctuations of lattice phase. These fluctuations can significantly affect the quantum dynamics [167]. We observed that the readout of the AOKR sequence (chapter 5) showed considerable fluctuations as the total number of pulses were increased beyond 5. Since the sequence did not break spatial symmetry, any asymmetric distribution which changes shot-to-shot is caused due to phase noise. To determine the characteristic time scale at which the vibration induced phase noise is dominant, a dummy setup was arranged as shown in Fig. A.1. The two 2-inch steel posts were separated by approximately 900 mm. The collimator and the retro mirror were mounted on a height of 280 mm on the 2-inch posts to mimic the kicking beams on the ^{87}Rb setup. The two mirrors shown in Fig. A.1 form a Michelson interferometer whose fringe readout is done at the photo-diode. An iris is arranged in the common path such that only a single fringe falls on the photo-diode. The intensity fluctuations due to vibrations of the posts are then

monitored on a spectrum analyzer (SRS's SR785). As it can be seen from the spectrum analyzer data in Fig. A.2, the time scale for these vibrations are of the order of ~ 10 ms.

A.2 BEC momentum width measurement using Bragg spectroscopy

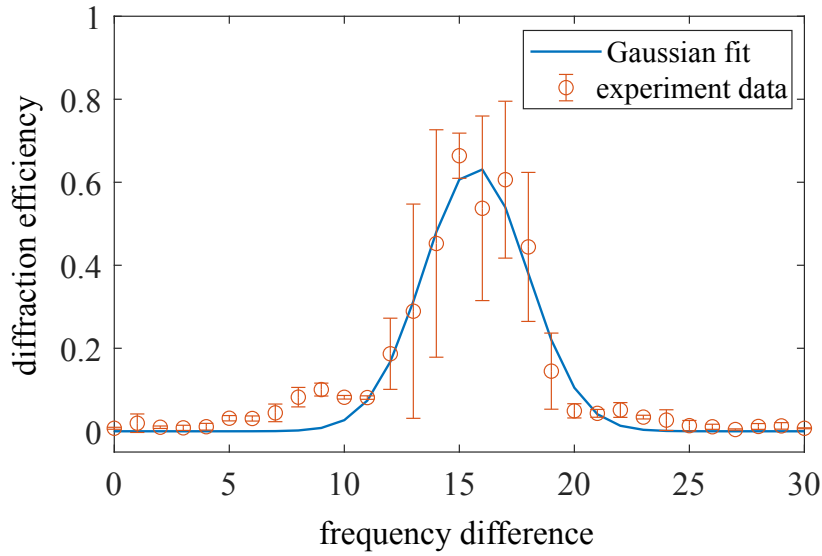


Figure A.3: Bragg spectroscopy of BEC: The BEC was subjected to a Bragg pulse of $200 \mu\text{s}$ duration, $100 \mu\text{s}$ after release from the trap. The frequency difference between the Bragg beams was scanned from 0-30 kHz. The standard deviation of the Gaussian fit to diffraction efficiency peak is 2.26 kHz.

The Bragg diffraction process is dependent on the initial momentum of the atoms as shown in Eq. 3.13. Thus for a width of $\Delta\nu$ in the Bragg frequency spectrum, the equivalent momentum spread of the BEC $\Delta\beta$ is given by:

$$\Delta\beta = \frac{2\pi m\Delta\nu}{K} \quad (\text{A.1})$$

Here, $K = 4\pi/\lambda$ is the grating constant. For $\Delta\nu = 2.26$ kHz the measurement of which is shown in Fig. A.3, $\Delta\beta = 0.075 \hbar K$. Though this seems broader than the value of $\Delta\beta \sim 0.02 - 0.03 \hbar K$, estimated from the AOKR experiment and the measurement of trapping frequency it may be likely due not using Fourier limited pulse width. A

pulse width of greater than $250 \mu\text{s}$ is required to resolve the spectrum beyond 1 kHz. Ref. [128] used a pulse width of $500 \mu\text{s}$ to resolve a spectrum whose width was 2 kHz (rms width). Our attempts to increase the pulse duration beyond $200 \mu\text{s}$ resulted in increased fluctuation in diffraction efficiency. This is already seen in the relatively large error bars in Fig. A.3. Simulation results indicate that this fluctuation is likely due to a phase noise in the lattice. Thus, the lattice has to be stabilized further to perform a more accurate momentum spectroscopy experiment.

A.3 Absorption imaging

Absorption imaging is a reliable way of obtaining high SNR images of cold atom clouds. It is a form of destructive imaging of atoms as the light used to observe the atomic cloud is on resonance with the relevant transition. When an absorption image is to be acquired, the cloud is illuminated with a pulse of on resonance laser beam with intensity I_0 . The transmitted light due to absorption by the atomic cloud is given by the Beer-Lambert's law:

$$I = I_0 e^{-n(x,y)\sigma} \quad (\text{A.2})$$

Where, $n(x, y)$ is the integrated column density in the direction of the beam and σ is the absorption cross-section. The exponent $n(x, y)\sigma$ is called the optical density or OD. If the illumination is on resonance and the intensity is near saturation, one can use the resonant absorption cross-section $\sigma_0 = \hbar\omega\Gamma/4I_s$ (ω = laser angular frequency, Γ = decay rate of transition, I_s = saturation intensity). To eliminate the effects of stray light and dark counts in the camera, a reference image (I_{ref}) is used where the camera image is acquired without the imaging illumination. Thus the measured optical density is:

$$OD_m = \ln \frac{I_l - I_{ref}}{I_a - I_{ref}} \quad (\text{A.3})$$

Where I_a and I_l are light intensities measured in and without the presence of atoms. This is the OD that is mentioned in all the images in this thesis. In our setup we use a single lens of 200 mm focal length to image the atomic cloud [93]. This lens is kept between equidistant from the camera and the atoms such that it is $2f$ away from both. The imaging beam diameter is 22 mm and typically has a power of 3-4 mW. To obtain

the amount of atoms in each diffracted order in the AOKR experiments, we use linear number density (n_l), integrated along the direction orthogonal to the lattice light.

$$n_l = \frac{1}{\sigma_0} \int_{-\infty}^{\infty} OD_m dx \quad (\text{A.4})$$

This linear number density is plotted in Fig. 3.2 to determine the population in each diffracted order.

Bibliography

- [1] Peter J. Mohr, David B. Newell, and Barry N. Taylor. Codata recommended values of the fundamental physical constants: 2014. *Rev. Mod. Phys.*, **88**:035009, Sep 2016.
- [2] S. Sturm, F. Köhler, J. Zatorski, A. Wagner, Z. Harman, G. Werth, W. Quint, C. H. Keitel, and K. Blaum. High-precision measurement of the atomic mass of the electron. *Nature*, **506**(7489):467–470, Feb 2014.
- [3] M. Planck. On the theory of the energy distribution law of the normal spectrum. *Verhandl. Dtsch. phys. Ges.*, **2**:237, 1900.
- [4] Louis De Broglie. Waves and quanta. *Nature*, **112**(2815):540–540, Oct 1923.
- [5] C. J. Davisson and L. H. Germer. Reflection of electrons by a crystal of nickel. *Proc. Natl. Acad. Sci. U S A*, **14**(4):317–322, Apr 1928. 16587341[pmid].
- [6] G. P. Thomson and A. Reid. Diffraction of cathode rays by a thin film. *Nature*, **119**(3007):890–890, Jun 1927.
- [7] C. G. Shull, W. A. Strauser, and E. O. Wollan. Neutron diffraction by paramagnetic and antiferromagnetic substances. *Phys. Rev.*, **83**:333–345, Jul 1951.
- [8] I. Estermann and O. Stern. Beugung von molekularstrahlen. *Zeitschrift für Physik*, **61**(1):95–125, Jan 1930.

- [9] Markus Arndt, Olaf Nairz, Julian Vos-Andreae, Claudia Keller, Gerbrand van der Zouw, and Anton Zeilinger. Wave–particle duality of c60 molecules. *Nature*, **401**(6754):680–682, Oct 1999.
- [10] DH Kruger, P Schneck, and HR Gelderblom. Helmut ruska and the visualisation of viruses. *The Lancet*, **355**(9216):1713–1717, 2000.
- [11] M. Bergin, S. M. Lambrick, H. Sleath, D. J. Ward, J. Ellis, and A. P. Jardine. Observation of diffraction contrast in scanning helium microscopy. *Sci. Rep.*, **10**(1):2053, Feb 2020.
- [12] Robin Woracek, Javier Santisteban, Anna Fedrigo, and Markus Strobl. Diffraction in neutron imaging a review. *Nucl. Instrum. Methods. Phys. Res. A*, **878**:141–158, 2018. Radiation Imaging Techniques and Applications.
- [13] P Geyer, U Sezer, J Rodewald, L Mairhofer, N Dörre, P Haslinger, S Eibenberger, C Brand, and M Arndt. Perspectives for quantum interference with biomolecules and biomolecular clusters. *Phys. Scr.*, **91**(6):063007, may 2016.
- [14] B. P. Abbott et al. Observation of gravitational waves from a binary black hole merger. *Phys. Rev. Lett.*, **116**:061102, Feb 2016.
- [15] H. Rauch, W. Treimer, and U. Bonse. Test of a single crystal neutron interferometer. *Phys. Lett. A*, **47**(5):369–371, Apr 1974.
- [16] R. Colella, A. W. Overhauser, and S. A. Werner. Observation of gravitationally induced quantum interference. *Phys. Rev. Lett.*, **34**:1472–1474, Jun 1975.
- [17] B. Heacock, M. Arif, R. Haun, M. G. Huber, D. A. Pushin, and A. R. Young. Neutron interferometer crystallographic imperfections and gravitationally induced quantum interference measurements. *Phys. Rev. A*, **95**:013840, Jan 2017.
- [18] R. Haun, F. E. Wietfeldt, M. Arif, M. G. Huber, T. C. Black, B. Heacock, D. A. Pushin, and C. B. Shahi. Precision measurement of the neutron scattering length of ^4He using neutron interferometry. *Phys. Rev. Lett.*, **124**:012501, Jan 2020.

- [19] Philippe Brax, Guillaume Pignol, and Damien Roulier. Probing strongly coupled chameleons with slow neutrons. *Phys. Rev. D*, **88**:083004, Oct 2013.
- [20] E. L. Raab, M. Prentiss, Alex Cable, Steven Chu, and D. E. Pritchard. Trapping of neutral sodium atoms with radiation pressure. *Phys. Rev. Lett.*, **59**:2631–2634, Dec 1987.
- [21] C. Monroe, W. Swann, H. Robinson, and C. Wieman. Very cold trapped atoms in a vapor cell. *Phys. Rev. Lett.*, **65**:1571–1574, Sep 1990.
- [22] Paul D. Lett, Richard N. Watts, Christoph I. Westbrook, William D. Phillips, Phillip L. Gould, and Harold J. Metcalf. Observation of atoms laser cooled below the doppler limit. *Phys. Rev. Lett.*, **61**:169–172, Jul 1988.
- [23] O. Carnal and J. Mlynek. Young’s double-slit experiment with atoms: A simple atom interferometer. *Phys. Rev. Lett.*, **66**:2689–2692, May 1991.
- [24] David W. Keith, Christopher R. Ekstrom, Quentin A. Turchette, and David E. Pritchard. An interferometer for atoms. *Phys. Rev. Lett.*, **66**:2693–2696, May 1991.
- [25] John F. Clauser and Shifang Li. Talbot-vonlau atom interferometry with cold slow potassium. *Phys. Rev. A*, **49**:R2213–R2216, Apr 1994.
- [26] Phillip L. Gould, George A. Ruff, and David E. Pritchard. Diffraction of atoms by light: The near-resonant kapitza-dirac effect. *Phys. Rev. Lett.*, **56**:827–830, Feb 1986.
- [27] Mark Kasevich and Steven Chu. Atomic interferometry using stimulated raman transitions. *Phys. Rev. Lett.*, **67**:181–184, Jul 1991.
- [28] K. Bongs, R. Launay, and M. A. Kasevich. High-order inertial phase shifts for time-domain atom interferometers. *Appl. Phys. B*, **84**(4):599–602, Sep 2006.
- [29] Achim Peters, Keng Yeow Chung, and Steven Chu. Measurement of gravitational acceleration by dropping atoms. *Nature*, **400**(6747):849–852, Aug 1999.

- [30] M. Hauth, C. Freier, V. Schkolnik, A. Senger, M. Schmidt, and A. Peters. First gravity measurements using the mobile atom interferometer gain. *Appl. Phys. B*, **113**(1):49–55, Oct 2013.
- [31] John F. Clauser. Ultra-high sensitivity accelerometers and gyroscopes using neutral atom matter-wave interferometry. *Physica B+C*, **151**(1):262–272, 1988.
- [32] D. Savoie, M. Altorio, B. Fang, L. A. Sidorenkov, R. Geiger, and A. Landragin. Interleaved atom interferometry for high-sensitivity inertial measurements. *Sci. Adv.*, **4**(12), 2018.
- [33] Zhong-Kun Hu, Bu-Liang Sun, Xiao-Chun Duan, Min-Kang Zhou, Le-Le Chen, Su Zhan, Qiao-Zhen Zhang, and Jun Luo. Demonstration of an ultrahigh-sensitivity atom-interferometry absolute gravimeter. *Phys. Rev. A*, **88**:043610, Oct 2013.
- [34] K. S. Hardman, P. J. Everitt, G. D. McDonald, P. Manju, P. B. Wigley, M. A. Sooriyabandara, C. C. N. Kuhn, J. E. Debs, J. D. Close, and N. P. Robins. Simultaneous precision gravimetry and magnetic gradiometry with a bose-einstein condensate: A high precision, quantum sensor. *Phys. Rev. Lett.*, **117**:138501, Sep 2016.
- [35] Xuejian Wu, Zachary Pagel, Bola S. Malek, Timothy H. Nguyen, Fei Zi, Daniel S. Scheirer, and Holger Müller. Gravity surveys using a mobile atom interferometer. *Sci. Adv.*, **5**(9), 2019.
- [36] Vincent Ménotet, Pierre Vermeulen, Nicolas Le Moigne, Sylvain Bonvalot, Philippe Bouyer, Arnaud Landragin, and Bruno Desruelle. Gravity measurements below 10^{-9} g with a transportable absolute quantum gravimeter. *Sci. Rep.*, **8**(1):12300, Aug 2018.
- [37] G. Stern, B. Battelier, R. Geiger, G. Varoquaux, A. Villing, F. Moron, O. Carraz, N. Zahzam, Y. Bidel, W. Chaibi, F. Pereira Dos Santos, A. Bresson, A. Landragin, and P. Bouyer. Light-pulse atom interferometry in microgravity. *Eur. Phys. J. D At. Mol. Opt. Phys.*, **53**(3):353–357, Jun 2009.

- [38] F. Sorrentino, Q. Bodart, L. Cacciapuoti, Y.-H. Lien, M. Prevedelli, G. Rosi, L. Salvi, and G. M. Tino. Sensitivity limits of a raman atom interferometer as a gravity gradiometer. *Phys. Rev. A*, **89**:023607, Feb 2014.
- [39] G. D’Amico, F. Borselli, L. Cacciapuoti, M. Prevedelli, G. Rosi, F. Sorrentino, and G. M. Tino. Bragg interferometer for gravity gradient measurements. *Phys. Rev. A*, **93**:063628, Jun 2016.
- [40] Zhong-Kun Hu, Xiao-Chun Duan, Min-Kang Zhou, Bu-Liang Sun, Jin-Bo Zhao, Mao-Mao Huang, and Jun Luo. Simultaneous differential measurement of a magnetic-field gradient by atom interferometry using double fountains. *Phys. Rev. A*, **84**:013620, Jul 2011.
- [41] R. Geiger, V. M enoret, G. Stern, N. Zahzam, P. Cheinet, B. Battelier, A. Villing, F. Moron, M. Lours, Y. Bidel, A. Bresson, A. Landragin, and P. Bouyer. Detecting inertial effects with airborne matter-wave interferometry. *Nat. Commun.*, **2**(1):474, Sep 2011.
- [42] Y. Bidel, N. Zahzam, C. Blanchard, A. Bonnin, M. Cadoret, A. Bresson, D. Rouxel, and M. F. Lequentrec-Lalancette. Absolute marine gravimetry with matter-wave interferometry. *Nat. Commun.*, **9**(1):627, Feb 2018.
- [43] Hubiao Wang, Lin Wu, Hua Chai, Lifeng Bao, and Yong Wang. Location accuracy of ins/gravity-integrated navigation system on the basis of ocean experiment and simulation. *Sensors*, **17**(12), 2017.
- [44] Kuan-Hung Chen, Cheinway Hwang, Liang-Cheng Chang, and Chien-Chung Ke. Short-time geodetic determination of aquifer storage coefficient in taiwan. *J. Geophys. Res. Solid Earth*, **123**(12):10,987–11,015, 2018.
- [45] Wolfgang Ketterle and Alan O. Jamison. An atomic physics perspective on the kilogram’s new definition. *Physics Today*, **73**(5):32–38, 2020.
- [46] Peter Asenbaum, Chris Overstreet, Minjeong Kim, Joseph Curti, and Mark A. Kasevich. Atom-interferometric test of the equivalence principle at the 10^{-12} level. *Phys. Rev. Lett.*, **125**:191101, Nov 2020.

- [47] P. Hamilton, M. Jaffe, P. Haslinger, Q. Simmons, H. Müller, and J. Khoury. Atom-interferometry constraints on dark energy. *Science*, **349**(6250):849–851, 2015.
- [48] Chenghui Yu, Weicheng Zhong, Brian Estey, Joyce Kwan, Richard H. Parker, and Holger Müller. Atom-interferometry measurement of the fine structure constant. *Ann. Phys.*, **531**(5):1800346, 2019.
- [49] G. Rosi, F. Sorrentino, L. Cacciapuoti, M. Prevedelli, and G. M. Tino. Precision measurement of the newtonian gravitational constant using cold atoms. *Nature*, **510**(7506):518–521, Jun 2014.
- [50] T. Kovachy, P. Asenbaum, C. Overstreet, C. A. Donnelly, S. M. Dickerson, A. Sugarbaker, J. M. Hogan, and M. A. Kasevich. Quantum superposition at the half-metre scale. *Nature*, **528**(7583):530–533, Dec 2015.
- [51] B. Canuel, A. Bertoldi, L. Amand, E. Pozzo di Borgo, T. Chantrait, C. Danquigny, M. Dovalé Álvarez, B. Fang, A. Freise, R. Geiger, J. Gillot, S. Henry, J. Hinderer, D. Holleville, J. Junca, G. Lefèvre, M. Merzougui, N. Mielec, T. Monfret, S. Pelisson, M. Prevedelli, S. Reynaud, I. Riou, Y. Rogister, S. Rosat, E. Cormier, A. Landragin, W. Chaibi, S. Gaffet, and P. Bouyer. Exploring gravity with the miga large scale atom interferometer. *Sci. Rep.*, **8**(1):14064, Sep 2018.
- [52] Richard H. Parker, Chenghui Yu, Brian Estey, Weicheng Zhong, Eric Huang, and Holger Müller. Controlling the multiport nature of bragg diffraction in atom interferometry. *Phys. Rev. A*, **94**:053618, Nov 2016.
- [53] Richard H. Parker, Chenghui Yu, Weicheng Zhong, Brian Estey, and Holger Müller. Measurement of the fine-structure constant as a test of the standard model. *Science*, **360**(6385):191–195, 2018.
- [54] M. Weitz, T. Heupel, and T. W. Hänsch. Multiple beam atomic interferometer. *Phys. Rev. Lett.*, **77**:2356–2359, Sep 1996.

- [55] Alan O. Jamison, Benjamin Plotkin-Swing, and Subhadeep Gupta. Advances in precision contrast interferometry with yb bose-einstein condensates. *Phys. Rev. A*, **90**:063606, Dec 2014.
- [56] Henry Fox Talbot. Lxxvi. facts relating to optical science. no. iv. *Philos. Mag.*, **9**(56):401–407, 1836.
- [57] Lord Rayleigh F.R.S. Xxv. on copying diffraction-gratings, and on some phenomena connected therewith. *The London, Edinburgh, and Dublin Philosophical Magazine and Journal of Science*, **11**(67):196–205, 1881.
- [58] Jianming Wen, Yong Zhang, and Min Xiao. The talbot effect: recent advances in classical optics, nonlinear optics, and quantum optics. *Adv. Opt. Photon.*, **5**(1):83–130, Mar 2013.
- [59] H. Hamam. Talbot array illuminators: general approach. *Appl. Opt.*, **36**(11):2319–2327, Apr 1997.
- [60] S. Sanders, R. Waarts, D. Nam, D. Welch, J. C. Ehlert, W. J. Cassarly, J. M. Finlan, and K. M. Flood. Phase locking of a two-dimensional semiconductor laser array in an external talbot cavity. In *Proceedings of LEOS '93*, pages 590–591, 1993.
- [61] Christian Kottler, Vincent Revol, Rolf Kaufmann, and Claus Urban. Dual energy phase contrast x-ray imaging with talbot-lau interferometer. *J. Appl. Phys.*, **108**(11):114906, 2010.
- [62] Zhaoyang Zhang, Xing Liu, Dan Zhang, Jiteng Sheng, Yiqi Zhang, Yanpeng Zhang, and Min Xiao. Observation of electromagnetically induced talbot effect in an atomic system. *Phys. Rev. A*, **97**:013603, Jan 2018.
- [63] Weiwei Zhang, Chenlong Zhao, Jiayuan Wang, and Jiasen Zhang. An experimental study of the plasmonic talbot effect. *Opt. Express*, **17**(22):19757–19762, Oct 2009.

- [64] Stefan Gerlich, Lucia Hackermüller, Klaus Hornberger, Alexander Stibor, Hendrik Ulbricht, Michael Gring, Fabienne Goldfarb, Tim Savas, Marcel Müri, Marcel Mayor, and Markus Arndt. A kapitza–dirac–talbot–lau interferometer for highly polarizable molecules. *Nat. Phys.*, **3**(10):711–715, Oct 2007.
- [65] Michael S. Chapman, Christopher R. Ekstrom, Troy D. Hammond, Jörg Schmiedmayer, Bridget E. Tannian, Stefan Wehinger, and David E. Pritchard. Near-field imaging of atom diffraction gratings: The atomic talbot effect. *Phys. Rev. A*, **51**:R14–R17, Jan 1995.
- [66] L. Deng, E. W. Hagley, J. Denschlag, J. E. Simsarian, Mark Edwards, Charles W. Clark, K. Helmerson, S. L. Rolston, and W. D. Phillips. Temporal, matter-wave-dispersion talbot effect. *Phys. Rev. Lett.*, **83**:5407–5411, Dec 1999.
- [67] Mark G. Raizen. Quantum chaos with cold atoms. *Adv. At. Mol. Opt. Phys.*, **41**:43–81, 1999.
- [68] W. K. Hensinger, H. Häffner, A. Browaeys, N. R. Heckenberg, K. Helmerson, C. McKenzie, G. J. Milburn, W. D. Phillips, S. L. Rolston, H. Rubinsztein-Dunlop, and B. Upcroft. Dynamical tunnelling of ultracold atoms. *Nature*, **412**(6842):52–55, Jul 2001.
- [69] G. Behinaein, V. Ramareddy, P. Ahmadi, and G. S. Summy. Exploring the phase space of the quantum δ -kicked accelerator. *Phys. Rev. Lett.*, **97**:244101, Dec 2006.
- [70] Mark Sadgrove, Munekazu Horikoshi, Tetsuo Sekimura, and Ken’ichi Nakagawa. Rectified momentum transport for a kicked bose-einstein condensate. *Phys. Rev. Lett.*, **99**:043002, Jul 2007.
- [71] Siamak Dadras, Alexander Gresch, Caspar Groiseau, Sandro Wimberger, and Gil S. Summy. Quantum walk in momentum space with a bose-einstein condensate. *Phys. Rev. Lett.*, **121**:070402, Aug 2018.

- [72] Pascal Szriftgiser, Jean Ringot, Dominique Delande, and Jean Claude Garreau. Observation of sub-fourier resonances in a quantum-chaotic system. *Phys. Rev. Lett.*, **89**:224101, Nov 2002.
- [73] C. Ryu, M. F. Andersen, A. Vaziri, M. B. d’Arcy, J. M. Grossman, K. Helmerson, and W. D. Phillips. High-order quantum resonances observed in a periodically kicked bose-einstein condensate. *Phys. Rev. Lett.*, **96**:160403, Apr 2006.
- [74] Shijie Chai. *Measuring The Gravitational Field with an Atomic Ruler*. PhD thesis, Dunedin, New Zealand, 2019.
- [75] Brynle Barrett, Adam Carew, Hermina C. Beica, Andrejs Vorozcovs, Alexander Pouliot, and A. Kumarakrishnan. Prospects for precise measurements with echo atom interferometry. *Atoms*, **4**(3), 2016.
- [76] Shijie Chai, Julia Fekete, and Mikkel F. Andersen. Measuring the local gravitational field using survival resonances in a dissipatively driven atom-optics system. *Phys. Rev. A*, **98**:063614, Dec 2018.
- [77] Shijie Chai and Mikkel F. Andersen. Enhancing survival resonances with engineered dissipation. *Phys. Rev. Research*, **2**:033194, Aug 2020.
- [78] A. Shayeghi, P. Rieser, G. Richter, U. Sezer, J. H. Rodewald, P. Geyer, T. J. Martinez, and M. Arndt. Matter-wave interference of a native polypeptide. *Nat. Commun.*, **11**(1):1447, Mar 2020.
- [79] Yaakov Y. Fein, Philipp Geyer, Patrick Zwick, Filip Kiałka, Sebastian Pedalino, Marcel Mayor, Stefan Gerlich, and Markus Arndt. Quantum superposition of molecules beyond 25 kda. *Nat. Phys.*, **15**(12):1242–1245, Dec 2019.
- [80] Stefan Gerlich, Yaakov Y. Fein, and Markus Arndt. *Interferometric Tests of Wave-Function Collapse*. Springer International Publishing, Cham, 2021.
- [81] Yaakov Y. Fein, Stefan Gerlich, Armin Shayeghi, Philipp Geyer, Filip Kiałka, Valentin Köhler, Marcel Mayor, and Markus Arndt. Universal matter-wave interferometry as a sensor in atomic physics and physical chemistry. In Selim M.

- Shahriar and Jacob Scheuer, editors, *Optical and Quantum Sensing and Precision Metrology*, volume 11700, pages 17 – 27. International Society for Optics and Photonics, SPIE, 2021.
- [82] Boris Daszuta and Mikkel F. Andersen. Atom interferometry using δ -kicked and finite-duration pulse sequences. *Phys. Rev. A*, **86**:043604, Oct 2012.
- [83] R. A. Horne, R. H. Leonard, and C. A. Sackett. Utility of atomic kicked-rotor interferometers for precision measurements. *Phys. Rev. A*, **83**:063613, Jun 2011.
- [84] I. Talukdar, R. Shrestha, and G. S. Summy. Sub-fourier characteristics of a δ -kicked-rotor resonance. *Phys. Rev. Lett.*, **105**:054103, Jul 2010.
- [85] Michele Delvecchio, Caspar Groiseau, Francesco Petiziol, Gil S Summy, and Sandro Wimberger. Quantum search with a continuous-time quantum walk in momentum space. *J. Phys. B: At. Mol. Opt. Phys.*, **53**(6):065301, feb 2020.
- [86] Michele Delvecchio, Francesco Petiziol, and Sandro Wimberger. Resonant quantum kicked rotor as a continuous-time quantum walk. *Condens. Matter*, **5**(1), 2020.
- [87] Kerson Huang. *Statistical mechanics / Kerson Huang*. Wiley New York, 2nd ed. edition, 1987.
- [88] Harold J. Metcalf and Peter van der Straten. *Laser Cooling and Trapping*. Springer-Verlag, New York, 1999.
- [89] L Allen and J H Eberly. Optical resonance and two-level atoms.
- [90] P. Cheiney, O. Carraz, D. Bartoszek-Bober, S. Faure, F. Vermersch, C. M. Fabre, G. L. Gattobigio, T. Lahaye, D. Guéry-Odelin, and R. Mathevet. A zeeman slower design with permanent magnets in a halbach configuration. *Rev. Sci. Instrum.*, **82**(6):063115, 2011.
- [91] Christopher J Foot. *Atomic physics*. Oxford master series in atomic, optical, and laser physics. Oxford University Press, Oxford, 2007.

- [92] Sunil Kumar. *Towards distributed quantum information processing using coupling of neutral atoms to plasmonic nanostructures*. PhD thesis, Indian Institute of Science Education and Research, Pune, India, 2017.
- [93] Sumit Sarkar. *Ultracold atoms in 1-D optical lattices: experiments towards quantum chaos and atom interferometry*. PhD thesis, Indian Institute of Science Education and Research, Pune, India, 4 2019.
- [94] S. J. M. Kuppens, K. L. Corwin, K. W. Miller, T. E. Chupp, and C. E. Wieman. Loading an optical dipole trap. *Phys. Rev. A*, **62**:013406, Jun 2000.
- [95] Wolfgang Petrich, Michael H. Anderson, Jason R. Ensher, and Eric A. Cornell. Behavior of atoms in a compressed magneto-optical trap. *J. Opt. Soc. Am. B*, **11**(8):1332–1335, Aug 1994.
- [96] Rudolf Grimm, Matthias Weidemüller, and Yurii B. Ovchinnikov. Optical dipole traps for neutral atoms. *Adv. At. Mol. Opt. Phys.*, **42**:95–170, 2000.
- [97] A. Fuhrmanek, R. Bourgain, Y. R. P. Sortais, and A. Browaeys. Light-assisted collisions between a few cold atoms in a microscopic dipole trap. *Phys. Rev. A*, **85**:062708, Jun 2012.
- [98] Jun John Sakurai. *Modern quantum mechanics; rev. ed.* Addison-Wesley, Reading, MA, 1994.
- [99] A. Einstein. *Quantentheorie des einatomigen idealen Gases*, pages 237–244. John Wiley and Sons, Ltd, 2005.
- [100] Bose. Plancks gesetz und lichtquantenhypothese. *Zeitschrift für Physik*, **26**(1):178–181, Dec 1924.
- [101] C E Hecht. The possible superfluid behaviour of hydrogen atom gases and liquids. *Physica*.
- [102] Willian C. Stwalley and L. H. Nosanow. Possible "new" quantum systems. *Phys. Rev. Lett.*, **36**:910–913, Apr 1976.

- [103] Dale G. Fried, Thomas C. Killian, Lorenz Willmann, David Landhuis, Stephen C. Moss, Daniel Kleppner, and Thomas J. Greytak. Bose-einstein condensation of atomic hydrogen. *Phys. Rev. Lett.*, **81**:3811–3814, Nov 1998.
- [104] M. H. Anderson, J. R. Ensher, M. R. Matthews, C. E. Wieman, and E. A. Cornell. Observation of bose-einstein condensation in a dilute atomic vapor. *Science*, **269**(5221):198–201, 1995.
- [105] K. B. Davis, M. O. Mewes, M. R. Andrews, N. J. van Druten, D. S. Durfee, D. M. Kurn, and W. Ketterle. Bose-einstein condensation in a gas of sodium atoms. *Phys. Rev. Lett.*, **75**:3969–3973, Nov 1995.
- [106] F. Pereira Dos Santos, J. Léonard, Junmin Wang, C. J. Barrelet, F. Perales, E. Rasel, C. S. Unnikrishnan, M. Leduc, and C. Cohen-Tannoudji. Bose-einstein condensation of metastable helium. *Phys. Rev. Lett.*, **86**:3459–3462, Apr 2001.
- [107] C. C. Bradley, C. A. Sackett, J. J. Tollett, and R. G. Hulet. Evidence of bose-einstein condensation in an atomic gas with attractive interactions. *Phys. Rev. Lett.*, **75**:1687–1690, Aug 1995.
- [108] G. Modugno, G. Ferrari, G. Roati, R. J. Brecha, A. Simoni, and M. Inguscio. Bose-einstein condensation of potassium atoms by sympathetic cooling. *Science*, **294**(5545):1320–1322, 2001.
- [109] Sebastian Kraft, Felix Vogt, Oliver Appel, Fritz Riehle, and Uwe Sterr. Bose-einstein condensation of alkaline earth atoms: ^{40}Ca . *Phys. Rev. Lett.*, **103**:130401, Sep 2009.
- [110] Axel Griesmaier, Jörg Werner, Sven Hensler, Jürgen Stuhler, and Tilman Pfau. Bose-einstein condensation of chromium. *Phys. Rev. Lett.*, **94**:160401, Apr 2005.
- [111] Simon Stellmer, Meng Khoon Tey, Bo Huang, Rudolf Grimm, and Florian Schreck. Bose-einstein condensation of strontium. *Phys. Rev. Lett.*, **103**:200401, Nov 2009.

- [112] Tino Weber, Jens Herbig, Michael Mark, Hanns-Christoph Nägerl, and Rudolf Grimm. Bose-einstein condensation of cesium. *Science*, **299**(5604):232–235, 2003.
- [113] Mingwu Lu, Nathaniel Q. Burdick, Seo Ho Youn, and Benjamin L. Lev. Strongly dipolar bose-einstein condensate of dysprosium. *Phys. Rev. Lett.*, **107**:190401, Oct 2011.
- [114] K. Aikawa, A. Frisch, M. Mark, S. Baier, A. Rietzler, R. Grimm, and F. Ferlaino. Bose-einstein condensation of erbium. *Phys. Rev. Lett.*, **108**:210401, May 2012.
- [115] E. T. Davletov, V. V. Tsyganok, V. A. Khlebnikov, D. A. Pershin, D. V. Shaykin, and A. V. Akimov. Machine learning for achieving bose-einstein condensation of thulium atoms. *Phys. Rev. A*, **102**:011302, Jul 2020.
- [116] Yosuke Takasu, Kenichi Maki, Kaduki Komori, Tetsushi Takano, Kazuhito Honda, Mitsutaka Kumakura, Tsutomu Yabuzaki, and Yoshiro Takahashi. Spin-singlet bose-einstein condensation of two-electron atoms. *Phys. Rev. Lett.*, **91**:040404, Jul 2003.
- [117] S. Jochim, M. Bartenstein, A. Altmeyer, G. Hendl, S. Riedl, C. Chin, J. Hecker Denschlag, and R. Grimm. Bose-einstein condensation of molecules. *Science*, **302**(5653):2101–2103, 2003.
- [118] M. R. Andrews, C. G. Townsend, H.-J. Miesner, D. S. Durfee, D. M. Kurn, and W. Ketterle. Observation of interference between two bose condensates. *Science*, **275**(5300):637–641, 1997.
- [119] D. S. Jin, J. R. Ensher, M. R. Matthews, C. E. Wieman, and E. A. Cornell. Collective excitations of a bose-einstein condensate in a dilute gas. *Phys. Rev. Lett.*, **77**:420–423, Jul 1996.
- [120] J. R. Abo-Shaeer, C. Raman, J. M. Vogels, and W. Ketterle. Observation of vortex lattices in bose-einstein condensates. *Science*, **292**(5516):476–479, 2001.

- [121] S. Burger, K. Bongs, S. Dettmer, W. Ertmer, K. Sengstock, A. Sanpera, G. V. Shlyapnikov, and M. Lewenstein. Dark solitons in bose-einstein condensates. *Phys. Rev. Lett.*, **83**:5198–5201, Dec 1999.
- [122] S. Inouye, A. P. Chikkatur, D. M. Stamper-Kurn, J. Stenger, D. E. Pritchard, and W. Ketterle. Superradiant rayleigh scattering from a bose-einstein condensate. *Science*, **285**(5427):571–574, 1999.
- [123] C. R. Cabrera, L. Tanzi, J. Sanz, B. Naylor, P. Thomas, P. Cheiney, and L. Tarruell. Quantum liquid droplets in a mixture of bose-einstein condensates. *Science*, **359**(6373):301–304, 2018.
- [124] D. M. Stamper-Kurn, M. R. Andrews, A. P. Chikkatur, S. Inouye, H.-J. Miesner, J. Stenger, and W. Ketterle. Optical confinement of a bose-einstein condensate. *Phys. Rev. Lett.*, **80**:2027–2030, Mar 1998.
- [125] Lev Pitaevskii and Sandro Stringari. *Bose-Einstein Condensation and Superfluidity*. Oxford university press, Great Clarendon Street, Oxford, OX2 6DP, United Kingdom, 2016.
- [126] C. J. Pethick and H. Smith. *Theory of the condensed state*, pages 159–181. Cambridge University Press, 2 edition, 2008.
- [127] S S Szigeti, J E Debs, J J Hope, N P Robins, and J D Close. Why momentum width matters for atom interferometry with bragg pulses. *New J. Phys.*, **14**(2):023009, feb 2012.
- [128] J. Stenger, S. Inouye, A. P. Chikkatur, D. M. Stamper-Kurn, D. E. Pritchard, and W. Ketterle. Bragg spectroscopy of a bose-einstein condensate. *Phys. Rev. Lett.*, **82**:4569–4573, Jun 1999.
- [129] Y. Castin and R. Dum. Bose-einstein condensates in time dependent traps. *Phys. Rev. Lett.*, **77**:5315–5319, Dec 1996.

- [130] Rui-Zong Li, Tian-You Gao, Dong-Fang Zhang, Shi-Guo Peng, Ling-Ran Kong, Xing Shen, and Kai-Jun Jiang. Expansion dynamics of a spherical bose–einstein condensate. *Chin. Phys. B*, **28**(10):106701, oct 2019.
- [131] Max Born, Emil Wolf, A. B. Bhatia, P. C. Clemmow, D. Gabor, A. R. Stokes, A. M. Taylor, P. A. Wayman, and W. L. Wilcock. *Principles of Optics: Electromagnetic Theory of Propagation, Interference and Diffraction of Light*. Cambridge University Press, 7 edition, 1999.
- [132] P. L. Kapitza and P. A. M. Dirac. The reflection of electrons from standing light waves. *Mathematical Proceedings of the Cambridge Philosophical Society*, **29**(2):297–300, 1933.
- [133] Daniel L. Freimund, Kayvan Aflatooni, and Herman Batelaan. Observation of the kapitza–dirac effect. *Nature*, **413**(6852):142–143, Sep 2001.
- [134] E Brion, L H Pedersen, and K Mølmer. Adiabatic elimination in a lambda system. *J. Phys. A Math. Theor.*, **40**(5):1033–1043, jan 2007.
- [135] Pierre Meystre and Murray SargentIII. *Elements of Quantum Optics*. Springer, Berlin, Heidelberg, 4 edition, 2007.
- [136] C V Raman and N S Nagendra Nath. The diffraction of light by high frequency sound waves: Part one. *Proc. Indian Acad. Sci.*, **A2**:406–412, 1936.
- [137] J. H. Huckans, I. B. Spielman, B. Laburthe Tolra, W. D. Phillips, and J. V. Porto. Quantum and classical dynamics of a bose-einstein condensate in a large-period optical lattice. *Phys. Rev. A*, **80**:043609, Oct 2009.
- [138] J. Baruchel, J.P. Guigay, C. Mazuré-Espejo, M. Schlenker, and J. Schweizer. Observation of pendellösung effect in polarized neutron scattering from a magnetic crystal. *Physica B+C*, **120**(1):80, 1983.
- [139] Mark Saunders. *Manifestation of quantum resonant effects in the atom-optical delta-kicked accelerator*. PhD thesis, Durham University, Durham, United Kingdom, 9 2011.

- [140] B.V.Chirikov. Research concerning the theory of nonlinear resonance and stochasticity. *Preprint N 267, Institute of Nuclear Physics, Novosibirsk*, 1969.
- [141] Wojciech Hubert Zurek and Juan Pablo Paz. Decoherence, chaos, and the second law. *Phys. Rev. Lett.*, **72**:2508–2511, Apr 1994.
- [142] G. Casati, I. Guarneri, and D.L. Shepelyansky. Classical chaos, quantum localization and fluctuations: A unified view. *Physica A: Statistical Mechanics and its Applications*, **163**(1):205–214, 1990.
- [143] B. G. Klappauf, D. A. Steck, and M. G. Raizen. Quantum chaos in mixed phase space: Beyond the delta kicked rotor. In *Quantum Electronics and Laser Science Conference*, page QWD12. Optical Society of America, 1997.
- [144] H. J. Korsch, E. M. Graefe, and Hans-Jörg Jodl. The kicked rotor: Computer-based studies of chaotic dynamics. *Am. J. Phys.*, **76**(4):498–503, 2008.
- [145] M. Arndt, A. Buchleitner, R. N. Mantegna, and H. Walther. Experimental study of quantum and classical limits in microwave ionization of rubidium rydberg atoms. *Phys. Rev. Lett.*, **67**:2435–2438, Oct 1991.
- [146] M. Bitter and V. Milner. Experimental observation of dynamical localization in laser-kicked molecular rotors. *Phys. Rev. Lett.*, **117**:144104, Sep 2016.
- [147] B. G. Klappauf, W. H. Oskay, D. A. Steck, and M. G. Raizen. Observation of noise and dissipation effects on dynamical localization. *Phys. Rev. Lett.*, **81**:1203–1206, Aug 1998.
- [148] F. L. Moore, J. C. Robinson, C. F. Bharucha, Bala Sundaram, and M. G. Raizen. Atom optics realization of the quantum δ -kicked rotor. *Phys. Rev. Lett.*, **75**:4598–4601, Dec 1995.
- [149] D. R. Grempel, R. E. Prange, and Shmuel Fishman. Quantum dynamics of a nonintegrable system. *Phys. Rev. A*, **29**:1639–1647, Apr 1984.
- [150] Gabriel Lemarié, Julien Chabé, Pascal Szriftgiser, Jean Claude Garreau, Benoît Grémaud, and Dominique Delande. Observation of the anderson metal-insulator

- transition with atomic matter waves: Theory and experiment. *Phys. Rev. A*, **80**:043626, Oct 2009.
- [151] Annie A.M. Cuyt, Vigdis Petersen, Brigitte Verdonk, Haakon Waadeland, and William B. Jones. *Handbook of Continued Fractions for Special Functions*. Springer Publishing Company, Incorporated, 1 edition, 2008.
- [152] M. Saunders, P. L. Halkyard, K. J. Challis, and S. A. Gardiner. Manifestation of quantum resonances and antiresonances in a finite-temperature dilute atomic gas. *Phys. Rev. A*, **76**:043415, Oct 2007.
- [153] A. Ullah, S. K. Ruddell, J. A. Currivan, and M. D. Hoogerland. Quantum resonant effects in the delta-kicked rotor revisited. *Eur. Phys. J. D At. Mol. Opt. Phys.*, **66**(12):315, Dec 2012.
- [154] P McDowall, A Hilliard, M McGovern, T Grünzweig, and M F Andersen. A fidelity treatment of near-resonant states in the atom-optics kicked rotor. *New J. Phys.*, **11**(12):123021, dec 2009.
- [155] Bryce Gadway, Daniel Pertot, René Reimann, Martin G. Cohen, and Dominik Schneble. Analysis of kapitza-dirac diffraction patterns beyond the raman-nath regime. *Opt. Express*, **17**(21):19173–19180, Oct 2009.
- [156] Wei Xiong, Xiaoji Zhou, Xuguang Yue, Yueyang Zhai, and Xuzong Chen. A momentum filter for atomic gas. *New J. Phys.*, **15**(6):063025, jun 2013.
- [157] J. Fekete, S. Chai, S. A. Gardiner, and M. F. Andersen. Resonant transfer of large momenta from finite-duration pulse sequences. *Phys. Rev. A*, **95**:033601, Mar 2017.
- [158] T. Kraemer, J. Herbig, M. Mark, T. Weber, C. Chin, H.-C. Nägerl, and R. Grimm. Optimized production of a cesium bose–einstein condensate. *Appl. Phys. B*, **79**(8):1013–1019, Dec 2004.
- [159] Hubert Ammann and Nelson Christensen. Delta kick cooling: A new method for cooling atoms. *Phys. Rev. Lett.*, **78**:2088–2091, Mar 1997.

- [160] Tim Kovachy, Jason M. Hogan, Alex Sugarbaker, Susannah M. Dickerson, Christine A. Donnelly, Chris Overstreet, and Mark A. Kasevich. Matter wave lensing to picokelvin temperatures. *Phys. Rev. Lett.*, **114**:143004, Apr 2015.
- [161] Ramón Ramos, David Spierings, Shreyas Potnis, and Aephraim M. Steinberg. Atom-optics knife edge: Measuring narrow momentum distributions. *Phys. Rev. A*, **98**:023611, Aug 2018.
- [162] Tobias Salger, Sebastian Kling, Tim Hecking, Carsten Geckeler, Luis Morales-Molina, and Martin Weitz. Directed transport of atoms in a hamiltonian quantum ratchet. *Science*, **326**(5957):1241–1243, 2009.
- [163] R. K. Shrestha, J. Ni, W. K. Lam, S. Wimberger, and G. S. Summy. Controlling the momentum current of an off-resonant ratchet. *Phys. Rev. A*, **86**:043617, Oct 2012.
- [164] D. H. White, S. K. Ruddell, and M. D. Hoogerland. Experimental realization of a quantum ratchet through phase modulation. *Phys. Rev. A*, **88**:063603, Dec 2013.
- [165] Saijun Wu, Ying-Ju Wang, Quentin Diot, and Mara Prentiss. Splitting matter waves using an optimized standing-wave light-pulse sequence. *Phys. Rev. A*, **71**:043602, Apr 2005.
- [166] Atsuo Morinaga, Toshiharu Tako, and Nobuhiko Ito. Sensitive measurement of phase shifts due to the ac stark effect in a ca optical ramsey interferometer. *Phys. Rev. A*, **48**:1364–1368, Aug 1993.
- [167] Caspar Groiseau, Alexander Wagner, Gil S. Summy, and Sandro Wimberger. Impact of lattice vibrations on the dynamics of a spinor atom-optics kicked rotor. *Condens. Matter*, **4**(1), 2019.
- [168] Peter Hänggi and Fabio Marchesoni. Artificial brownian motors: Controlling transport on the nanoscale. *Rev. Mod. Phys.*, **81**:387–442, Mar 2009.
- [169] Frank Jülicher, Armand Ajdari, and Jacques Prost. Modeling molecular motors. *Rev. Mod. Phys.*, **69**:1269–1282, Oct 1997.

- [170] Holger Schanz, Marc-Felix Otto, Roland Ketzmerick, and Thomas Dittrich. Classical and quantum hamiltonian ratchets. *Phys. Rev. Lett.*, **87**:070601, Jul 2001.
- [171] J. B. Majer, J. Peguiron, M. Grifoni, M. Tussveld, and J. E. Mooij. Quantum ratchet effect for vortices. *Phys. Rev. Lett.*, **90**:056802, Feb 2003.
- [172] Gui-Lu Long and Tian-Cai Zhang. Quantum ratchet with photons. *Science Bulletin*, **60**(2):278–278, Jan 2015.
- [173] Christopher Grossert, Martin Leder, Sergey Denisov, Peter Hänggi, and Martin Weitz. Experimental control of transport resonances in a coherent quantum rocking ratchet. *Nat. Commun.*, **7**(1):10440, Feb 2016.
- [174] Clément Hainaut, Adam Raçon, Jean-François Clément, Jean Claude Garreau, Pascal Szriftgiser, Radu Chircireanu, and Dominique Delande. Ratchet effect in the quantum kicked rotor and its destruction by dynamical localization. *Phys. Rev. A*, **97**:061601, Jun 2018.
- [175] M. Schiavoni, L. Sanchez-Palencia, F. Renzoni, and G. Grynberg. Phase control of directed diffusion in a symmetric optical lattice. *Phys. Rev. Lett.*, **90**:094101, Mar 2003.
- [176] I. Dana, V. Ramareddy, I. Talukdar, and G. S. Summy. Experimental realization of quantum-resonance ratchets at arbitrary quasimomenta. *Phys. Rev. Lett.*, **100**:024103, Jan 2008.
- [177] Jiating Ni, Wa Kun Lam, Siamak Dadras, Mario F. Borunda, Sandro Wimberger, and Gil S. Summy. Initial-state dependence of a quantum resonance ratchet. *Phys. Rev. A*, **94**:043620, Oct 2016.
- [178] J. A. Fleck, J. R. Morris, and M. D. Feit. Time-dependent propagation of high energy laser beams through the atmosphere. *Appl. Phys.*, **10**(2):129–160, Jun 1976.
- [179] James W. Cooley and John W. Tukey. An algorithm for the machine calculation of complex fourier series. *Math. Comput.*, **19**(90):297–301, 1965.

- [180] Gilbert Strang. On the construction and comparison of difference schemes. *SIAM J. Numer. Anal.*, **5**(3):506–517, 1968.
- [181] Justin T. Schultz, Azure Hansen, and Nicholas P. Bigelow. A raman waveplate for spinor bose-einstein condensates. *Opt. Lett.*, **39**(14):4271–4273, Jul 2014.
- [182] J. Martin, B. Georgeot, and D. L. Shepelyansky. Time reversal of bose-einstein condensates. *Phys. Rev. Lett.*, **101**:074102, Aug 2008.
- [183] A. Marte, T. Volz, J. Schuster, S. Dürr, G. Rempe, E. G. M. van Kempen, and B. J. Verhaar. Feshbach resonances in rubidium 87: Precision measurement and analysis. *Phys. Rev. Lett.*, **89**:283202, Dec 2002.
- [184] O. Thomas, C. Lippe, T. Eichert, and H. Ott. Experimental realization of a rydberg optical feshbach resonance in a quantum many-body system. *Nat. Commun.*, **9**(1):2238, Jun 2018.
- [185] M. Büchner, R. Delhulle, A. Miffre, C. Robilliard, J. Vigué, and C. Champenois. Diffraction phases in atom interferometers. *Phys. Rev. A*, **68**:013607, Jul 2003.
- [186] A. Miffre, M. Jacquy, M. Büchner, G. Tréneç, and J. Vigué. Vibration-induced phase noise in mach–zehnder atom interferometers. *Appl. Phys. B*, **84**(4):617–625, Sep 2006.